Condition Monitoring of Wind Turbines Using micro-Doppler information

Zijian Guo

Centre for Signal and Image Processing (CeSIP),
Department of Electronic and Electrical Engineering,
University of Strathclyde,
204 George Street,
Glasgow G1 1XW

Thesis submitted to the
University of Strathclyde
Master of Philosophy

October 2017

Supervisor: Prof. John Soraghan

Acknowledgements:

First of all, I would like to thank my supervisor Professor John Soraghan who has been an excellent mentor to me throughout the whole period of my master studies. His kindness to answer all the questions and providing me with wise advice through meetings is greatly appreciated. The conversations we had provided me with an analytical way of thinking which becomes a key element in solving problems.

I would also like to thank the radar research group, especially Dr. Carmine Clement, A. R. Persico and Domenico Gaglione for all the time they spent for answering my questions and having useful conversations on how to approach problems concerning my research.

I am grateful for everyone involved in the Wind turbine blade project, as well as for organizing the useful research and training events. I had an excellent experience of meeting and working with so many researchers.

There aren't enough words to thank my parents, to whom I owe a lifetime of gratitude, for the continuous encouragement and support throughout my studies

Last but not least, I owe a big thanks to my wife Fuyu Li. Her support has been invaluable and her patience to wait for me and encourage me all through this time is greatly valued and appreciated.

I am grateful for all the experts and professors who have participate in reviewing this paper, giving me valuable advice of this paper, thank you.

ABSTRACT

With the development of modern science technology and awareness of environmental protection, new energy technologies have emerged and developed rapidly. Wind power, as a renewable energy source, has played a pivotal role in society which has been deeply researched and promoted around the world in recent years. As wind turbine capacity is growing, wind turbine blade maintenance test and diagnosis have gradually drown people's attention, also have become the hot points in new energy technologies. Therefore, exploring the development of wind turbine blade detection and diagnosis is necessary.

This thesis will adopt radar technology to monitor and diagnose the operation of the wind turbine blade, with a simple and effective way to solve the working condition of wind turbine blades. This study focuses on the design of a running model of wind turbine, within-depth analysis of micro-Doppler of radar back scattering signals from wind turbine blades to determine the health of the wind turbine blades, providing the basic data for the maintenance of the wind turbine blades. Monitor and diagnosis of the whole process is divided into four parts—Theory Analysis, Mathematical Modeling, Algorithm Development and Experiment Design. The thesis will focus on the wind turbine blade daily operation problems --- vibration, corrosion, and other problems, through the data model analysis, to give a more efficient and accurate detection and diagnosis, to provide a remote and online protection for the safe operation of wind turbine blades.

Key words: Wind turbine; Wind turbine blades; Micro-Doppler effect; Radar; Monitor; Diagnosis.

CONTENTS

LIST OF FIGURES

LIST OF TABLES

Chapter 1 Introduction

1.1 Research Background and Motivation

Essentially, Wind energy is a transformation of solar energy. Airflow generates the kinetic energy on the earth's surface. Since the ground is irradiated by solar which has different temperature and the air has different water vapor, causing different pressure on the ground, in the horizontal direction, high-pressure air flows to low-pressure areas, therefore the wind is formed. The greater air flow rate is, the more kinetic energy is formed. People can use wind turbines to transfer kinetic energy into rotational movement to promote a generator producing electricity, through the shaft, transmitted the rotational power of rotors (composition of by the aero dynamic blades) to the generator. Modern turbine blades will transfer mechanical energy of airflow into electrical energy as a generator.

Wind turbine converts the kinetic energy of air flow to mechanical energy. Most of wind turbines are classified by wind receiving device structure and spatial arrangement; generally divided into two types--horizontal axis and vertical axis. For a conventional wind turbine with wind wheel as wind energy receiving device, according to the wind wheel shaft related to the direction of air flow, a wind turbine can be divided into horizontal axis wind wheel (axis parallel to the flow direction), and the vertical axis wind wheel (axis perpendicular to both ground and air flow direction), which includes two to three wind turbine blades, shown in **Figure 1.1**.Currently, the horizontal axis wind turbine are most used in wind power enterprise [1], because the horizontal axis wind turbine has a high efficiency of wind energy conversion and shorter shaft, these underscore economic advantages on large-scale wind turbines.

Figure 1.1 The horizontal (left) [2] and vertical (right) axis wind turbine [3]

Wind turbine needs to be installed in places which are rich in wind resources, mostly from the sea or hilltop close to the sea. Temperature throughout the year is from above 50 ℃ to below -20 ℃, and the temperature difference between day and night is up to 20 ℃ [4]. The surrounding medium sometimes is high humidity, with salt spray, rain and even hail. The working power source is air, random vary between 4.5 -- 28m/s, sometimes wind speed subjected to maximum 60m / s. In this complex of wind conditions, when the wind turbine is in load operation, key components blades, main bearings and speed increase boxes sometimes will suffer high strength load in several times of the rated load. This instantaneous high-strength load will bring significant impact of wind turbine reliability and lifetime. Sometimes resulting in wind turbine performance degradation, or even damage, as shown in **Figure 1.2**.

Figure 1.2 Wind turbine blade broken [5]

Blade is the core component to transfer wind energy to mechanical energy, as one of the most basic and critical wind turbine components, reaching more than 20% of the overall wind turbine value. Under a complex weather conditions, it is easier to damage the blade more than the entire wind turbine [6-7].

Wind power as a renewable energy, plays a pivotal role in social processes. Maintenance of wind turbines and wind turbine blade testing and diagnosing is gradually attracting people's attention, which has become one of the hot new energy technologies.

Since the 1970s, countries all over the world have entered a golden period of development of wind power. According to the data released by the Global Wind Energy Council, by the end of 2007 the global wind power installed capacity has reached 94 million kilowatts. The ranked top three are Germany, the United States and Spain. The installed capacity of these three countries is above 60% of the world's total installed wind power capacity [8]. According to "2014 Global wind power capacity statistics" issued by the Global Wind Energy Council, in 2014 the global wind power capacity reached 51.477GW, achieving 44% annual growth [9].

It can be seen from all over the world, the number of wind turbines of each country has reached a very large scale. Wind turbine blades are the key components of the wind power generation,

directly affects the performance of the wind power generation system. Wind turbine blades work in the harsh environmenteffected by so many external factors, such as erosion, sand particle, ultraviolet radiation, lightning, which are likely to cause wind turbine blades of vibration, chemical corrosion, cracks, and other issues, which directly affect the safe operation of the wind power enterprise and economic benefits.

Assume that the probability of wind turbine downtime due to blade failure is certain, then such a large number of wind turbines on the basis of wind power companies are faced with a great accident downtime. Therefore, if we can develop a wind turbine blade online mointor and diagnosis, which would greatly avoid unnecessary or unplanned downtime.

Regular, prior detection and diagnosis of turbine blades is the basis for the safe operation of the wind power business, a small amount of investment could avoid huge losses. This thesis will apply radar technology, focusing on the daily operation of the wind power companies facing, vibration, corrosion, and other problems, through the data model analysis, to give a more efficient and accurate detection and diagnosis, to provide repair, maintenance basis and effective protection for the safe operation of wind turbine blades.

1.2 Research Status

Wind Turbine Detection Exploration

In recent years, along with large-scale of wind turbines, wind turbine blade length is increasing. However, the weight of the blade length are three times power related to blade length. Thus, pre-bent and flexible techniques are widely used in blades design. In order to make the generator drive torque and blade wind load reduced, usually designed with a slight bent tip called "flexible" concept. This design can make maximize use of wind energy including low wind speed range and each area of wind speed, and can be increased by 5 to 10% of the capacity to catch the wind. According to the aerodynamic design concept, each cross-section of blade has different twist

angles and the structure of flexible and forward-curved blades in order to reduce weight, thus forming a "bending and torsion elongated structure" blade with modern features. Therefore, under the action of wind, blades are prone to swing vibration, non-linear deformation could lead to instability to cause wind turbine devastating damage. Therefore, during the design of blades, it is necessary to analyze the wind turbine aerodynamic loads and mechanical vibration coupling law [10-13].

Wind turbines operate in harsh environments, varied conditions, even under a variety of pre-estimated situations with the appropriate design, it is difficult to achieve the desired results in actual use, so wind turbines need to be monitored in operating status, with a timely diagnosed to avoid a more serious accident [14-18].

In the actual operation of wind turbine, blades bear the combined effects of centrifugal force, air fluid dynamics, vibration force, temperature stress, medium stress in extremely harsh working conditions, therefore, various failures often occurred in blade.

Such as: ice [19-20], the crack [21-23], pitting [24], wear [25-27] etc.

So far, the most of research are based on the blade surface detection. For example, Marín, who has studied the 300kW wind turbine blade damage and repair [28-29]. Shokrieh and Rafiee using three-dimensional finite element method research whole composites wind turbine blade fatigue failures [30]. Chou, who made fracture analysis of wind loading conditions of wind turbine blades in critical state [31]. From the above research, we try to find a new method to remote monitor the wind turbine blades working condition.

When wind turbine blades rotating, there will be a relative motion occurrence, we can use this property to monitor the wind turbine blades working condition on line. In order to collect blades working information, we use radar to send signal and analyze the receive backscatter signal to online monitor the wind turbine blades working condition. There are many ways to deal with the backscatter signal, the time domain analysis and frequency domain analysis, and there is a modern wavelet transform, short time Fourier transform (STFT), Gabor expansion, the secondary

bilinear frequency distribution, including Spectrogram, Scalogram, Cohen distribution, Wigner-Ville distribution, Choi-Williams distribution [32-36].

For wind turbine blade testing apparatus, a mature program is now only published by Fraunhofer industrial operations and Automation Research Institute in 2009 robot RIWEA [37], as shown in Figure 1.3**,** Figure 1.4**.**

Figure 1.3 Robot RIWEA close FIG [37]

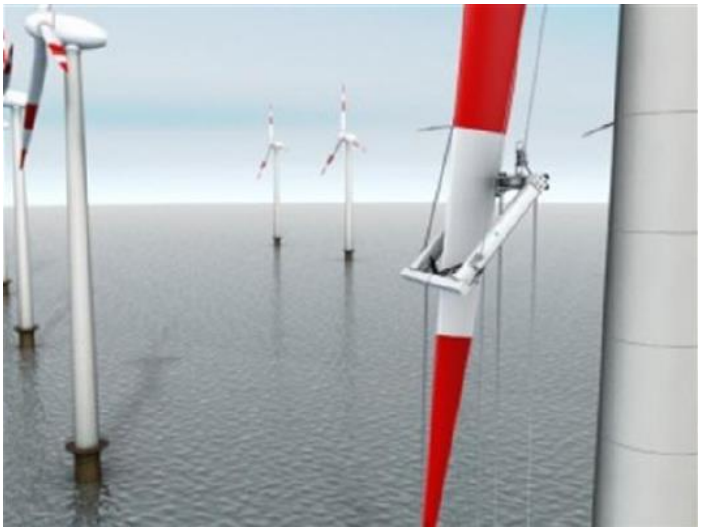

Figure 1.4 Robot RIWEA remote FIG [37]

RIWEA can promote itself to 100 feet (30 meters height), close to the blade surface, using its own advanced sensing equipment give the wind turbine blades accurate measurement checks. Its detection system consists of three components: an infrared emitter indicating wind turbine blade surface temperature, ultrasound systems and high-resolution cameras. RIWEA can use portable ultrasound found the depth of the flaw that maintenance workers cannot find. Through high-precision testing apparatus, RIWEA can detect wind turbine blade surface cracks more accurately than manual process, even find the exact location of damaged parts of the machine.

1.3 Wind turbine blade monitoring method

1.3.1 Wind Power Enterprises Situation

At present, commonly used preventive examinations of wind turbine blades is that after two years of operation, use the opportunity to overhaul the unit and do the whole examination, which includes: clean the blades, blade inner component check.

In addition, for the problem of the naked eye cannot determine the location and size, wind turbine inspectors widespread use ultrasonic flaw detection and laser scatter speckle interferometry to conduct problematic blade [38].

1.3.2 Infrared thermal imaging detection technology

Infrared detector is based on the distribution of temperature to determine the presence and shape of defects. The input variables are material parameters, temperature and spatial distribution of temperature versus time. Output variables are defect shape, size and location[39].

Infrared thermography is inseparable from the support of advanced infrared thermal imaging equipment, which is used to identify, analyse and control infrared information. Infrared detector transfers invisible infrared radiation into a measurable signal, which is a key component of infrared

thermal imaging instruments. It directly affects the detection sensitivity of infrared thermal wave imaging.

According to different thermal loading and heating wave signal acquisition and processing methods, infrared thermography can be divided into pulses infrared thermal wave imaging detection, modulated infrared thermal wave imaging detection, pulsed phase infrared thermal imaging detection and ultrasonic wave/microwave infrared thermography imaging detection.

1.3.3 Ultrasonic detection technology

Ultrasonic testing is a non-destructive testing. Ultrasound can penetrate through the object which radio waves, light waves cannot penetrate, while reflect between two different impedance surfaces, since the object inside is non-uniformity, the ultrasonic attenuates, which can distinguish the defect inside of the object.

Ultrasonic testing is the use of the relationship between object non-sound properties (such as hardness, density, concentration, strength, elasticity, viscosity, flow, level, thickness, defects, etc.) and the acoustic properties of the medium ultrasound (e.g. sound velocity, attenuation, the acoustic impedance). Measure the ultrasound to determine the object non-sound properties[38].

(1) Ultrasonic inspection

Ultrasonic detection is a non-destructive testing method. It can be used without disrupting the object, measuring the effect of propagation by acoustic properties to determine the defections (such as cracks, bubbles, impurities, etc.) in shape and size distribution. Ultrasonic detection technology has high sensitivity, penetration, fast detection, easy operation properties. Ultrasound penetrates opaque solids in tens of meters. When Ultrasonic encountered impurities in the medium, it can produce a strong reflection; and when it encounters moving objects, it can produce Doppler effect. Ultrasonic detection is used in many different ways, according to the its principles, it can be divided into pulse reflection, penetration and the resonance [40].

(2) Ultrasonic Ranging

Ultrasonic Ranging is an ultrasonic method used to detect the distance between known position and the target object surface, which uses the ultrasonic wave propagation and reflection in the media to determine the distance. Since the ultrasonic wave propagation velocity in the general media is much slower than the speed of light, it is relatively easy to determine the propagation time, and it is easy to directional ultrasonic emit and control the intensity and direction. Ultrasonic Ranging is an non-contact measurement utilizing the property of sound waves, electronic counting, and photoelectric switch. It has a very important use in many engineering practice applications, including non-destructive measurement, process monitoring, robot localization and measurement, and liquid level measurement. Transit time is a basic principle of ultrasonic distance measurement, that is

$$D = ct/2 \tag{1.1}$$

Where: D is the distance between the transducer and the obstacle; c is the speed of ultrasonic wave propagation $c = \sqrt{rRT/u}$; r is the ratio of the molecule constant pressure and molecular constant volume heat capacity; R is the gas constant; T is the absolute temperature; u is the molecular weight; t is the time in the ultrasonic propagation medium.

(3) Limitations of ultrasonic detection

If there are particles in the media, these particles are likely to form a number of scattering centers, which produce random distribution echo signal in the time domain, constituting the background noise, interfering to the signal. In practice, the noise reduction methods used are mainly multiple averaging method, matched filter, correlation, spectral analysis. However, due to some non-random noise, these treatments are often less than satisfactory results [41].

1.3.4 Microwave detection technology

Microwave detection technology can be traced back to the 1950s, and in 1990s, it developed rapidly. With the continuous development of new materials and devices, application of electromagnetic waves are also from low to high frequency band, microwave testing is a new detection technology in recent years with the requirement of a variety of non-metallic composite materials in engineering practice.

Microwave detects the metal surface, transmitting signals within the waveguide (device for transmitting an electromagnetic wave) is the main mode TE10 wave, selecting different checkpoints, so that the metal surface is equivalent to a short-circuit load, without cracks, the reflected waves still TE10 wave; when in crack point, the main wave generates higher order modes TM wave (wave of magnetic vector perpendicular to the direction of propagation).

Microwave detection is using the amplitude and phase change of reflected waves to achieve non-destructive testing [42].

Microwave detection, as a new testing method, its advantages are effectively able to detect metal and non-metallic surfaces, long-distance remote testing, very high detection sensitivity and high penetration ability for the non-metal. But microwave testing equipment require a very high sampling frequency, and only high-speed (Digital to Analog) D / A converter can achieve to detect tiny cracks [43].

For non-metallic materials internal detection is mainly using microwave and ultrasonic detection technology, although the ultrasonic detection technology developed, but it requires couplant, which cannot monitor wind turbine motion conditions. For remote measurement techniques, we can use radar to send different waves and receive Doppler signal to analyze and achieve high measurement results.

1.4 The Main Contents

Based on the wind turbine blade design theory and fault diagnosis theory, this study focuses on the design of a running model of wind turbine, in-depth analysis of radar back scattering signals from wind turbine blades to determine the health of the wind turbine blades, providing the basic data for the analysis of the wind turbine blades. Monitor and diagnosis of the whole process is divided into 4 parts—Theory Analysis, Mathematical Modeling, Algorithm Development and Experimental Design. During the study of 4 parts, try to prove the feasibility of this study. This thesis main content is as follows:

Chapter 2 introduces the basic concepts and the principle of each part of radar and target Doppler effect.

Chapter 3 introduces the basic theory of wind turbine as well as the basic concepts and principles of wind turbine air foil aerodynamics and basic theory of wind turbines blade.

Chapter 4 describes the rigid body motion and spatial coordinate representation (Euler angles), Radar cross section (RCS) prediction methods and the calculation method of radar micro Doppler Effect.

Chapter 5 applies of Short Time Fourier Transform diagnosis and analysis of wind turbine blades operation.

Chapter 6 introduces wind turbine blade fault identification based on the Krawtchouk Moment method, using different classification, the method according to the respective frequency range of the wind turbine blade vibration spectrum, doing fault diagnosis. Experimental results show that this method can effectively identify wind turbine blade vibration, corrosion, and selecting reasonable data, can make recognition accuracy rate of over 90%. Finally, proposed future direction of work.

Chapter 7 summarizes the main conclusions, giving different idea of wind turbine blades monitoring.

Chapter 2 Application of Radar Technology and Literature Review

2.1 Radar Working Principle and Classification

In this Chapter, we are going to introduce the basic concepts and the principles of each part of radar and radar Doppler effect.

2.1.1 Introduction of Pulse Radar and Micro Doppler Effect

Basic components of the radar system is shown in **Figure 2.1**. Typically includes a wave form generator, a transmitter, a receiver, A / D (Analog/Digital) conversion, signal processing, data processing, monitor, signal storage and transmission, the antenna, the servo devices, power supply and other components. The waveform generator generates a certain frequency and modulation radio frequency (RF) excitation signal, while sending produced a coherent oscillator signal to a receiver; transmitter amplifies RF excitation signal, and then through the transceiver switch sending to an antenna, radiated by the antenna; and target echo signals via the antenna and transceiver switches to the receiver, then the receiver processes the signal by low noise amplification, mixes the frequency and filters it. The role of signal processing is suppressing noise, interference signals, through coherent and non-coherent accumulation, improve the SNR of the receive signal, and automatic detect and track targets.

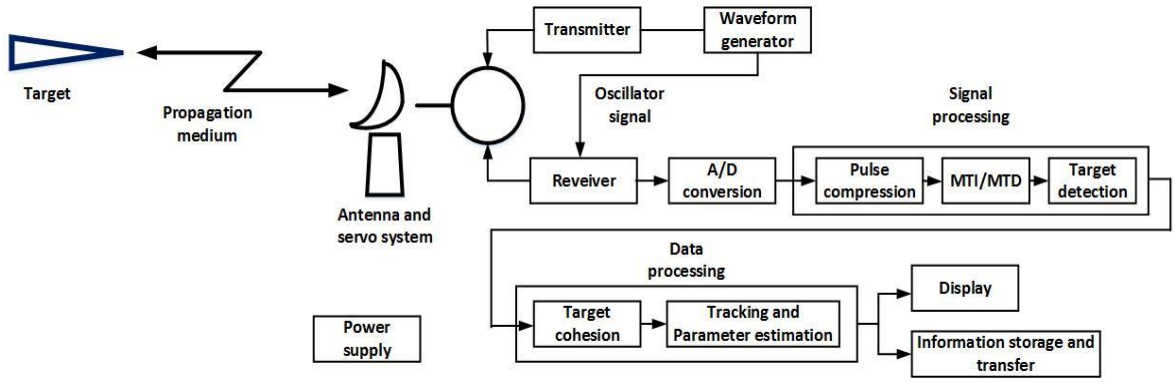

Figure 2.1 The basic composition of the radar system

1. Radar Classification by radar signals

According to the form of radar signal, it is divided into pulse radar and continuous wave radar, and the quasi-continuous wave. According to the signal bandwidth, it can be divided into narrowband radar, wideband radar and ultra-wideband radar. According to the radar coherent property, radar can be divided into coherent and non-coherent radar.

2. Radar operating frequency

The range of radar operating frequency is wide, from a few Megahertz (MHz) to several Gigahertz (GHz). It will be divided into different radar operating frequency band, **Table 2.1** lists the correspondence between the radar band and frequency, as well as the band's main applications and features .According to the operating wavelength, it can be divided into ultrashort wave radar, VHF radar, decimeter radar, centimeter radar, millimeter wave radar.

Table 2.1 Radar operating frequency

Band Name	Frequency(f) range	Wavelength	Main application
HF	3-30 MHz	100-10 m	Over the horizon radar, very far from the target, but with low resolution and accuracy
VHF	30-300 MHz	1000-100cm	Remote monitoring (200-500 km), with moderate resolution and accuracy
UHF	300-1000MHz	100-30 cm	
L	1-2 GHz	30-15 cm	Remote monitoring with moderate resolution and effected by weather
S	2-4 GHz	15-7.5 cm	Medium-range (about 100-200 km) surveillance and remote tracking (about 50-150 km), with moderate precision, severe effect by snow and rain weather
C	4-8 GHz	7.5-3.75 cm	Short-range surveillance, tracking and guidance, high precision
X	8-12 GHz	3.75-2.5 cm	Short-range surveillance, high precision remote tracking, medium-range or short-range in the rain (about 25-50 km)
Ku	12-18 GHz	2.5-1.67 cm	Short range (about 10-25 km) tracking and guidance, specifically for the limited size of the antenna does not need to work all weather condition, widely used in airborne radar systems
K	18-27 GHz	1.67-1.11cm	
Ka	27-40 GHz	11.1-7.5mm	
V	40-75 GHz	7.5-4.29mm	Very short distance (about 1-2 km) tracking, such as automotive collision avoidance and autopilot radar
W	75-110 GHz	4.29-2.7mm	Very short distance (about 2-5 km) tracking and guidance
mm	110-300 GHz	<2.7 mm	Very short distance (about 1-2 km) tracking and guidance

3. Distance

Ordinary radar pulse is to determine the distance from the transmitted signal time which propagates to the target and return. As shown in **Figure 2.2**. Assuming the delay time t, t = 2R / c, the target distance R

$$R = \frac{c \cdot \tau}{2} \tag{2.1}$$

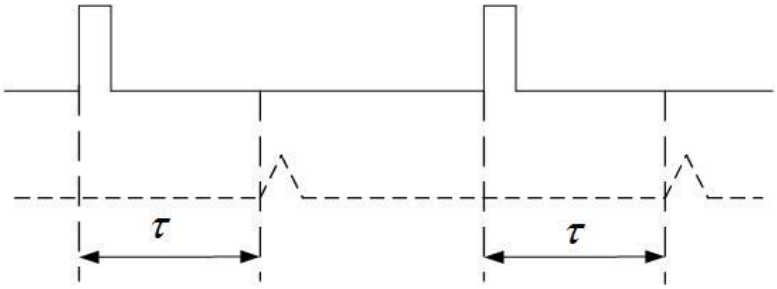

Figure 2.2 Transmitted pulse and target echo schematic

4. Direction (azimuth and elevation)

Direction of the goal is achieved by measuring the front angle of echo wave to the radar. Radar generally use directional antennas that have an arrow band width antenna pattern beam scanning the azimuth and elevation dimension. When the received signal is in the maximum energy, the antenna direction is the target direction.

Direction of the incident wave front can be determined by measuring the received phase difference by the two separate antennas and the phase difference depends on the angle between the incident wave front and the connection of two antennas.

5. Doppler frequency

When there is relative motion between the target and the radar, the radar transmit signal frequency is f_0, then the received signal is $f_0 + f_d$, f_d is the Doppler frequency. Due to this movement of the target relative to the radiation source causes a change in the frequency of the echo signal which is called the Doppler effect. As shown in **Figure 2.3**, when the target motion toward the radar, the Doppler frequency is positive; when the target away from the radar, the Doppler frequency is negative. The wave form on the

target with an equal interval of lambda and phase. The target approaching the radar lead each equiphase wavelength close, lambda> lambda '(lambda' is reflection wavelength); Vice versa, lambda<lambda'.

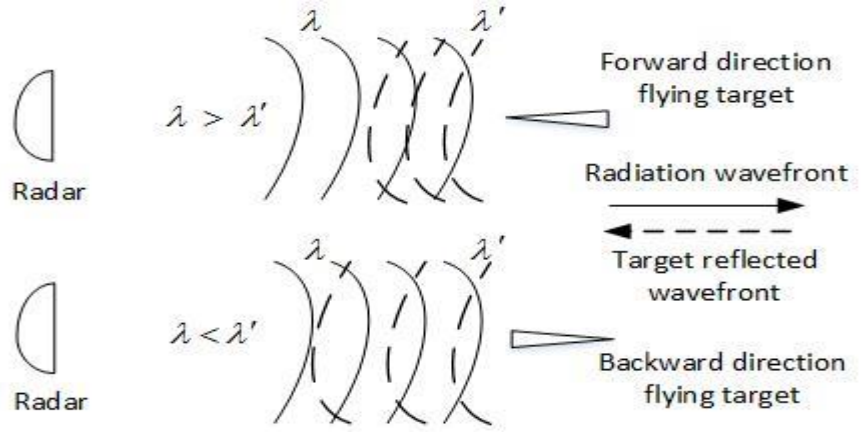

Figure 2.3 Doppler effect (moving target reflected the equiphase wavefront of the reflected wave)

Assumed the radar transmit pulse width is τ, corresponding beam path length $L = ct$ (cis the speed of light), the radial velocity of the target is v_r, as shown in **Figure 2.4**, the time interval between the front edge and the trailing edge of the pulse arriving at the target is Δt, in time of Δt, the distance of the target move in the pulse is $a = v \cdot \Delta t$. Since the pulses propagate in the speed of light, the trailing edge has moved the distance $ct - a$, then

$$c\tau = c\Delta t + v_r \Delta t \tag{2.2}$$

$$c\tau' = c\Delta t - v_r \Delta t \tag{2.3}$$

By the Equation(2.3), the relation of the reflected pulse width and incident pulse width is

$$\tau' = \frac{c - v_r}{c + v_r}\tau \tag{2.4}$$

Where, $\frac{c - v_r}{c + v_r}$ referred as time spreading factor. If $v_r = 0$, $\tau' = \tau$. Similar, when the target away from the radar, the relationship between the reflected and the incident pulse width is

$$\tau' = \frac{c + v_r}{c - v_r}\tau \tag{2.5}$$

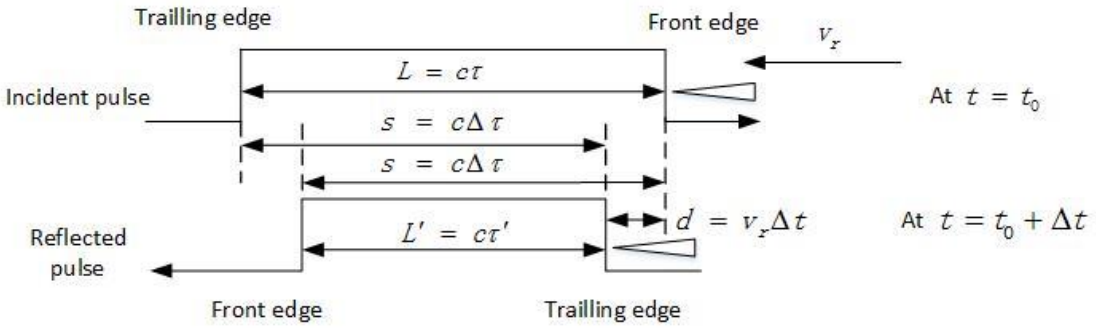

Figure 2.4 The impact of the moving object to emitting pulses

In order to derive the Doppler frequency, consider the case of two pulses shown in **Figure 2.5**, assuming that two incident pulse repetition frequencies (PRF) is f_r, after the leading edge of the pulse 1 reach the target, pulse 2 leading edge takes time Δt reach the target, radio propagation distance is

$$\left(\frac{c}{f_r}\right) - v\Delta t \tag{2.6}$$

And pulse2 leading edge delay distance in time Δt is $v\Delta t$,

$$\frac{c}{f_r} - v\Delta t = c\Delta t \tag{2.7}$$

Simplified,

$$\Delta t = \frac{c/f}{c+v}, \quad v\Delta t = \frac{vc/f}{c+v} \tag{2.8}$$

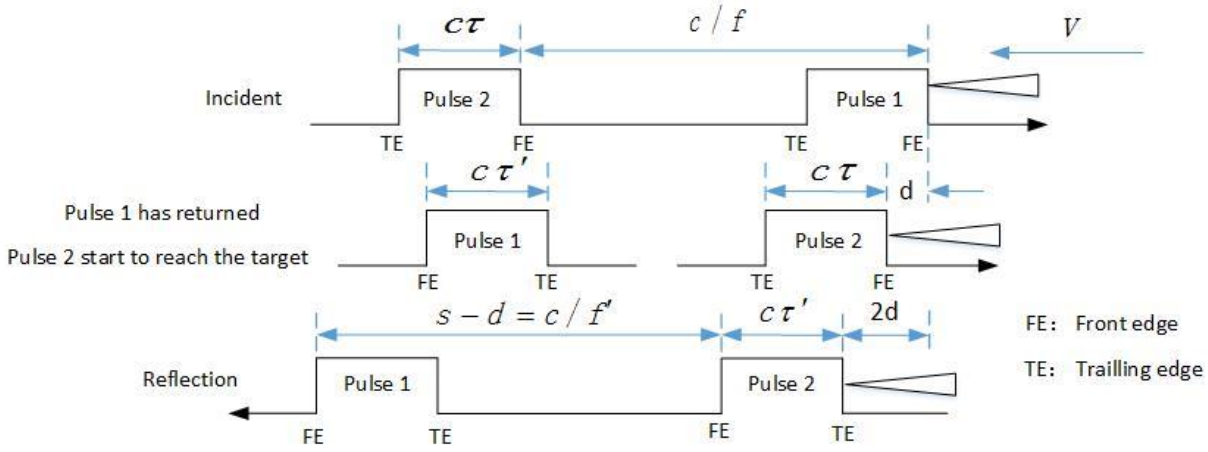

Figure 2.5 Effect of target motion one mission pulses

The reflected pulse interval is T' and wave path is $c\Delta t - v\Delta t$, the echo pulse repetition frequency $f' = 1/T'$,

$$c\Delta t - v\Delta t = c\Delta t - \frac{vc/f}{c+v} = \frac{c}{f'} \tag{2.9}$$

Thus, the relationship between the echo pulse PRF and incident pulses PRF is

$$f' = \frac{c+v}{c-v} f \tag{2.10}$$

As the number of cycles is constant, frequency of the reflected signal is increased by the same factor and the relationship between the echo signal carrier frequency f_0' and incoming signal carrier frequency f_0 is

$$f_0' = \frac{c+v}{c-v} f_0 \tag{2.11}$$

Doppler frequency is defined as difference between echo signal carrier frequency f_0' and signal carrier frequency f_0,

$$f_d = f_0' - f_0 = \frac{2v}{c-v} f_0 \tag{2.12}$$

Due to $v \ll c$, and lambda $\lambda = c / f_0$,

$$f_d \approx \frac{2v}{c} f_0 = \frac{2v}{\lambda} \tag{2.13}$$

Doppler frequency is related to the angle between the radar line of sight and the target movement direction, when the angle between the radar line of sight and the direction of target movement is θ . $v = v_t \cos\theta$, is target speed projected onto the radar line of sight, as shown in **Figure 2.6**, the Doppler frequency

$$f_d = \frac{2v_t \cos\theta}{\lambda} \tag{2.14}$$

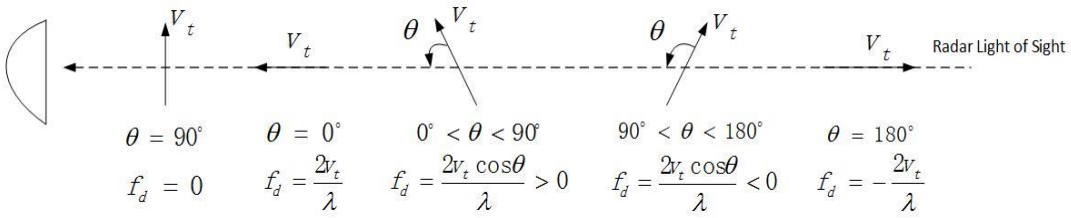

Figure 2.6 Relationship between the radar line of sight and Doppler frequency

2.1.2 Estimation and Analysis of Doppler Frequency Shift

Doppler radars utilize the Doppler effect to measure the radial velocity of a target. The Doppler frequency shift can be extracted by a quadrature detector that produces an in-phase (I) component and a quadrature phase (Q) component from the input signal.

In the quadrature detector, the received signal is split into two mixers called synchronous detectors. In the synchronous detector I, the received signal is mixed with transmitted signal; in the other channel it is mixed with a 90^o shift of the transmitted signal.

If the received signal is expressed as

$$s_r(t) = a\cos\left[2\pi(f_0 + f_D)t\right] = a\cos[2\pi f_0 + \varphi(t)] \tag{2.15}$$

Where, a is the amplitude of the received signal, f_0 is the carrier frequency of the transmitted signal, $\varphi(t) = 2\pi f_D t$ is the movement phase of the received signal due to the target shift.

By mixing with the transmitted signal

$$s_t(t) = \cos(2\pi f_0 t) \tag{2.16}$$

Output of synchronous detector I is

$$s_r(t)s_t(t) = I(t) = \frac{a}{2}\cos\left[4\pi f_0 t + \varphi(t)\right] + \frac{a}{2}cos\varphi(t) \tag{2.17}$$

After low pass filtering, the I-channel output is

$$s_r(t)s_t(t) = I(t) = \frac{a}{2}cos\varphi(t) \tag{2.18}$$

The received signal by mixing with the 90° phase shifted transmitted signal, the Q-channel output is

$$s_r(t)s_t^{90^\circ}(t)Q(t) = -\frac{a}{2}sin\varphi(t) \tag{2.19}$$

Combining the I and Q outputs, a complex Doppler signal can be formed by

$$s_D(t) = I(t) + jQ(t) = \frac{a}{2}\exp\left[-j\varphi(t)\right] = \frac{a}{2}\exp(-j2\pi f_D t) \tag{2.20}$$

Thus, the Doppler frequency shift f_D can be estimated from the complex Doppler signal $s_D(t)$. The periodogram can be used to calculate the spectral density of the signal. Then the maximum likelihood estimation can be applied to locate the maximum of the periodogram.

From the estimated Doppler frequency, the radial velocity of the target is determined by

$$v = \frac{\lambda}{2}\hat{f}_D = \frac{c}{2f}\hat{f}_D \tag{2.21}$$

Modulated continuous wave (FM-CW) and coherent pulsed Doppler radars can have wide frequency bandwidth to gain a high-range resolution and measure both the range and Doppler information.

1. Resolution

Resolution refers to the ability to distinguish two adjacent targets. Radar typically includes two-dimensions of distance and azimuth, and even includes elevation and speed dimensions. In this four-dimensional, as long as one can distinguish the target is resolved. For distance dimension, the two targets are at the same angle but at different distances. For pulse radar, when the trailing edge of the first target and the leading edge of second echo pulse close to that, it cannot distinguish between the two targets, as a distinguished limit, the limit distance is the distance resolution. Distance resolution is generally represented by R,

$$\Delta R = \frac{c \cdot \tau}{2} = \frac{c}{2B} \tag{2.22}$$

Where τ is the transmit pulse width. It can be seen that the narrower pulse width or the wider bandwidth B of the transmitted signal, the smaller the R value, the higher range resolution.

Radar systems are usually designed to work in minimum distance $R_{\min}$ and maximum distance $R_{\max}$, $R_{\min}$ and the distance between and $R_{\max}$ is divided into M range gates and the width of each range gate R is

$$M = \frac{R_{\max} - R_{\min}}{\Delta R} \tag{2.23}$$

When the two targets are at the same distance, the angular position is different, angular resolution is defined that the smallest angle can be distinguished (the resolution in the horizontal plane called azimuth resolution, the resolution in the vertical plane called the pitch angular resolution). It is related to the beam width, the narrower the beam, the higher the angular resolution. Half-power beam width $\theta_{0.5} \approx \frac{\lambda}{D}, \lambda$ is the wavelength, D is the effective aperture of the antenna.

Figure 2.7 shows the schematic diagram of the target resolution, in "Case1", two targets in the same distance unit, it is indistinguishable in distance dimension, but it can be distinguishable in azimuth dimension; In "Case2", two targets in the same orientation unit, it is indistinguishable in the azimuth, but it can be distinguishable in distance dimension; In “Case3”, two targets in the different distance unit and different orientation unit. It can be distinguishable in distance dimension or azimuth dimension.

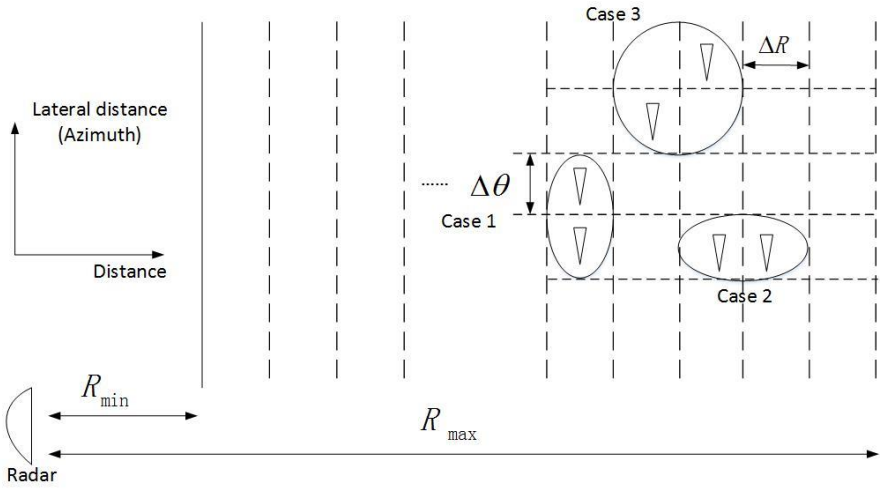

Figure 2.7 Target resolution schematic

2.1.3 The Composition of The Radar System and Function

The basic block diagram of the radar system shown in **Figure 2.8**, includes an antenna and servo control, transmitter, waveform generator, a receiver, a signal processor, data processor, terminal display and other equipment. Functions of each part are briefly summarized below:

Antenna. This radiates the power signal, and receives the target scattering signal.

Waveform generator. Also called the frequency synthesizer. Produces 10mW to 1WRF excitation signal to the radar while providing a coherent oscillator signal.

Transmitter. High power transmission parts. Amplify and filter the RF excitation signal.

Receiver. A low-power receiving portion. The received signal power is generally in the rank of μW to mW , amplify the received signal, mix frequency and filtering.

Signal processor. Process echo signals to improve the signal to noise ratio, while suppressing noise and interference, and detect the target.

Data processor. Manages tracking and tracking filter for test results.

Terminal display and data transmission. Displays received signal, shows original video, and tracking information.

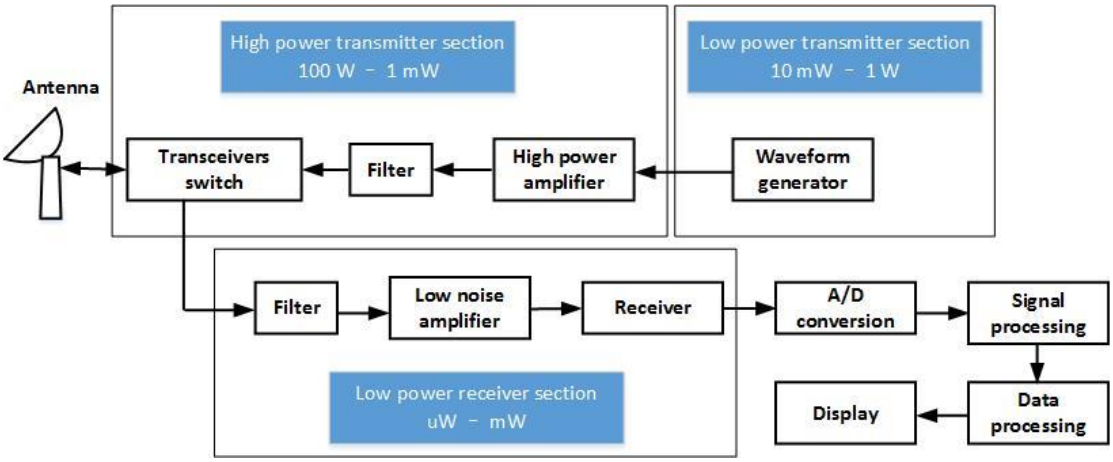

Figure 2.8 The basic block diagram of the transponder system

Radar Transmitter

Radar is to use the object reflected electromagnetic waves to detect and determine the parameters of distance, azimuth, altitude and speed of the target. Therefore, the radar transmitter requires a specific power signal. Radar transmitters provide a carrier signal modulated by high-power radio frequency, through the feeder and the transceiver switches radiated by the antenna.

Radar transmitter has two types -- single-stage oscillating and M.O.P.A.(**Master Oscillator-Power Amplifier)** transmitter, as shown in **Figure 2.9**, the high-power RF signal provided from the primary high-power RF oscillator, controlled by pulse modulation, and therefore the output of the

oscillator is the modulated high-power radio frequency signal. Normally, pulse radar radiation is a high-power radio frequency signal modulated by a rectangular pulse.

M.O.P.A. transmitter has multi-level. First, the master oscillator generates a low-power RF signal; then amplifies the RF signal, increases the signals power level; this is called the RF amplifier chain.

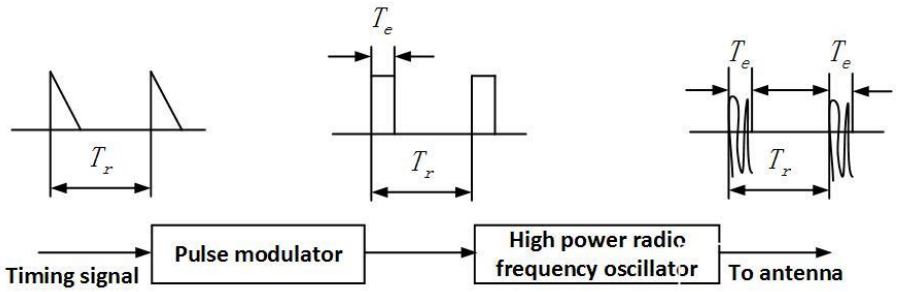

Figure 2.9 Single-stage oscillating transmitter

The pulse of the master oscillator amplifier is actually cut from a continuous wave. If the controlled switch clock is generated as a reference of oscillator clock, then the pulse is coherent. For the pulse signals, coherence means from one pulse to the next pulse having phase consistency. If the initial phase between pulses is random, the transmitted signal is incoherence.

The RF amplifier chain typically using a multi-stage amplifier. The final stage of high power amplifier soften use multiple amplifiers in parallel, and then through a power synthesizer to reach the transmit power required.

Output Power

Transmitter output power directly impacts on radar power and anti-interference property. Usually the output power from the transmitter to the antenna is the transmitter power.

Output power of the pulse radar transmitter can be divided into peak power P_t and average power P_{av}. P_t is the average output power of amplified RF during transmit pulse, P_{av} is an average output power within the pulse repetition period. If the transmitted wave form is a simple rectangular pulse modulation, transmit pulse width is t, and the pulse repetition period is T, then

$$P_{av} = P_t \frac{t}{T} = P_t t f \tag{2.24}$$

Where $f = 1/T$ is the pulse repetition frequency, $t/T = D$, called radar Work ratio. Continuous wave radar D = 1.

Radar Receiver

The task of the radar receiver is to use appropriate filtering to filter the received weak high frequency signal from antenna, and after filtering, amplification, mixes the frequency, then after detection, it is sent to the signal processor. The radar receiver can be classified by design, function and structure. Generally the radar receiver can be divided into four types—superheterodyne type, super-regenerative type, crystal type and tuner high-frequency (TRF) type.

Superheterodyne radar receiver simplify block diagram shown in **Figure 2.10**. Its major components are: 1. high frequency part, also known as the receiver "front end", which includes a receiver protection, low-noise high-frequency amplifier, mixer and a local oscillator; 2. intermediate frequency amplifier, including the matched filter device; 3. detector and video amplifier.

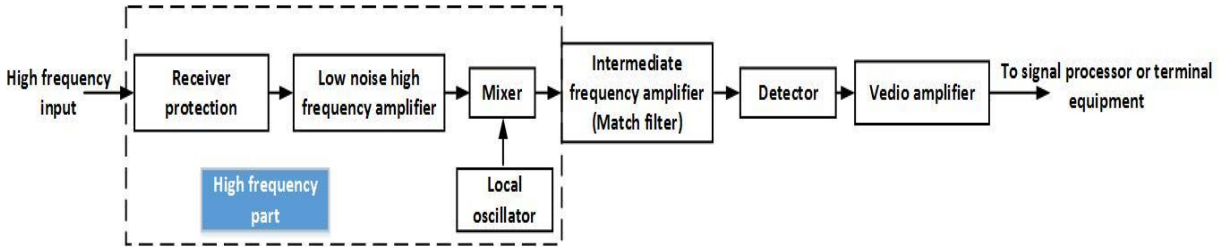

Figure 2.10 A simplified block diagram of superheterodyne radar receiver

2.2 Radar Cross Section (RCS)

Radar discovers targets by targets scattering power. In general, RCS is defined as intensity of the target scattered energy. In order to describe the target back scattering characteristics, define the "point" target RCS σ is,

$$\sigma = \frac{P_s}{S_e} \tag{2.25}$$

Where, P_s is the target scattering power, S_e is irradiation power density. This is a defining equation, the total power is not dependent on target scattering power P_s and irradiation power density S_e .

As shown, due to scattering, unit angle power P_r at the receive point of is

$$P_r = \frac{P_s}{4\pi} = S_e \cdot \frac{\sigma}{4\pi} \rightarrow \sigma = 4\pi \cdot \frac{P_s}{S_e} \tag{2.26}$$

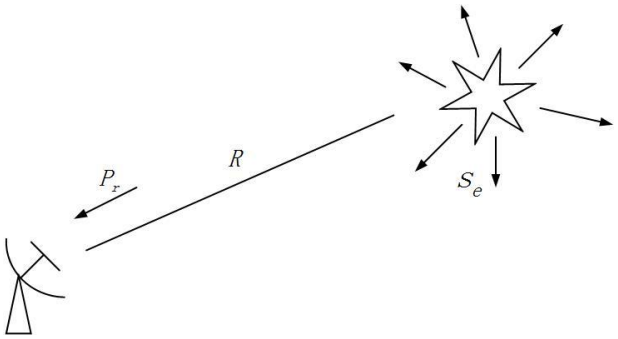

Figure 2.11 Target scattering properties

Therefore, σ can be defined as: In the far field (plane wave illumination) conditions, σ equals to 4π multiplied the ratio of the scatter radiation intensity to the incident power density in a specific direction. In order to better explain the meaning of σ , by definition considered a good conductive properties of isotropic spheres sectional area. Power density S_1 at the incident, spheres geometric projection area is A_1 , intercepted the target power is $S_1 A_1$. It uniform radiates power into the solid angle, according to the Equation(2.26), defined sphere RCS as

$$\sigma = 4\pi \left[\frac{S_1 A_1 / (4\pi)}{S_1} \right] = A_1 \tag{2.27}$$

Equation(2.27) shows that good conductivity isotropic spheres, its geometrical scattering cross section is equal to the projected area of the sphere. Any reflector's RCS can be equivalent to a cross-sectional area of isotropic sphere. In the receiver direction, targets RCS is equivalent to a lossless uniform radiation cross-sectional area (projected area). Because the complex shape of the actual target, its back scatter characteristics are synthesized various parts of the vector scattered, and different illumination direction has a different RCS. In terms of complex targets, σ not only with the emitter direction at launch, but also depends on the scattering direction at receiver.

2.2.1 RCS of Simple Shape Targets

For targets of simple geometry, such as, circular plate, cone, etc., its RCS can be calculated. For non-spherical target, the RCS is related to perspectives. In all simple target, spheres have a simple shape, and its RCS is not related to perspectives, in common, conductive sphere of target as a standard measure of RCS.

Figure 2.12 shows the relationship between ideal RCS conductive sphere and wave number (or wavelength). The vertical axis represents the normalization back scatter RCS that is the ratio of RCS and the projected area.

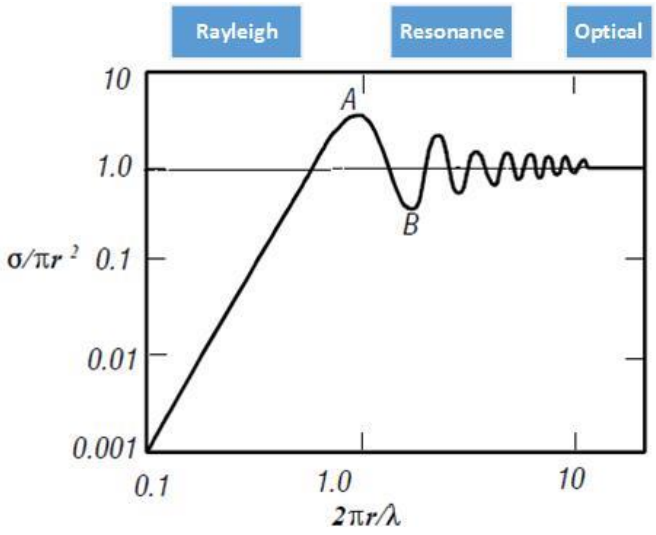

Figure 2.12 Relationship between Back scatter RCS and wave numbers

In **Figure 2.12**, RCS can be divided into three regions[44]:

(1) Rayleigh region (Radius of the sphere is far smaller than the wavelength, $2\pi r / \lambda < 1$)

Since the wavelength in the Rayleigh region is long enough that only a portion of the field gradient to inspire current on the sphere surface. For a small sphere in Rayleigh region, its RCS is proportional to the sixth power of the radius, and is inversely proportional to the fourth power of the wavelength, i.e.

$$\sigma = 9\pi r^2 \left(\frac{2\pi r}{\lambda} \right)^4 \quad r << \lambda \ , \quad \lambda > 10r \tag{2.28}$$

The majority of radar targets are not in this area, but weather particles are in this area for common radar waveform (their size is much smaller than the wavelength). Target in Rayleigh region, the main parameters of their RCS is the volume rather than the shape, in general, the size of the radar target is much greater than the cloud particles, thus reducing the operating frequency of the radar echo can reduce the impact of clouds and rain.

(2) Resonance region ($1 < 2\pi r / \lambda < 10$), the region between the Optical region and Rayleigh region, RCS has large oscillation, when the perimeter $2\pi r = \lambda$, RCS reaches a peak $\sigma = 3.7\pi r^2$. This resonance phenomenon can be explained by the physical interference between the incident and creeping wave, creeping wave and the front surface of the sphere to form an interference.

(3) Optical region (Radius of the sphere is far smaller than the wavelength, ($2\pi r / \lambda > 10$)

In fact, most of radar targets are in the optical area. The target wavelength is much larger than the wavelength, if the target surface is smooth, and target RCS may be determined by the geometrical optics principle. In accordance with the principles of geometric optics, the surface area is the strongest reflection of electromagnetic waves on a small area in front of the most salient points, the size of this area is proportional to the radius of curvature ρ of the point, the greater the curvature, the greater the reflection region, the reflection region optically called "bright spots."

2.2.2 Radar Cross Section (RCS) of Complex Shape Targets

When the electro-magnetic wave radiates onto the target, the electro-magnetic scattering occurs. The incident electro-magnetic wave on the surface of the target and (or) in vivo induce electro-magnetic currents, resulting in a scattered electro-magnetic field. The scattered electro-magnetic wave is transmitted to all possible directions. If the target is at a sufficient distance away from the radar, the incident wave front may be regarded as a plane wave. To measure scattering of electromagnetic waves by using a target power bistatic scattering cross section. If the scattering direction is return to the radar, the bistatic scattering into backscatter and backscatter cross-sectional area is the cross-sectional area, known as the radar cross section (RCS).

According to, "IEEE Institute of Electrical and Electronic Dictionary defines RCS as a target reflection intensity, is defined as 4π multiple of the power ratio of per unit solid angle of the scattered power in the specified direction to the per unit incident plane wave from the specified direction. "RCS with the formula described as $\sigma = \lim_{r\to\infty} 4\pi r^2 \frac{|E_s|^2}{|E_i|^2}$ [45], here E_s is the strength of the far-field scattering electric field, E_i is far-field intensity of the incident electric field, r is the distance from the radar to the target.

RCS is defined to characterize the properties of the target. It was normalized to the incident power density at the target, regardless of distance from the radar to the target. RCS depends on the size of the target, geometry and materials, the transmitter frequency, polarization transmitter and receiver respectively, as well as the perspective of target relative to the radar transmitter and receiver[46-47].

The maximum detectable distance of the target is proportional to the fourth root of its RCS. RCS unit is usually described by the square meter (m^2).

When the electro-magnetic wave irradiate the target, each building block generates a voltage. Building Blocks voltage vector and value determine the overall RCS targets. It is defined as the

square root of the magnitude of the vector sum. RCS accuracy depends on the accuracy of these building blocks and modeling.

The target electro-magnetic scattering mechanism is a complex process, including reflection, diffraction, wave, conduction, and the interactions between them. Emit from the surface, having the highest RCS in the scattering mechanism. Diffraction from intermittent (such as edges, corners or vertices), is weaker than reflection. Along the target surface is propagation surface currents. Leakage wave on a flat surface, a creeping wave on a curved surface. When the wave enters like wave guide structures (such as aircraft air intake) conduction occurred. Spiked features and side lobe RCS may also be from the multiple reflection, diffraction and other scattering mechanisms.

2.2.3 RCS Prediction Methods

RCS prediction method is an analytical method to calculate RCS. An incident wave causes the target current, and radiates electro-magnetic waves. If the current distribution is known, it can be used as the radiation integral to calculate scattering field and RCS. RCS prediction methods commonly used physical optics (PO), ray tracing, and the finite difference method [47]. Physical Optics is a high-frequency approximation method to estimate the induced currents on the object surface.

In this thesis, we use mono-static RCS to determine the object backscatter electromagnetic power flux density. The wind turbine blades are formed by a lot of continuous subdivision surfaces (rectangular mesh). The objects total RCS are superimposed square root of each individual surface of RCS. Scattering of each rectangle with the assumption that the rectangle is isolated from other rectangles.

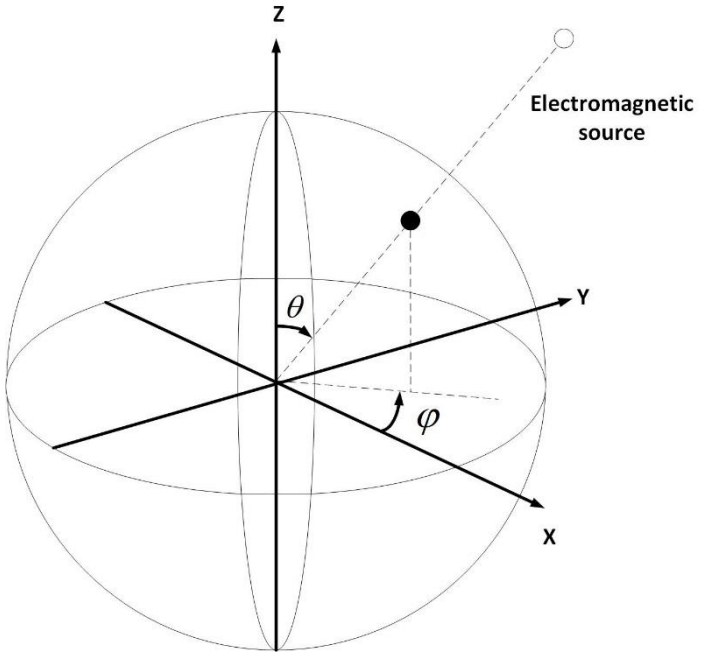

Figure 2.13 RCS prediction in Spherical coordinates

In addition, without considering multiple reflections and edge diffraction and surface waves. Block only with the surface is either completely illuminated by the incident or completely obscured. As shown in **Figure 2.13**, the standard spherical coordinate system is used on a Physical Optics surface RCS prediction with specific incident and scattering directions, RCS is calculate data specific angle θ and ϕ .

The large size complexity target can often be approximated decomposed into a number of independent scatterers, **Figure 2.14** shows an experiment with wind turbine blades built by some simple rectangular geometry blocks.

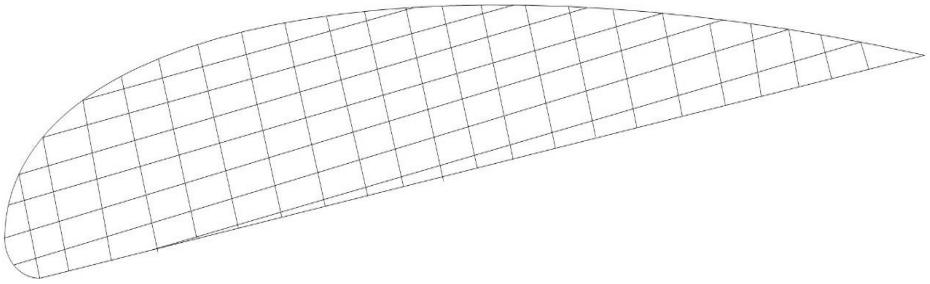

Figure 2.14 wind turbine blade geometric components model

The size of each individual scatterer is in the optical area; there is no interaction between the various parts, and under such conditions the overall RCS is the sum of various parts of RCS,

$$\sigma = \left| \sum_k \sqrt{\sigma_k} \exp(j \frac{4\pi d_k}{\lambda}) \right|^2 \tag{2.29}$$

Where σ_k is the k-th scatterer RCS, d_k is the distance between the k-th scatterer to the antenna.

In this Chapter, we have introduced the radar working principle and have introduced RCS to analyze the object operational status which provides a theoretical basis for measuring wind turbine blade working condition.

2.3 Introduction of Signal Analysis Based on Discrete Orthogonal Moment.

Currently, an important research direction in mathematics field of image processing and analysis is to use the shape of the image features. Moments function is an effective image shape descriptors. It can be widely used in classification of objects, position estimation, image coding and image reconstruction [48]. A setof moment values calculated from a digital image, usually represents all characteristic features of the image, providing all the useful information about the image geometric features. A set of invariants can be obtainedfrom the moment function , when images translation or rotated, the moments will not be changed. thus the moments can be extracted as the target feature vectors.

By calculating the image moment invariants can easily extract rotation invariant characteristics. Since 1962, Hu constructed seven set of invariants moments used for image analysis [49]], Teague proposed the concept of orthogonal moments in 1980 [50], which orthogonal Zernike moments and Legendre moments solve information redundancy when geometric moments extract image

information. However the continuous moment in analyzing the digital images are inevitably generating discrete distortion. In 2003, Yap [51], proposed the discrete orthogonal Krawtchouk moments can avoid distortion caused by discrete, which is suitable for digital image processing.

In this section, the theory of defining the Krawtchouk moments is introduced, followed by the feature extraction algorithm.

Krawtchouk moment has the ability to extract local information. This can be achieved by changing the parameters of the binomial distribution polynomial p in Krawtchouk polynomial. Classical Krawtchouk polynomial is defined as [51]:

$$K_n(x;p,N)=\sum_{k=0}^{n}a_{k,n,p}x^k={}_2F_1(-n,-x;-N;\frac{1}{p}) \tag{2.30}$$

Where, $x,n=0,1,2,...,N, N>0, p\in(0,1).$, ${}_2F_1(\cdot)$ is Gauss Hyper geometric function and it is defined as

$${}_2F_1(a,b;c;z)=\sum_{k=0}^{\infty}\frac{(a)_k(B)_k z^k}{(c)_k}\frac{z^k}{k!} \tag{2.31}$$

Where $(a)_k$ is Pochhammer function, defined as

$$(a)_k=a(a+1)(a+2)...(a+k-1)=\frac{\Gamma(a+k)}{\Gamma(a)},(a)_0=1 \tag{2.32}$$

(N + 1) Krawtchouk polynomials $\{K_n(x;p,N)\}$ constitute a set of weighted discrete function:

$$w(x;p,N)=\binom{N}{x}p^x(1-p)^{N-x} \tag{2.33}$$

Its orthogonality:

$$\sum_{x=0}^{N} w(x;p,N)K_N(x;p,N)K_m(x;p,N) = \rho(n,p,N)\delta_{nm} \tag{2.34}$$

Where, $n,m = 1,2,...,N$,

$$\rho(n;p,N) = (-1)^n \left(\frac{1-p}{p}\right)^n \frac{n!}{(-N)_n} \tag{2.35}$$

The parameter p represent a shift parameter, p deviates from the value 0.5 by Δp ,the weighted Krawtchouk polynomials are approximately shifted N Δp [63]. This characteristic can extract local information in the image.

To avoid excessively large range of values, introduce weighted normalized Krawtchouk orthogonal polynomials:

$$\bar{K}_n(x;p,N) = K_n(x;p,N)\sqrt{\frac{w(x;p,N)}{\rho(n;p,N)}} \tag{2.36}$$

Considering a 2D function of $f(x,y)$, with x and y numbers in the sets in the sets (1,N) and (1,M) respectively. M and N represent the image wide and height samples. Order of (n ,m) Krawtchouk moment is defined as:

$$Q_{nm} = \sum_{x=0}^{N-1}\sum_{y=0}^{M-1} \bar{K}_n(x;p_1,N-1)\bar{K}_m(y;p_2,M-1) f(x,y) \tag{2.37}$$

Inverse transform as follows:

$$f(x,y) = \sum_{n=0}^{N-1}\sum_{m=0}^{N-1} Q_{nm}\bar{K}_n(x;p_1,N-1)\bar{K}_m(y;p_2,M-1) \tag{2.38}$$

It can be seen that the moments provide limited set of values to represent a 2D function.

General expression of rotation invariant continuous moments

Bhatia and Wolf has pointed out [52-53], a complex exponential polynomial rotating about the origin, remains the same, having the following form:

$$V(r\cos\theta, r\sin\theta) = g_p(r)\exp(jq\theta) \tag{2.39}$$

Where $g_p(r)$ is a polynomial about r with order p. If density function $f(x, y)$ represents image in Cartesian coordinates, used $f(r, \theta)$ represents it in polar coordinates, and $g_p(r)$ is the radial polynomial equation, thus defined continuous orthogonal moments are rotation invariant moments.

The typical general form is:

$$F_{pq} = \int\int f(r, \theta)g_p(r)e^{jq\theta}rdrd\theta \tag{2.40}$$

Where F_{pq} represents the order of pq moment, is a function of radius r and p and q are integers.

If the image along the center rotating angle α, that is the image functions $f(r, \theta)$ become $f(r, \theta + \alpha)$, the moment $f(r, \theta + \alpha)$ is:

$$F'_{pq} = \int\int f(r, \theta)g_p(r)e^{jq(\theta+\alpha)}rdrd\theta \tag{2.41}$$

$$F'_{pq} = F_{pq}\exp(-jq\alpha) \tag{2.42}$$

As can be seen from the above equation, $\|F_{pq}\| = \|F'_{pq}\|$, $\|F_{pq}\| = \sqrt{F_{pq} \cdot F^*_{pq}}$ (* denotes a complex conjugate) has rotation invariance property.

Chapter 3 The Basic Concept of Wind Turbines and Blades Common Problems

3.1 The Main Parameters of Wind Turbine Machine

Wind turbines transfer wind energy into electrical energy, mainly consists of the impeller, hub, transmission, generator, tower and other institutions, as well as connected grid electrical components and control components, as shown in **Figure 3.1**. Unit capacity of wind turbines is growing, the larger the blade swept area and quality of the cabin, the more design and operation of various parameters is to be considered.

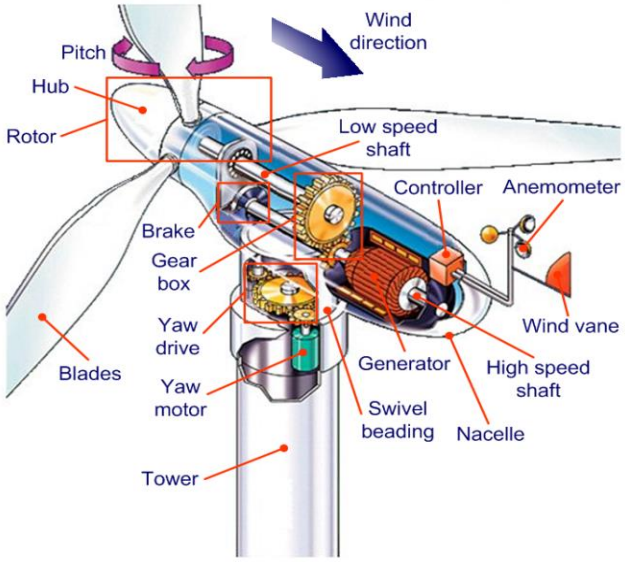

Figure 3.1 The main structure of wind turbine [54]

As shown in **Table 3.1**, with1.5MW horizontal axis wind turbine, for example, wind turbines main parameters are as follows [55]:

The annual average wind speed at hub height is 8.5 m / s, wind speed vertical gradient is 8 deg.

Table 3.1 1.5MW horizontal axis wind turbine main parameters [56]

Item	Parameter Value	Unit
Rated power	1500	kW
Wind wheel diameter	70	m
Tower height	82	m
Number of Blades	3	-
Hub height	84	m
Wind wheel angle	5	deg
Wind wheel cone angle	0	deg
Transmission form	Gear box	
Pneumatic control	Pitching	
Variable speed/fixed speed	Variable speed	
Nacelle diameter	3.5	m
Staging Speed	3	m
Cut-out speed	27.6	m
Wheel speed extreme state	42.5	m
Winds hear index	0.2	

3.2 Basic Concepts of Wind Turbine Blades and Blade Vibration Related Theories

Wind turbine blades are one of the main components of a wind turbine, which involves many parameter. This chapter describes about wind turbines basic concepts and terminology of the blade

1. **Blade.** Blade is the basic components to absorb wind energy. Blade airfoil, twisted, tip speed ratio and the number of blades have a direct impact on the efficiency of wind energy.

2. **Blade rotation plane.** The round plane rotation of the blades.

3. **Wind wheel diameter.** Blades rotation swept surface diameter, also known as blade diameter.

4. **Wind wheel.** Assembly of wind turbine blade mounted on the hub.

5. **Wind energy utilization factor.** Wind turbine absorbs the extent of nature wind energy used the power coefficient C_ρ:

$$C_\rho = \frac{P}{\frac{1}{2}\rho A v_1^3} \tag{3.1}$$

Where, P --the power of wind turbine shaft, W

ρ --air density kg / m^3

A --blade swept area m^2

v_1 --wind speed in front wheel m / s

6. **Tip speed ratio** λ . The ratio of speed of the tip of blades and wind speed v, represent the state of wind wheel rotation indifferent wind.

$$\lambda = \frac{V}{v} = \frac{2\pi Rn}{60v} \tag{3.2}$$

Where, V --tip speed of blade m/s

v --wind speed m/s

n --blade rotating speed r/min

R --blade rotating diameter m

3.2.1 Blade Material, Structure and Manufacturing Process

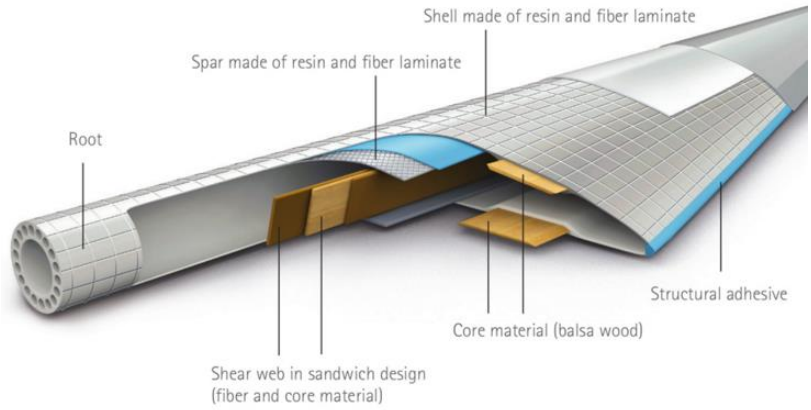

Figure 3.2 Wind turbine blade cross section view [57]

Wind turbine blades have a variety of materials, and material strength of the blade is the key to the performance of the wind turbines. It also determines the intensity of radar signal scattering.Current blades materials have wood, fiber-reinforced plastic cover wood and fiber-reinforced plastic hollow or filled, foamed material, metals (aluminum) blades. Glass-fiber reinforced composites is the most common used one.

Wind turbine blades are shell structure, as shown in Figure 3.2. It is divided into three parts. (1) Root: The material is generally using metal; (2) Shell: generally made by fiberglass; (3) the keel (ribs or reinforcing frame).

The purpose of this design is wind turbine blades to withstand greater loads, usually considered extreme wind 50 ~ 60m / s. In order to improve the strength and stiffness of the blade, or even to prevent local instability. The main beam bears most of the bending load, and the shell also bears some of the load except for the aerodynamic performance.

3.2.2 Airfoil Geometry and Aerodynamic Characteristics

Figure 3.3 Airfoil Terminology[58]and **Figure 3.4** shows the cross-sectional view of airfoil that cross-section along the blade chord direction. Airfoil on coming stream wind speed is v, and direction of wind speed is assumed in the same plane of airfoil cross-section.

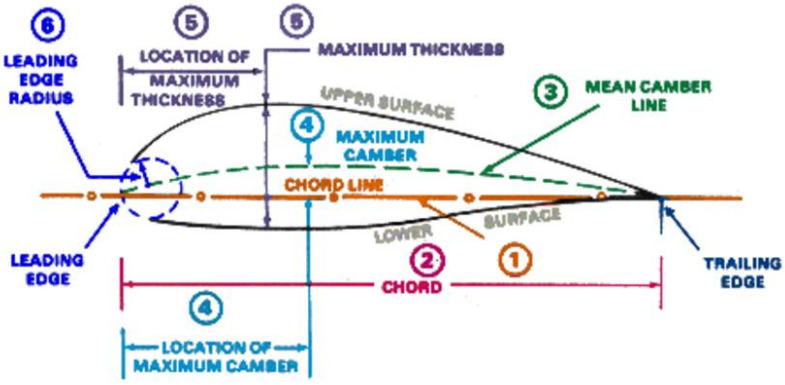

Figure 3.3 Airfoil Terminology[58]

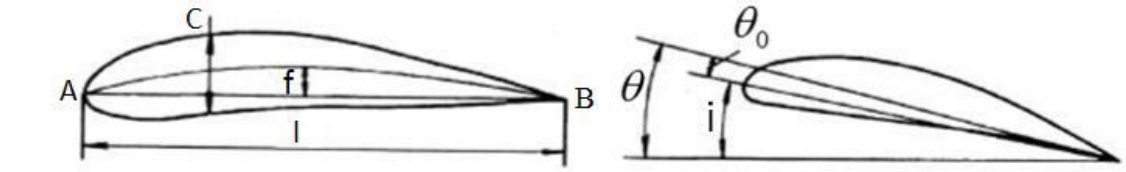

Figure 3.4 Cross-sectional view of airfoil

Point B -- Trailing edge. the trailing edge is relatively thin. Point A -- Leading edge. The leading edge is relatively thick. L -- airfoil chord, the maximum length from points A to B, and chord is the width of the blade. C--maximum thickness, the Maximum thickness in the normal direction of airfoil chord : $\bar{C}$ -- relative thickness of airfoil, $\bar{C} = \frac{C}{l}$, usually 10% -15%. Airfoil central line -- the

circle center connection line of various tangency circle of upper and lower surfaces from the leading edge to trailing edge. f --maximum bending of airfoil central line. i--angle of attack, is the angle between the direction of flow and the chord line; θ_0 -- zero lift angle, which is the angle between the chord line and the zero lift line; θ -- lift angle, the angle between the direction of flow and zero lift line.

$$i = \theta + \theta_0 \tag{3.3}$$

Here, θ_0 is negative, θ and i are positive. Torsion angle-the angle between the blade chord line and the plane of rotation of the wind wheel.

3.2.3 Mechanical Analysis during Blades Rotation

The forces acting on the blade scan be simplified to three: aerodynamic, centrifugal force and gravity.

Aerodynamic design includes: rotor diameter, number of blades, each cross-section blade chord length, thickness, twist angle distribution and airfoil cross-section. To determine each blade lift, resistance, absorption, tip losses at a certain wind speed. These aerodynamic forces can be decomposed into normal and tangential two kinds of forces along the blade: the force F on the airfoil are related to the relative velocity direction, and can be expressed as

$$F = \frac{1}{2}\rho C_r S v^2 \tag{3.4}$$

Where S--wings pan area, equal to chord length l multiplied by the wing span length b;

C_r --total aero-dynamic coefficients.

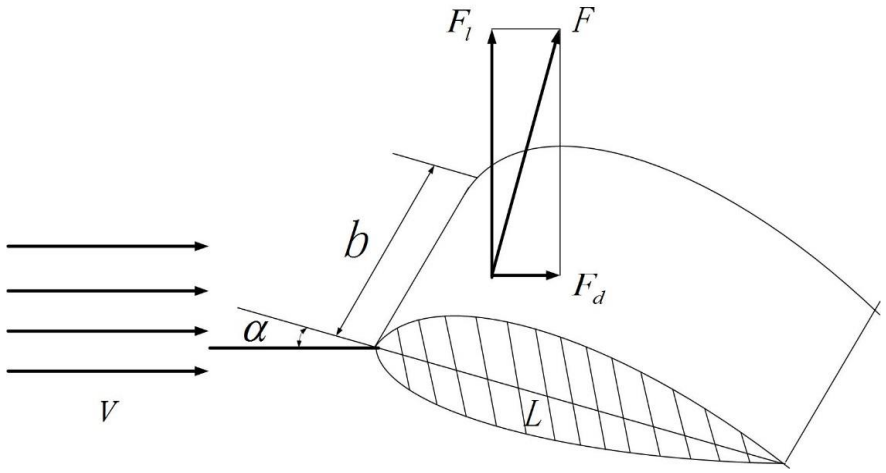

Figure 3.5 Mechanical Analysis of Rotating blades

This force can be divided into two parts: the component F_d parallel to velocity v, known as resistance; and vertical components F_1 of velocity v, called the lift. F_d and F_1 can be expressed as

$$F_d = \frac{1}{2}\rho C_d(\alpha_A)Sv^2 \tag{3.5}$$

$$F_1 = \frac{1}{2}\rho C_l(\alpha_A)Sv^2 \tag{3.6}$$

Where, C_d, C_l are the drag coefficient and lift coefficient. ρ is the air density, v is stream density. Lift-drag ratio is $\varepsilon(\alpha_A) = \frac{F_l}{F_d} = \frac{C_l(\alpha_A)}{C_d(\alpha_A)}$ the quality of airfoil is measured by maximum lift to drag ratio $\varepsilon_{\max}$, lift to drag ratio of high qualityairfoilmayreach60 or more, and even flat lift to drag ratio can also reach 10.

Because the two components are vertical and therefore it has the following relationship:

$$\begin{cases} F_d^2 + F_l^2 = F^2 \\ C_d^2 + C_l^2 = C_r^2 \end{cases} \tag{3.7}$$

If using M expressed the torque caused by F at the leading edge point, can obtain the pitch moment coefficient C_M .

$$M = \frac{1}{2}\rho C_M S l v^2 \tag{3.8}$$

Therefore, force on the aero-dynamic airfoil can be expressed as lift, drag and pitch moment.

It should be noted that, in different cross-sectional shape, the airfoil lift and drag characteristics vary widely, affecting the airfoil lift and drag characteristics factors are: camber, thickness, leading edge, surface roughness, limited wingspan.

When the blade results in a stall in the operation, there is a noise increase caused by blade vibration and unstable phenomenon. Therefore, in selecting the C_l value, we cannot set the stall point as the design point. For horizontal axis wind turbine, in order to make the blade still work well slightly to the right design point, the C_l value, the maximum does not exceed 0.8 to 0.9.

Centrifugal force

$$p(r) = \int_r^R \delta Q^2 f r_l dr_l \tag{3.9}$$

Gravity load

$$q_g = -pfg\sin W \tag{3.10}$$

Where p, f conversion density and area of the blades. W is blade rotation azimuth. q is the acceleration of gravity. Q is leaf sectional diameter. δ is speed.

Blades under these three major forces, there are two load: cyclic loading, non-cyclical load. When the periodic interference force is applied, forced vibration may occur indifferent directions. Its possible vibration types are:

Tangential bending vibration—vibration along the minimal inertia of blade sectional in the vertical direction.

Axial bending vibration—vibration along the minimal inertia of blade sectional in the vertical direction.

Torsional vibration—vibration along the blade height direction and through the center axis of gravity of the cross section.

Composite vibration—combination of bending and torsional vibrations. Self-excited vibration may also occur.

3.2.4 Wind Turbine Blade Design and Momentum (BEM) Theory

Relationship between wind turbine blades momentum and wind power

Because of the non-uniform force of blade can easily cause vibration, it is assumed that the forces on a blade element can be calculated by means of two-dimensional aerofoil characteristics using an angle of attack determined from the incident resultant velocity in the cross-sectional plane of the element; In a radial position on the blade, given values of a and a' determined the aerofoil characteristic coefficient C_d and C_l vary with the angle of attack. Consider a turbine with N blades, tip radius of R, chord of c, pitch angle of β (measured between the aerofoil zero lift line and the plane of the disc), blade speed of Ω, and the wind speed be U_∞, combining the tangential velocity Ωr and tangential velocity of the wake a $'\Omega$ r gets the net tangential flow velocity (1 +a $')\Omega$r. The resultant relative velocity at the blade with the blade chord line at radius r is shown in **Figure 3.6**.

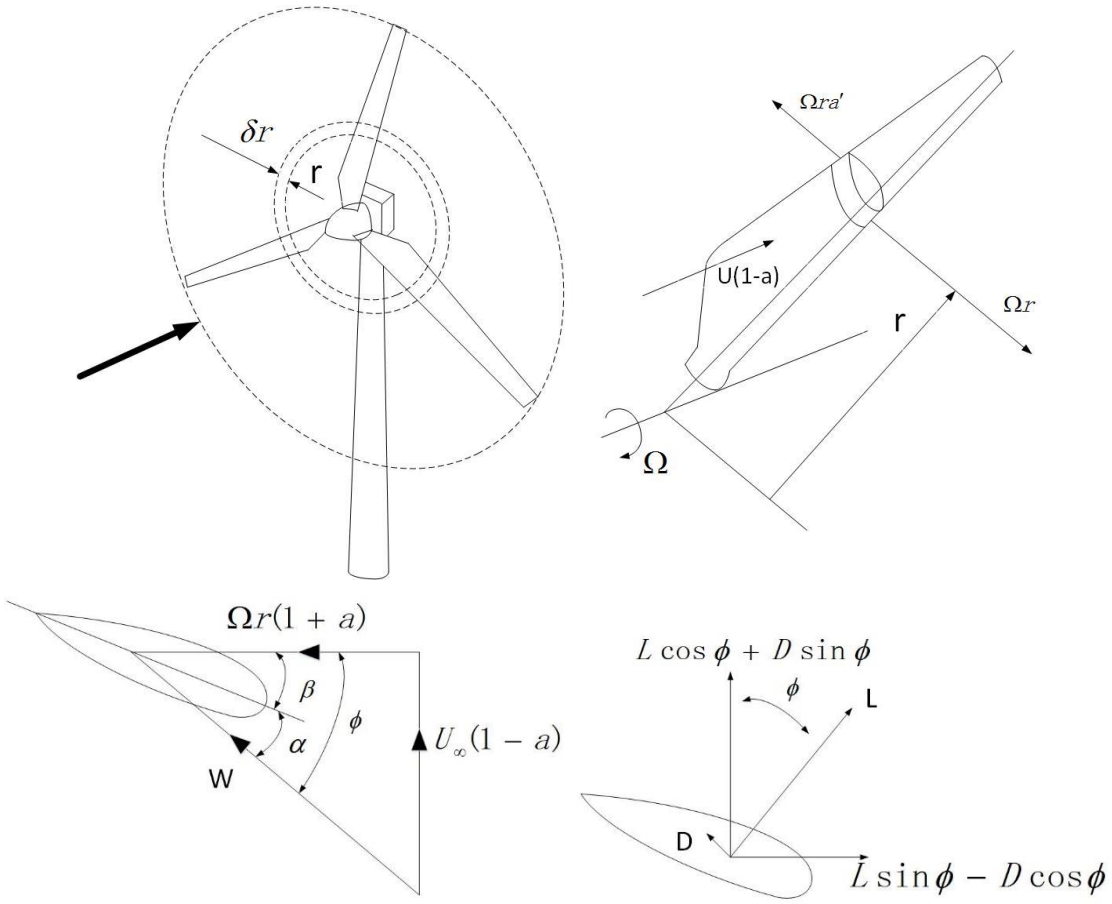

Figure 3.6 Speed and force of rotating blades and blade element

$$W = \sqrt{U_\infty^2(1-a)^2 + \Omega^2 r^2(1+a')^2} \tag{3.11}$$

Which acts at an angle φ to the plane of rotation, thus,

$$\sin\varphi = \frac{U_\infty(1-a)}{W} \tag{3.12}$$

$$\cos\varphi = \frac{\Omega r(1+a')}{W} \tag{3.13}$$

The angle of attack α is

$$\alpha = \varphi - \beta \tag{3.14}$$

The lift force on a span-wise length δr (vertical to the direction of W) is,

$$\delta L = \frac{1}{2}\rho W^2 c C_L \delta r \tag{3.15}$$

The drag force (parallel to the W) is,

$$\delta D = \frac{1}{2}\rho W^2 c C_d r \delta r \tag{3.16}$$

Momentum (BEM) theory [59]

The basic BEM assumes that: the force on the blade element is responsible for the change of momentum of the air which pass through the annulus swept. It is assumed that there is no interaction of the air flows through contiguous annuli in radial direction.

N blade elements axial force can be expressed as follows

$$\delta L \cos\varphi + \delta D \sin\varphi = \frac{1}{2}\rho W^2 N c (C_L \cos\varphi + C_d \sin\varphi)\delta r \tag{3.17}$$

The axial momentum change rate of the air pass thorough the swept annulus is

$$\rho U_\infty (1-a) 2\pi r \delta r 2 a U_\infty = 4\pi\rho U_\infty^2 a(1-a) r \delta r \tag{3.18}$$

The drop in wake pressure caused by wake rotation is equal to the increase in dynamic head, which is

$$\frac{1}{2}\rho(2a'\Omega r)^2 \tag{3.19}$$

The additional axial force on the annulus is

$$\frac{1}{2}\rho(2a'\Omega r)^2 2\pi r \delta r \tag{3.20}$$

Thus,

$$\frac{1}{2}\rho W^2 N c (C_l \cos\varphi + C_d \sin\varphi)\delta r = 4\pi\rho[U_\infty^2 a(1-a) + (a'\Omega r)^2] r \delta r \tag{3.21}$$

Thereby

$$\frac{W^2}{U_\infty^2} N \frac{c}{R}(C_l \sin\varphi - C_d \cos\varphi) = 8\pi(a(1-a) + (a'\lambda\mu)^2)\mu \tag{3.22}$$

Element rotor torque on the axial driven by aerodynamic is expressed as follows

$$(\delta L \sin\varphi - \delta D \cos\varphi)r = \frac{1}{2}\rho W^2 Nc(C_l \sin\varphi - C_d \cos\varphi)r\delta r \tag{3.23}$$

The axial angular momentum change rate of the air pass thorough the swept annulus is

$$\rho U_\infty (1-a)2\pi r\delta r 2aU_\infty = 4\pi\rho U_\infty^2(\Omega r)a'(1-a)r^2\delta r \tag{3.24}$$

Equaling the two moments

$$\frac{1}{2}\rho W^2 Nc(C_L \sin\varphi - C_d \cos\varphi)r\delta r = 4\pi\rho U_\infty(\Omega r)a'(1-a)r^2\delta r \tag{3.25}$$

Simplify

$$\frac{W^2}{U_\infty^2} N \frac{c}{R}(C_l \sin\varphi - C_d \cos\varphi) = 8\pi\lambda\mu^2 a'(1-a) \tag{3.26}$$

Where the parameter $\mu = r / R$

Simplify,

$$C_l \cos\varphi + C_d \sin\varphi = C_x \tag{3.27}$$

$$C_l \sin\varphi + C_d \cos\varphi = C_y \tag{3.28}$$

Calculation of torque and power produced by wind turbines need to determine flow induction factors, the factor can be induced by solving Equations (3.22) and (3.25). Because the two-dimensional airfoil characteristics are nonlinear function of the angle of attack, the solution is obtained through repeated iterations. To determine the performance characteristics of wind turbine blade, such as power coefficient varying in a wide range tip speed ratio, need iteratively

solved process. First, assuming a and a' equal to zero, we get φ, C_p and C_d, and then find a new flow factor by the equation (3.22) and (3.25). Iterative process need to keep repeating until it reaches the convergence point.

$$\frac{a}{1-a}=\frac{\sigma_r}{4\sin\varphi^2}[(C_x)-\frac{\sigma_r}{4\sin^2\varphi}C_y^2] \tag{3.29}$$

$$\frac{a}{1+a'}=\frac{\sigma_r C_y}{4\sin\varphi\cos\varphi} \tag{3.30}$$

Blade solidity σ is defined as total blade area divided by the rotor disc area and is a primary parameter in determining rotor performance. Chord solidity σ_r is defined as the total blade chord length at a given radius divided by the circumferential length at that radius.

$$\sigma_r=\frac{N}{2\pi}\frac{c}{r}=\frac{N}{2\pi\mu}\frac{c}{R} \tag{3.31}$$

The last point about the BEM theory is: only the blade ring has a uniform amount, when a is uniform, this theory applies.

3.3 Common Damage of Blade in Operation and Maintenance

1. Blade vibration

Blade vibration include: vibration in vertical direction of blade plane, vibration parallel to the direction of blade plane, the vibration direction parallel leaf strings, in which, the vibration direction parallel leaf strings hazards largest and most obvious, because of the vibration frequency of the vibration frequency and the impeller is similar, under certain conditions, may produce resonance effects, such as greater resonance amplitude, also higher damage for the impeller.

2. Blade icing

Figure 3.7 Blade icing[60]

Effect of ice on wind turbine blades is enormous. It not only changes the blade aerodynamic shape, and reduces efficiency, but also causes rotational imbalance even to the point that it cannot not run. Moisture in the air will freeze at temperatures below 0 ℃. Ice formed and quantity is affected by weather conditions, equipment size and status (moving or still). Generally icy environment occurs in two ways: one is the temperature at 0 ℃, when small droplets in the air hit the low temperature surface of the device, it will freeze on the surface of the device: the other is when the temperature is far below 0 ℃.

3. Blade crack

Figure 3.8 Blade crack[61]

Crack extension causes wind turbines blade fracture is a very serious situation of harm. In general, the main reason of wind turbine blades crack is local stress concentrated on the blade. Long-term, low-load, overload or running in vibration area also make blades crack or exacerbating the situation in the alternating stress. Wind turbine blade crack should be checked timely for processing defects, helping to eliminate accidents.

4. Blades pitting

Pitting corrosion means that on the local surface there emerges corrosion holes which develop the deep pitting phenomenon. When wind turbine blades get pitting, it will seriously damage the blades, and even blade fracture in running. So the blade pitting failure analysis and diagnosis is very important.

5. Blades worn

In the wind turbine operation, due to the high-speed of dust, sand in the air collision to blades, often produce blades wear fault through wear. It will cause wind turbine rotor run balance, blade fracture, etc., so the blade wear fault analysis and diagnosis is very important.

For blade vibration and wear, it can be detected from the radar echo signal. From the spectrum of echo signals, we can directly analyze their fault, but for more complex problems, especially

multiple failures occurring simultaneously, it is difficult to analyze, and we need to use other means of analysis. In next chapter, we would focus on the analysis of these failures from the characteristics of radar echo signal.

Chapter 4 Micro-Doppler Effect in Radar

Micro-Doppler effect was first introduced in coherent laser radar system[62]. Laser radar (Laser detection and ranging, LADAR) system transmits an optical frequency electromagnetic waves to an object and receiving the reflected light wave, through its laser beam amplitude, frequency, phase, and polarization modulation to measure the distance of the object, speed and other properties.

Coherent laser radar retains phase information of scattered light and a reference laser from the local oscillator, with great sensitivity and has the ability to measure the speed of the object from the rate of change in phase.

Micro-Doppler effect caused by the components of the object can be explained from the physics and mathematics. In Physics, the micro-Doppler effect comes from electromagnetic scattering field theory. Before analyzing radar objects with micro-movement, introduce the basic principles of radar scattering and rigid body motion.

4.1 Micro-Motion

In many cases, an object or any structural of this object may have an oscillation effect, called micro-motion. As a result, except for the main body of the moving object, the object or any structural component of the oscillatory motion of the object can be called micro-movements.

Micromotion induced frequency modulation in radar carrier frequency signal. For purely periodic vibration or rotation movement, the micro-Doppler-shifted produces side bands Doppler shift in center carrier frequency. This modulation comprises harmonic frequency related to the angle of carrier frequency, vibration or the rate of rotation, the vibration direction and the direction of the incident wave. Frequency modulation determines the kinematic properties of the object.

Micro-Doppler effect is sensitive to the signal band. For work in the microwave band radar system, if the multiplication value of target oscillation rate and the oscillation displacement is high enough, the micro-Doppler effect can be observed. Generated by the rotation of the micro-Doppler shift, for example, the rotation of the rotor blades, as the longer arm and higher tip speed, it can be detected Doppler shift.

4.1.1 Rigid-Body Motion

An object can be rigid or non-rigid. Rigid body is a finite size, but no deformation of the solid (in any sport, the distance between the two particles does not change). This is an idealized model but it effectively simplifies the simulation and analysis.

Quality of Rigid M is all particles quality of M, $\mathrm{M}=\sum_{k} m_k$ where m_k is the quality of the k th particle. Rigid body motion is usually a combination of translation (all the particles moving in parallel) and rotation(all particles of the object circular motion about an axis) [63-65].

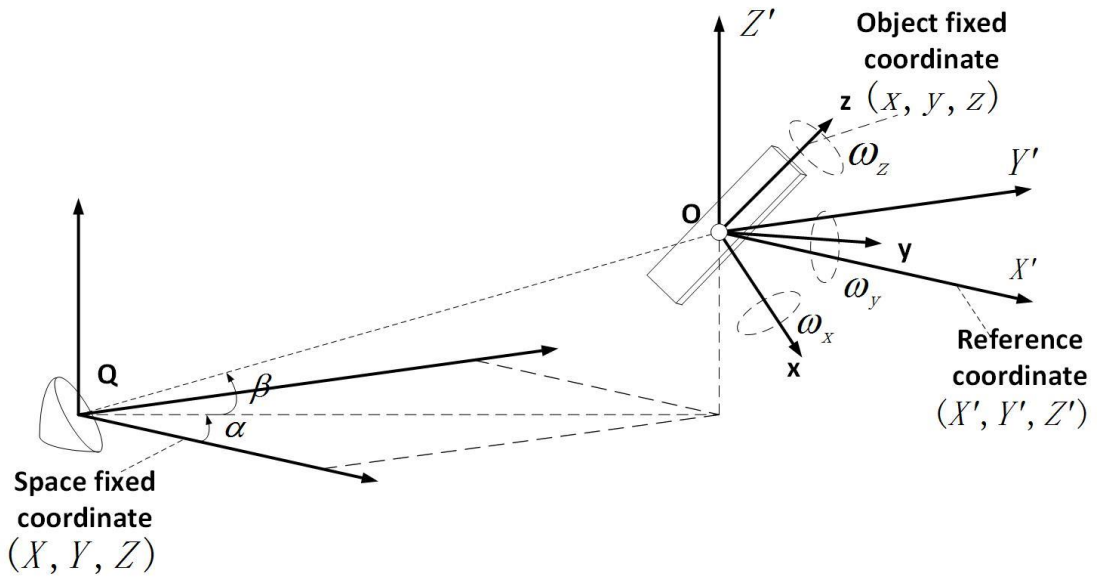

Figure 4.1 Three dimensional coordinates

To describe rigid body motion, usually using three coordinates, shown in **Figure 4.1**: spatially fixed coordinate (X, Y, Z), local fixed coordinate system (x, y, z) and reference coordinate $\left(X', Y', Z'\right)$. R is the distance from the origin of space fixed coordinate system to the origin of the object fixed coordinate. Set the object origin as the center of mass of the object (O). Then, the direction of the object fixed coordinate related to spatially fixed coordinate is given by three independent angles. Therefore, the rigid body is a mathematical system with six degrees of freedom. r is any particle P located in a fixed objects coordinate, then its position in space fixed coordinate is given by r + R. The speed of particle P_i

$$\mathrm{v} = \frac{d}{dt}\left(R + r\right) = V + \Omega \times \tag{4.1}$$

Where, V is the translational velocity of the center of mass of a rigid body, Ω is the angular velocity of the rotation object. Ω direction is along the rotation axis. Therefore, the rigid body motion includes translational movement and object rotation and (or) vibration.

In order to indicate the direction of the object, Euler angles, rotation matrices and quaternions are the most commonly used method.

4.1.2 Euler Angles

Construction of limited rotation in three dimensions space can be followed by three relative rotation, the three rotation angle referred to Euler angles.

Leonhard Euler use Euler angles to describe the rigid body in three-dimensional Euclidean space orientation. For any reference coordinate, a rigid body orientation, in accordance with the order from the reference coordinate, do the three Euler angles rotation. Therefore, the orientation of rigid body orientation can be used three rotation matrixes to determine. In other words, any rotation matrix of rotating rigid body is composed of three basic rotation matrix.

Euler angles is a description of rotation.

For Euler angles (α, β, r) in coordinate E

1. Composite three matrix---Rotate angle α around x-axis under coordinate E, rotating angle β about y-axis under coordinate E, rotating angle r around z-axis under coordinate E.

2. Composite three matrix---rotate angle α around x-axis under coordinate E, rotating angle β about y-axis under the new coordinate E' (after the coordinate rotating angle α around the x axis under coordinate E), rotating angle r around the z axis under coordinates E'' (after the coordinate rotating angle β around the y-axis under coordinate E').

The two rotation method is not equivalent.

When we talked about Euler angles (α, β, r) under coordinates E, this sentence is ambiguous, we must define the rotation order, because the rotation order will affect the result of the rotation.

If it is assumed that the order of rotation is first about the x axis, next y axis, then z-axis, x-y-z, then the Euler angles corresponding to the rotation matrix is that in 2 described above.

Assuming the rotation order is first around z-axis, next y-axis then the x-axis, z-y-x, then the Euler angles of rotation matrix corresponding to 1 above indicated rotation matrix. It looks like change the order of 2, that is rotate angle r about z-axis under coordinate E, rotating angle β around y-axis under coordinate E'(after the coordinate rotates angler around z-axis under the coordinate E), rotating angle α around x-axis under the coordinates E''(after the coordinate rotating angle β around y-axis under coordinate E').

We define Euler angles (ϕ, θ, ψ), ϕ is defined as the counter-clockwise rotation around the z-axis, θ defined as counterclockwise rotation around the y-axis, ψ defined as the counterclockwise rotation around the x axis. Euler angles are often used to represent three successive rotated at a given rotational sequence. The first step in a rotation sequence is that rotating coordinate(x, y, z) rotates to the new coordinate (x_1, y_1, z_1). In step 2, coordinate (x_1, y_1, z_1) rotated to new

coordinate（x_2, y_2, z_2）,the third transform the coordinates change to the final coordinates（x_3, y_3, z_3）,as described in **Figure 4.2.**

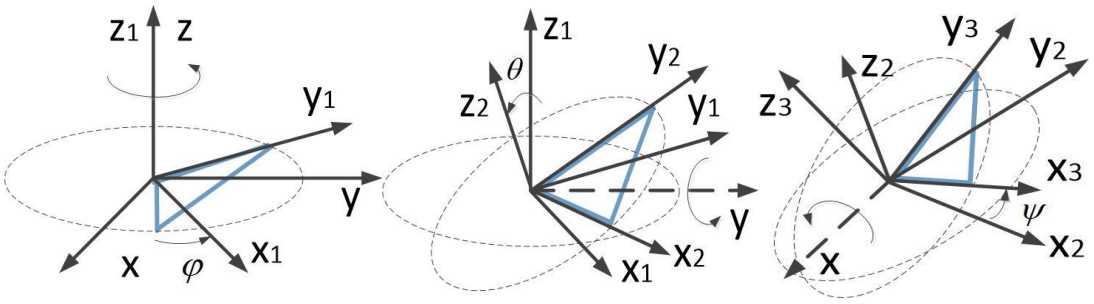

Figure 4.2 Euler angles of three consecutive rotation

Another common rotation sequence in classical mechanics is called x convention. It follows the sequence z-x-z, first rotate an angle about the z-axis, then rotate an angle about the x-axis, third rotate an angle around z-axis.

For x-y-z sequences, rotation is followed by x-y-z (ψ, θ,ϕ) sequence. Step 1, rotate around the x-axis, $\mathrm{x} = \begin{bmatrix} 1 & 0 & 0 \end{bmatrix}^T$, rotating followed by rotation angle ψ:

$$R_x = \begin{bmatrix} 1 & 0 & 0 \\ 0 & \cos\psi & \sin\psi \\ 0 & -\sin\psi & \cos\psi \end{bmatrix} \tag{4.2}$$

Step 2, rotate around the new y-axis, $y_1 = \begin{bmatrix} 0 & \cos\psi & \sin\psi \end{bmatrix}^T$, rotating followed by rotation angle θ:

$$R_Y = \begin{bmatrix} \cos\theta & 0 & -\sin\theta \\ 0 & 1 & 0 \\ 0 & -\sin\psi & \cos\psi \end{bmatrix} \tag{4.3}$$

Step 3, rotate around the new z-axis, $z_2 = \begin{bmatrix} -\sin\theta & \cos\theta\sin\psi & \cos\theta\cos\psi \end{bmatrix}^T$, rotating followed by rotation angle ϕ:

$$R_Z = \begin{bmatrix} \cos\phi & \sin\phi & 0 \\ -\sin\phi & \cos\phi & 0 \\ 0 & 0 & 1 \end{bmatrix} \tag{4.4}$$

Thus, the rotation matrix x-y-z sequence is

$$R_{X-Y-Z} = R_Z \cdot (R_Y \cdot R_X) = \begin{bmatrix} r_{11} & r_{12} & r_{13} \\ r_{21} & r_{22} & r_{23} \\ r_{31} & r_{32} & r_{33} \end{bmatrix} \tag{4.5}$$

Where, rotation matrix components are

$$\begin{cases} r_{11} = \cos\theta\cos\phi \\ r_{12} = \sin\psi\sin\theta\cos\phi + \cos\psi\sin\phi \\ r_{13} = -\cos\psi\sin\theta\cos\phi + \sin\psi\sin\phi \end{cases} \tag{4.6}$$

$$\begin{cases} r_{21} = -\cos\theta\sin\phi \\ r_{22} = -\sin\psi\sin\theta\sin\phi + \cos\psi\cos\phi \\ r_{23} = \cos\psi\sin\theta\sin\phi + \sin\psi\cos\phi \end{cases} \tag{4.7}$$

$$\begin{cases} r_{31} = \sin\theta \\ r_{32} = -\sin\psi\cos\theta \\ r_{33} = \cos\psi\cos\theta \end{cases} \tag{4.8}$$

According to component of rotation matrix, if $\cos\theta \neq 0$ or $|r_{11}| + |r_{12}| \neq 0$, the three rotation angle (ψ, θ, ϕ) can be determined as follows:

$$\begin{cases} \psi = \arctan(-r_{32} / r_{33}) \\ \theta = \arcsin(r_{31}) \\ \phi = \arctan(-r_{21} / r_{11}) \end{cases} \tag{4.9}$$

If $\theta = \pi/2$ or $-\pi/2$, $\cos\theta = 0$, will occur gimbal lock phenomenon[66-67].

Although Euler angles rotation matrix process are convenient and easier to understand, but it have a problem called gimbal lock. When the two axes located in a straight line, the gimbal lock will occur. It causes one-dimensional degree of freedom lost. For example, in x-y-z sequence, when the

angle of rotation $\theta = \pi/2$ around the y-axis, y-axis, x-axis and z-axis folding each other, and therefore a degree of freedom is lost. Recalling the Equation (4.5)- Equation (4.8), when the angle of rotation $\theta = \pi/2$ around the y-axis, rotation matrix becomes

$$R_{X-Y-Z}(\psi, \theta = \frac{\pi}{2}, \phi) = \begin{bmatrix} 0 & 0 & -1 \\ \sin\psi\cos\phi - \cos\psi\sin\phi & \sin\psi\sin\phi + \cos\psi\cos\phi & 0 \\ \cos\psi\cos\phi + \cos\psi\cos\phi & \cos\psi\sin\phi - \sin\psi\cos\phi & 0 \end{bmatrix}$$

(4.10)

If $\psi = 0$, the rotating matrix is

$$R_{X-Y-Z}(\psi = 0, \theta = \frac{\pi}{2}, \phi) = \begin{bmatrix} 0 & 0 & -1 \\ -\sin\phi & \cos\phi & 0 \\ \cos\phi & \sin\phi & 0 \end{bmatrix} \quad (4.11)$$

When $\phi = 0$, $\psi = -\psi$, rotating matrix is

$$R_{X-Y-Z}(\psi = -\psi, \theta = \frac{\pi}{2}, \phi = 0) = \begin{bmatrix} 0 & 0 & -1 \\ -\sin\phi & \cos\phi & 0 \\ \cos\phi & \sin\phi & 0 \end{bmatrix} \quad (4.12)$$

Therefore, the 3×3 rotation matrix $R_{X-Y-Z}(0, \frac{\pi}{2}, \phi)$ is equal to the value of the rotation matrix $R_{X-Y-Z}(-\psi, \frac{\pi}{2}, 0)$, so a degree of freedom is lost. In this case, there are only two degrees of freedom. Thus, gimbal lock results an undesired and restricted movement.

4.2 Electromagnetic Scattering from Moving Object

Scattered field and RCS characteristics of the object are often calculated under the assumption that the object is stationary. However, in most practical cases, the member objector objects are rarely static, and there may be movement, such as translation, rotation or oscillation.

Theoretical analysis shows that the moving object modulate scattering electromagnetic wave phase function [68-70]. If an object linearly oscillate periodically, modulation cause sidebands in Doppler frequency of translation.

For translation object, far field of the object can be derived as follows [69]:

$$E_T(r') = \exp\{jkr_0 \cdot (u_k - u_r)\}E(r) \tag{4.13}$$

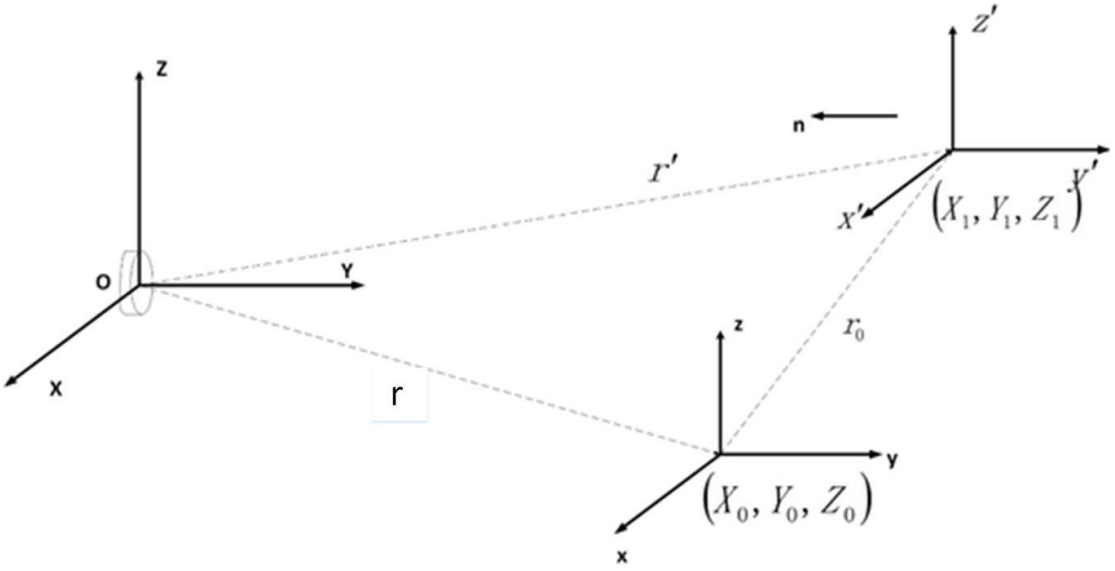

Figure 4.3 Geometry of translation object in the far electromagnetic fields

Where, $k = 2\pi / \lambda$ is the wave number, u_k is a unit vector of the incident wave, u_r is the unit vector of observe direction, $E(r)$ is far field before moving, $r = (X_0, Y_0, Z_0)$ is the starting coordinates in space fixed coordinate, $r' = (X_1, Y_1, Z_1)$ is translated objects to space fixed coordinate, and $r' = r + r_0$, r_0 is the translation vector, as shown in **Figure 4.3**.

The only difference between the before translation and after translation is phase item $\exp\{jkr_0 \cdot (u_k - u_r)\}$. If the translation is a function of time $r_0 = r_0(t) = r_0(t)u_T$, here u_T is a translation unit vector, the phase function becomes

$$\exp\{j\Phi(t)\} = \exp\{jkr_0(t)u_T \cdot (u_k - u_r)\}E(r) \tag{4.14}$$

For back scatter, the observation direction opposite to the direction of the incident wave. $u_k = -u_r$, and

$$\exp\{j\Phi(t)\} = \exp\{j2kr_0(t)u_T \cdot u_k\} \tag{4.15}$$

If the translation direction is perpendicular to the incident direction, $u_T \cdot u_k$, $\exp\{\Phi(t)\} = 1$.

For a vibrating object, assuming that $r_0(t) = A\cos\Omega t$, the phase factor becomes a function of time with angular frequency of Ω:

$$\exp\{j\Phi(t)\} = \exp\{j2kA\cos\Omega t u_T \cdot u_k\} \tag{4.16}$$

In general, when the radar transmits an electromagnetic waves of carrier frequency f_0, radar received signal can be expressed as

$$s(t) = \exp\{jkr_0(t)(u_k - u_r) - j2\pi f_0 t\}|E(r)| \tag{4.17}$$

Where, phase factor $\exp\{jkr_0(t)(u_k - u_r)\}$ is defined as modulated by time varying operation of the micro-Doppler effect.

4.3 Micro-Doppler Calculation

4.3.1 Basic math of micro-Doppler effect

For simplicity, radar target is represented as a set of points scattering, the scattering of these points is the main reflection point on the target. Point scattering model simplifies the analysis, while retaining the micro-Doppler features. In a simplified model, the scattering are considered to be perfect reflecting mirror, reflecting whole energy.

As shown in **Figure 4.4**, radar is stationary and radar is located at the origin point Q of space fixed coordinate (X, Y, Z).Target is described by the local coordinate(x, y, z), and there are translation and rotation relating to radar coordinate. To observe target rotating, a reference coordinate

(X', Y', Z') is introduced, it shares the same origin point in the local coordinate, therefore reference coordinate has the same translation as target, but not rotating relative to the radar coordinates. Reference coordinate origin point O is assumed to be located at a distance R_0 from the radar.

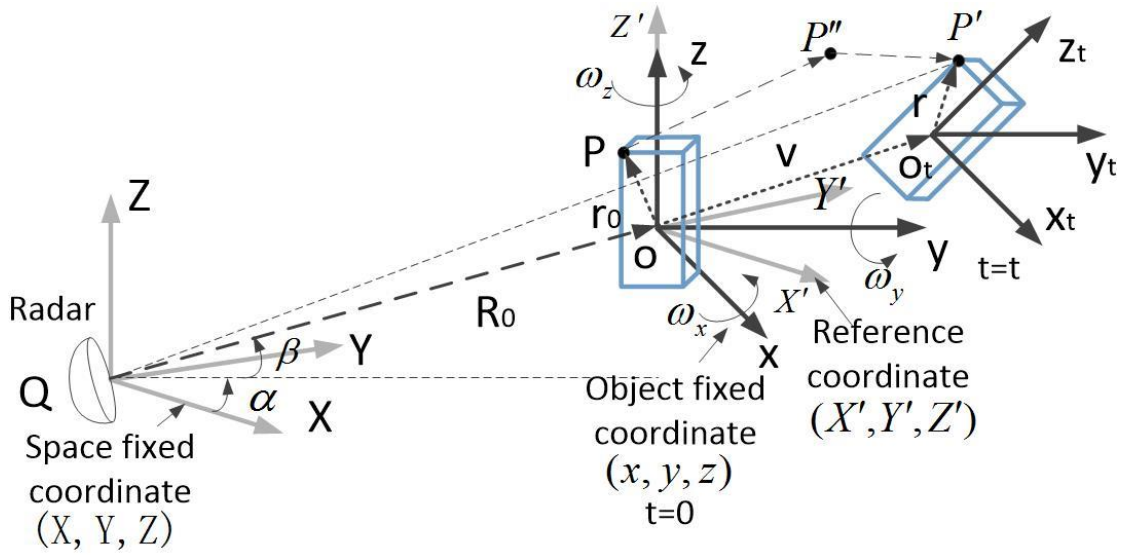

Figure 4.4 The geometric relationship between the blades rotating and translation

4.3.2 Micro Doppler caused by micro -moving target

Assuming that the target has the translational velocity v relative to radar and angular rotation speed ω, can be expressed as $\omega = (\omega_x, \omega_y, \omega_z)^T$ in the local coordinate or expressed as $\omega = (\omega_X, \omega_Y, \omega_Z)^T$ in the reference coordinate. Thus, the point in time t scattering will move to P'. This movement involves two steps: (1) as shown in **Figure 4.4**, with speed v from P shifted to P'', that is $OO_t = vt$; (2) with the rotational angular velocity ω from P'' to P'. If we observe this motion in the reference coordinate, the point P is positioned at $r_0 = (X_0, Y_0, Z_0)^T$, and the rotation described by the rotation matrix R_t. Then, the position P' at time t will be

$$r = O_t P' = R_t O_t P'' = R_t r_0 \tag{4.18}$$

$$QP' = QO + OO_t + O_t P' = R_0 + vt + R_t r_0 \tag{4.19}$$

The distance from the radar Q to the point of scattering vector P' can be derived as follows:

$$QP' = QO + OO_t + O_t P' = R_0 + vt + R_t r_0 \tag{4.20}$$

Scalar distance is

$$r(t) = \left\| R_0 + vt + R_t r_0 \right\| \tag{4.21}$$

Where, $\left\| \cdot \right\|$ represents Euclidean norm.

If the radar transmits a carrier f sine wave from the scattering of point P base band signal is a function of:

$$s(t) = p(x, y, z) \exp\{ j2\pi f \frac{2r(t)}{c} \} = p(x, y, z) \exp\{ j\Phi[r(t)] \} \tag{4.22}$$

Where, $\rho(x, y, z)$ is scattering reflectance function of point P' in the local coordinate. c is electromagnetic wave propagation velocity, the phase of the baseband signal is

$$\Phi(r) = 2\pi f \frac{2r(t)}{c} \tag{4.23}$$

By the time derivative of the phase, caused by the movement target Doppler shift can be derived:

$$\begin{aligned} f_D &= \frac{1}{2\pi} \frac{d\Phi(t)}{dt} = \frac{2f}{c} \frac{d}{dt} r(t) \\ &= \frac{2f}{c} \frac{1}{2r(t)} \frac{d}{dt} [(R_0 + vt + R_t r_0)^T (R_0 + vt + R_t r_0)] \\ &= \frac{2f}{c} [v + \frac{d}{dt} (R_t r_0)]^T n \end{aligned} \tag{4.24}$$

Where, $n = \dfrac{R_0 + vt + R_t r_0}{\left\| R_0 + vt + R_t r_0 \right\|}$ is the unit vector of QP'.

We can now return to rotation matrix in Equation(4.24). In the reference coordinate, the angular rotation velocity vector can be describe as $\omega = (\omega_X, \omega_Y, \omega_Z)^T$, the target will be along the unit vector $\omega' = \frac{\omega}{\|\omega\|}$ rotating with a scalar angular velocity $\Omega = \|\omega\|$. Assuming a high pulse repetition rate and a relatively low angular velocity, each time interval of the rotary motion can be considered infinitely small

$$R_t = \exp\{\hat{\omega}t\} \tag{4.25}$$

Where $\hat{\omega}$ is the Skew symmetric matrix associated with ω. Thus, Doppler shift in Equation (4.24) becomes

$$\begin{aligned} f_D &= \frac{2f}{c}\left[v + \frac{d}{dt}(e^{\hat{\omega}t} r_0)\right]^T n = \frac{2f}{c}(v + \hat{\omega} e^{\hat{\omega}t} r_0)^T n \\ &= \frac{2f}{c}(v + \hat{\omega} r)^T n = \frac{2f}{c}(v + \omega \times r)^T n \end{aligned} \tag{4.26}$$

If $\|R_0\| >> \|vt + R_t r\|$, n can be approximated $n = \frac{R_0}{\|R_0\|}$, which is the direction of the sight of the radar. Doppler shift is then approximated

$$f_D = \frac{2f}{c}[v + \omega \times r] \cdot n \tag{4.27}$$

Where, the first term is due to the translation of the Doppler shift.

$$f_{Trans} = \frac{2f}{c} v \cdot n \tag{4.28}$$

The second term is due to the rotation of the Doppler shift.

$$f_{mD} = \frac{2f}{c}[\omega \times r] \cdot n \tag{4.29}$$

For time varying rotation, angular rotation speed is a function of time, and can be expressed as a polynomial function

$$\Omega(t) = \Omega_0 + \Omega_1 t + \Omega_2 t^2 + \ldots \tag{4.30}$$

If not use more than quadratic term items, the micro-Doppler shift can be expressed as

$$f_{mD} = \frac{2f}{c}[\Omega(t) \times r] \cdot n = \frac{2f}{c}[\Omega_0 \cdot (r \times n) + \Omega_1 \cdot (r \times n)t + \Omega_2 (r \times n)t^2] \tag{4.31}$$

The equation has been applied vector operations $(a \times b) \cdot c = a \cdot (b \times c)$.

4.3.3 The micro-Doppler shift caused by vibration

As shown in **Figure 4.5**, radar located at the origin spatially fixed coordinate (X, Y, Z), the scattering point P vibrate in the center point o. The center point is also an origin point of the reference coordinate, the reference coordinate is moving R_0 from (X, Y, Z) to the radar position. We also assume that the center point o is stationary relative to the radar. If the point o relative to the radar azimuth and elevation are α and β, then point o is located in the radar coordinate

$$(R_0 \cos\beta \cos\alpha, R_0 \cos\beta \sin\alpha, R_0 \sin\beta) \tag{4.32}$$

So the radar line of sight (LOS) of the unit vector becomes

$$n = [\cos\alpha \cos\beta, \sin\alpha \cos\beta, \sin\beta]^T \tag{4.33}$$

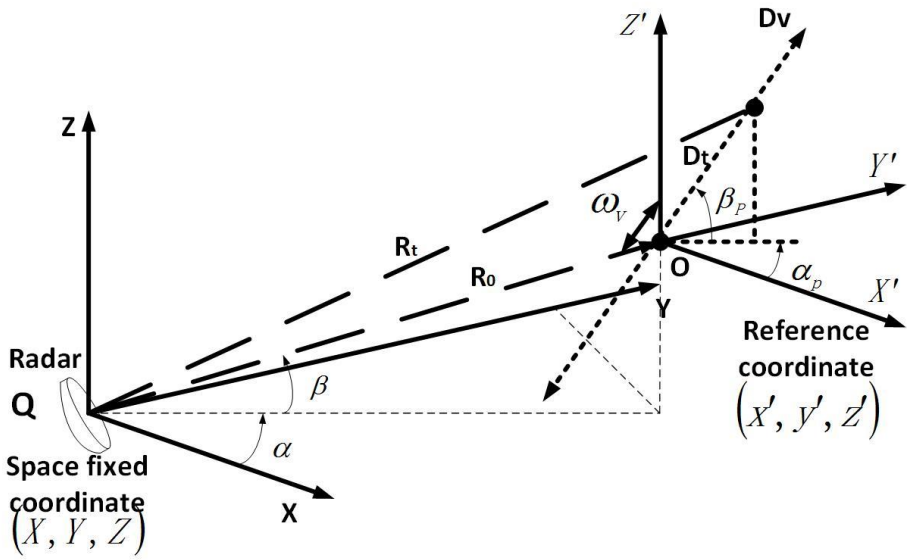

Figure 4.5 micro-Doppler caused by vibration model

Assume that the scattering point P vibrate with frequency f_v and amplitude D_v and the vibration azimuth and elevation are α_p and β_p in the reference coordinate. As shown in **Figure 4.5**, the vector from radar to the scattering point P become $R_t = R_0 + D_t$, the distance from the radar to the scattering point P can be expressed as

$$\begin{aligned} R_t = |R_t| = [&(R_0 \cos\beta\cos\alpha + D_t \cos\beta_P \cos\alpha_P)^2 + \\ &(R_0 \cos\beta\sin\alpha + D_t \cos\beta_P \sin\alpha_P)^2 + \\ &(R_0 \sin\beta + D_t \sin\beta_P)^2]^{1/2} \end{aligned} \tag{4.34}$$

If $R_0 >> D_t$, the distance is approximately

$$\begin{aligned} R_t &= \{R_0^2 + D_t^2 + 2R_0 D_t[\cos\beta\cos\beta_P\cos(\alpha-\alpha_P) + \sin\beta\sin\beta_P]\}^{1/2} \\ &\approx R_0 + D_t[\cos\beta\cos\beta_P\cos(\alpha-\alpha_P) + \sin\beta\sin\beta_P] \end{aligned} \tag{4.35}$$

If the azimuth α of center point O and elevation angle β_p of scattering point P are 0, and $R_0 >> D_t$, then we have

$$R_t = (R_0^2 + D_t^2 + 2R_0 D_t \cos\beta\cos\alpha_P)^{1/2} \cong R_0 + D_t \cos\beta\cos\alpha_P \tag{4.36}$$

Because the angular frequency of the vibration rate is ω_v , andvibration amplitude is ω_v , thus $D_t = D_v \sin \omega_v t$, the scattering point distance become

$$R(t) = R_t = R_0 + D_v \sin \omega_v t \cos \beta \cos \alpha_P \tag{4.37}$$

Radar receiver signal then becomes

$$s_R(t) = \rho \exp\{ j[2\pi f_0 t + 4\pi \frac{R(t)}{\lambda}]\} = \rho \exp\{ j[2\pi f_0 t + \Phi(t)]\} \tag{4.38}$$

Where, ρ is scattering reflectance, f_0 is carrier frequency of the transmitted signal, λ is the wavelength, $\Phi(t) = 4\pi \times R(t) / \lambda$ is the phase function.

Due to vibration, scattering point Pat time t will be

$$\begin{bmatrix} X_1 \\ Y_1 \\ Z_1 \end{bmatrix} = D_v \sin(2\pi f_v t) \begin{bmatrix} \cos \alpha_P \cos \beta_P \\ \sin \alpha_P \cos \beta_P \\ \sin \beta_P \end{bmatrix} + \begin{bmatrix} X_0 \\ Y_0 \\ Z_0 \end{bmatrix} \tag{4.39}$$

Scattering point P due to the speed vibration becomes

$$v = D_v f_v \cos(2\pi f_v t)[\cos \alpha_P \cos \beta_P, \sin \alpha_P \cos \beta_P, \sin \beta_P]^T \tag{4.40}$$

Based on section 4.3.2, the vibration caused by the micro-Doppler shift is

$$\begin{aligned} & f_{mD} = \frac{2f}{v}(v^T \cdot n) = \\ & \frac{2ff_v D_v}{c}[\cos(\alpha - \alpha_P)\cos \beta \cos \beta_P + \sin \beta \sin \beta_P]\cos(2\pi f_v t) \end{aligned} \tag{4.41}$$

If the azimuth α and elevation angles β_P are zero, we have

$$f_{mD} = \frac{2ff_v D_v}{c} \cos \beta \cos \alpha_P \cos(2\pi f_v t) \tag{4.42}$$

When the scatterers in vibration are oriented along the direction of the radar line of sight, or α_P and the elevation angle β are 0, maximum Doppler frequency shift is $2ff_vD_v/c$.

4.3.4 Micro-Doppler shift caused by rotation

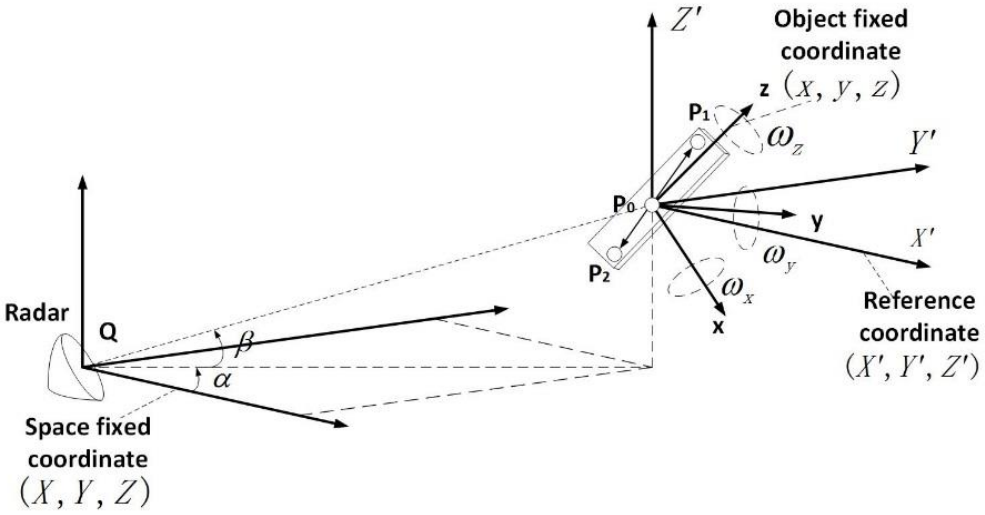

Figure 4.6 Micro-Doppler shift caused by rotation model

The geometric relationship between the radar and the three-dimensional rotation targets are shown in **Figure 4.6**. Space fixed coordinate is (X,Y,Z), and the target local coordinate is (x,y,z), the reference coordinate (X',Y',Z') is parallel to the radar coordinate and locate at the origin point in target local coordinate. Assuming that azimuth α and elevation angles β of target in the radar coordinates.

Due to the rotation target, target at any point in the local coordinate (x,y,z) will be described in the reference coordinate (X',Y',Z'). The new location can be calculated by multiplying the initial rotation matrix (x,y,z order), the initial angle of rotation matrix (ϕ_0,θ_0,ψ_0) in which ϕ_0 is z-axis rotation angle, θ_0 is x-axis rotation angle, and ψ_0 is z-axis rotation angle.

Corresponding initial rotation matrix is defined as

$$R_{Init} = R_Z(\phi_0) \cdot R_X(\theta_0) \cdot R_Z(\psi_0) = \begin{bmatrix} r_{11} & r_{12} & r_{13} \\ r_{21} & r_{22} & r_{23} \\ r_{31} & r_{32} & r_{33} \end{bmatrix} \tag{4.43}$$

Where,

$$\begin{cases} r_{11} = -\sin\phi_0 \cos\theta_0 \sin\psi_0 + \cos\phi_0 \cos\psi_0 \\ r_{21} = -\cos\phi_0 \cos\theta_0 \sin\psi_0 - \sin\phi_0 \cos\psi_0 \\ r_{31} = \sin\theta_0 \sin\psi_0 \end{cases} \tag{4.44}$$

$$\begin{cases} r_{12} = \sin\phi_0 \cos\theta_0 \cos\psi_0 + \cos\phi_0 \sin\psi_0 \\ r_{22} = \cos\phi_0 \cos\theta_0 \cos\psi_0 - \sin\varphi_0 \sin\psi_0 \\ r_{32} = -\sin\theta_0 \cos\psi_0 \end{cases} \tag{4.45}$$

$$\begin{cases} r_{13} = \sin\phi_0 \sin\theta_0 \\ r_{23} = \cos\phi_0 \sin\theta_0 \\ r_{33} = \cos\theta_0 \end{cases} \tag{4.46}$$

Observe in local coordinate, when the target rotates around axis x, y and z in angular velocity $\omega = (\omega_x, \omega_y, \omega_z)^T$, the scattering point P $r_P = (x_P, y_P, z_P)^T$ represented by the local coordinate will be moved to a new location $R_{Init} \cdot r_P$ in the reference coordinate and rotating unit vector becomes

$$\omega = (\omega_x', \omega_y', \omega_z')^T = \frac{R_{Init} \cdot \omega}{\|\omega\|} \tag{4.47}$$

Scalar angular velocity is $\Omega = \|\omega\|$.Thus, according to Rodrigues formula [48], at time t the rotation matrix becomes

$$R_t = I + \hat{\omega}' \sin\Omega t + \hat{\omega}'^2 (1 - \cos\Omega t) \tag{4.48}$$

Where, $\hat{\omega}'$ is the skew-symmetric matrix.

$$\hat{\omega}' = \begin{bmatrix} 0 & -\omega_z' & \omega_y' \\ \omega_z' & 0 & -\omega_x' \\ -\omega_y' & \omega_x' & 0 \end{bmatrix} \tag{4.49}$$

Thus, in the reference coordinate (X', Y', Z'), at time t scattering point P will move to a new location $r = R_t \cdot R_{Init} \cdot r_P$. According to section 4.3.3 of the discussion, micro-Doppler shift caused by rotation approximately.

$$\begin{aligned} f_{mD} &= \frac{2f}{c}[\Omega\omega' \times r]_{radial} = \frac{2f}{c}(\Omega\hat{\omega}' r)^T \cdot n = \frac{2f}{c}[\Omega\hat{\omega}' R_t \cdot R_{Init} \cdot r_P]^T \cdot n \\ &= \frac{2f\Omega}{c}\{[\hat{\omega}'^2 \sin\Omega t - \hat{\omega}'^3 \cos\Omega t + \hat{\omega}'(I + \hat{\omega}'(I + \hat{\omega}'^2)]R_{Init} \cdot r_P\}^T \cdot n \end{aligned} \tag{4.50}$$

If the skew symmetric matrix $\hat{\omega}'$ defined by the unit vector, then $\hat{\omega}'^3 = -\hat{\omega}'$, the micro-Doppler shift rotation caused by rotation is

$$f_{mD} = \frac{2f\Omega}{c}[\hat{\omega}'(\hat{\omega}' \sin\Omega t + I\cos\Omega t)R_{Init} \cdot r_P\}_{radial} \tag{4.51}$$

4.4 Analysis of Micro-Doppler Frequency Shifts

To deal with localized conflicts of the time domain and frequency domain have been proposed "localized in time domain." Typically short-time Fourier analysis method proposed by Gabor in 1946, the basic idea is: Fourier analysis is an essential tool in the frequency domain analysis, in order to achieve localization time domain, before the signal is multiplied by the Fourier transform multiplying a limited time window function, and assume a non-stationary signal analysis window within a short time interval is stationary, moving through the window on the timeline so that the signal is analyzed paragraph by paragraph, so get the signal of a group of "local" spectrum at different times from the "local" differences spectrum, get the time-varying characteristics of the signal.

However, according to the uncertainty principle of Heisenberg, time resolution and frequency resolution cannot be arbitrarily small, their multiplication value is subject to certain restriction. To improve the time resolution we need to reduce the frequency resolution, and vice versa. Once the application window function is selected, the time resolution and frequency resolution is determined, but changing signals of different time periods can only add the same window, so it is not suitable for the requirement of signal frequency changes, so the constant window of short-time Fourier transform, is more suitable for use in quasi-stationary signal analysis applications. In addition, the longer of the signal "local", the harder it is to ensure “local” stability, that are deficiencies of short-time Fourier analysis.

Short-time Fourier transform basic idea is to divide the signal into many small time intervals in order to determine the frequency in that time interval. The spectrum represents that how the spectrum changes over time. When given a very short time width window function $\gamma(t)$ and make the window slide, then the short-time Fourier transform of the signals defined as:

$$\begin{aligned} STFT(t,\omega) &= \int_{-\infty}^{+\infty} s(\tau)\gamma_{t,\omega}^{*}(\tau)d\tau \\ &= \int_{-\infty}^{+\infty} s(\tau)\gamma^{*}(\tau-t)e^{-j\omega\tau}d\tau \end{aligned} \tag{4.52}$$

Where, * represents complex conjugate. Due to shift of the window function in time and frequency, short time Fourier transform having a local property, which is time function, but also a frequency function. For a given time t, $STFT(t,\omega)$ regards as the moment "local spectrum."

The performance of short-time Fourier transform (STFT) in many respects are ideal, but due to the interference of window function the characteristic becomes poor. From the uncertainty principle, STFT frequency-domain and time-domain characteristics is contradictory. Although the spectrum resolution is not high, there is no cross-term problems. No cross-term is at the cost of low-resolution spectra.

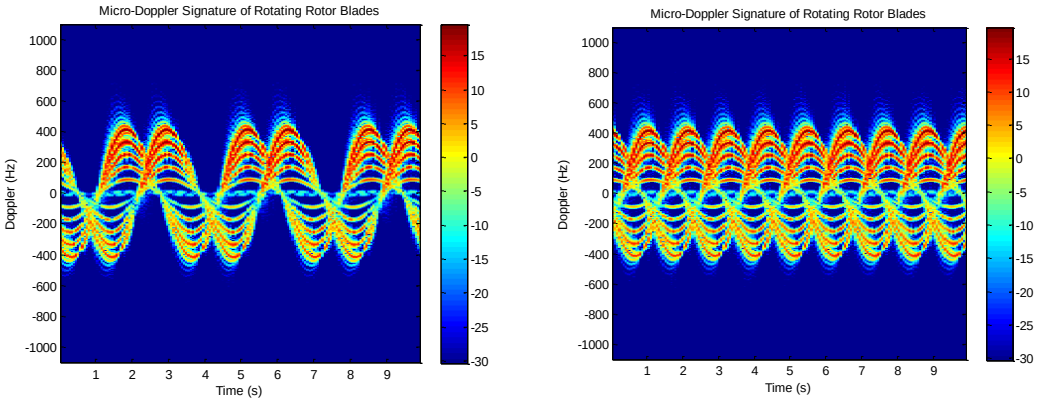

Figure 4.7 Rotating blades of two and three-blades micro-Doppler features

Rotating rotor blades micro Doppler features are represented in the joint time-frequency domain, in order to better explore time variations of Doppler characteristics. Micro-Doppler characteristics of the rotating blades with two blades and three blades are depicted in **Figure 4.7**.

From the Equation, the radar receive signal can be rewritten as

$$s_R(t) = \rho \exp\{ j[2\pi f_0 t + 4\pi \left(\frac{R_0 + D_v \sin \omega_v t \cos \beta \cos \alpha_\beta}{\lambda} \right)\} \tag{4.53}$$

Set $B = (4\pi / \lambda) D_v \cos \beta \cos \alpha_P$ and the received signal can be rewritten as

$$s_R(t) = \rho \exp\left\{ j \frac{4\pi}{\lambda} R_0 \right\} \exp\{ j2\pi f_0 t + B \sin \omega_v t\} \tag{4.54}$$

(4.54) can be expressed as a first class kth Bessel function,

$$J_k(B) = \frac{1}{2\pi} \int_{-\pi}^{\pi} \exp\{ j(B \sin u - ku)\} du \tag{4.55}$$

Thus,

$$
\begin{aligned}
s_R(t) &= \rho \exp\left(j\frac{4\pi}{\lambda} R_0 \right) \sum_{k=-\infty}^{\infty} J_k(B) \exp[\, j(2\pi f_0 + k\omega_v)t] \\
&= \rho \exp\left(j\frac{4\pi}{\lambda} R_0 \right) \{ J_0(B) \exp(j2\pi f_0 t) + \\
&\quad J_1(B) \exp[\, j(2\pi f_0 + \omega_v)t] - J_1(B) \exp[\, j(2\pi f_0 - \omega_v)t + \\
&\quad J_2(B) \exp[\, j(2\pi f_0 + 2\omega_v)t] + J_2(B) \exp[\, j(2\pi f_0 - 2\omega_v)t] + \\
&\quad J_3(B) \exp[\, j(2\pi f_0 + 3\omega_v)t] - J_3(B) \exp[\, j(2\pi f_0 - 3\omega_v)t] + \ldots \}
\end{aligned}
\tag{4.56}
$$

Therefore, the micro-Doppler spectrum makes up by the center frequency f_0 and the spacing of the adjacent pairs spectral lines of $\omega_v / (2\pi)$.

Obviously, even and odd blades Doppler shape is different. Even blades produce symmetric Doppler graphics around the mean Doppler frequency, but odd blades produce a symmetry Doppler graphics around the mean Doppler frequency. From the characteristic of micro-Doppler in the joint time-frequency domain, can be estimated from the number and speed of the tip of the blade, blade length. These characteristics of the wind turbine operation are important.

Chapter 5 Application radar technology to monitor and diagnose wind turbine blades

5.1 Wind Turbine Space Mathematic Model

Geometry of radar and rotating blade is shown in **Figure 5.1**. Radar located spatially fixed coordinate origin point (X, Y, Z), and the rotor center located at the origin point of the object fixed coordinate, and rotate at an angle velocity Ω around the x-axis in plane (y, z). The reference coordinate in parallel with the spatially fixed coordinate, and convert to the space fixed coordinate. From the radar to the reference coordinate origin distance is R_0. The origin point Azimuth and elevation observed from radar reference coordinate are α, β respectively.

From view point of electromagnetic scattering, each rotor blade is made up by some scattering centers. Each scattering center is considered as a point having a certain reflectivity. For simplicity, the same reflectance is assigned to all the scattering centers. Set $\alpha = \beta = 0^\circ$, if the scattering point P at $(x_0, y_0, z_0 = 0)$ with a constant angular velocity Ω rotates around z axis in the object fixed coordinate, the distance from origin of the fixed coordinate to the scattering point P is $l_P = \left(x_0^2 + y_0^2\right)^{1/2}$.If t=0, initial rotation angle is ϕ_0, then at time t rotation angle become

$\phi_t = \phi_0 + \Omega_t$, P point is rotated to $(x_t = 0, y_t, z_t)$, shown in **Figure 5.2**. Therefore, the distance from the radar to point P becomes

$$\begin{aligned} R_P(t) &= [R_0^2 + l_P^2 + 2l_P R_0 \cos(\phi_0 + \Omega t)]^{1/2} \\ &\cong R_0 + l_P \cos\phi_0 \cos\Omega t + l_P \cos\phi_0 \cos\Omega t \end{aligned} \tag{5.1}$$

Assuming that in the far field, $\left(l_P / R_0\right)^2 \to 0$ .Therefore, the scattering signal radar received by point P is

$$s_R(t) = \exp\left\{-j\left[2\pi f_0 t + \frac{4\pi}{\lambda} R_P(t)\right]\right\} = \exp\{-j[2\pi f_0 t + \Phi_P(t)]\} \tag{5.2}$$

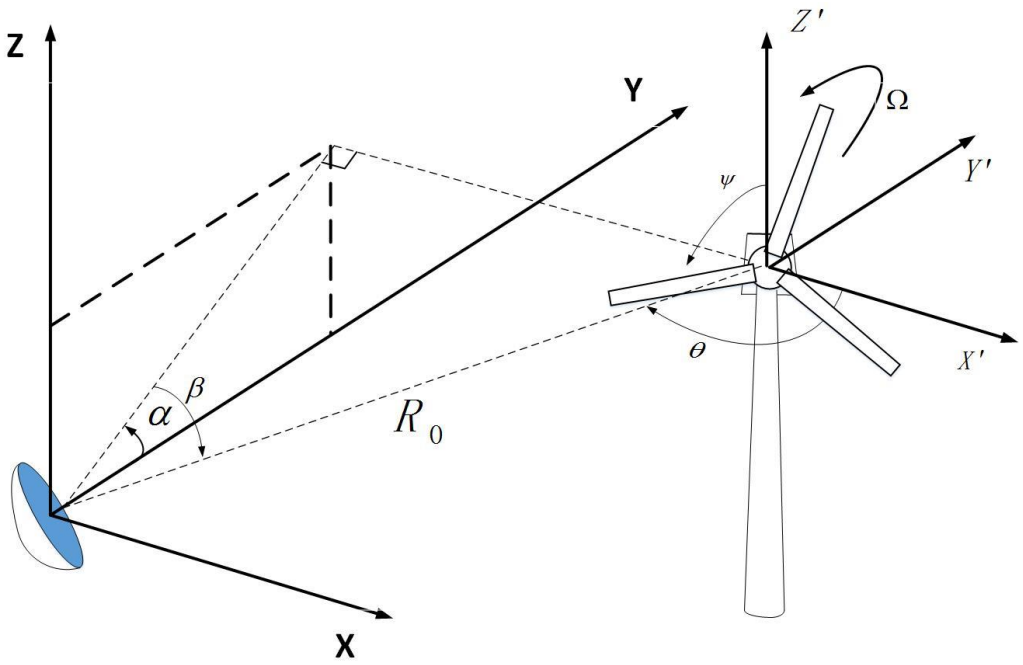

Figure 5.1 Geometric of radar and the rotation wind turbine

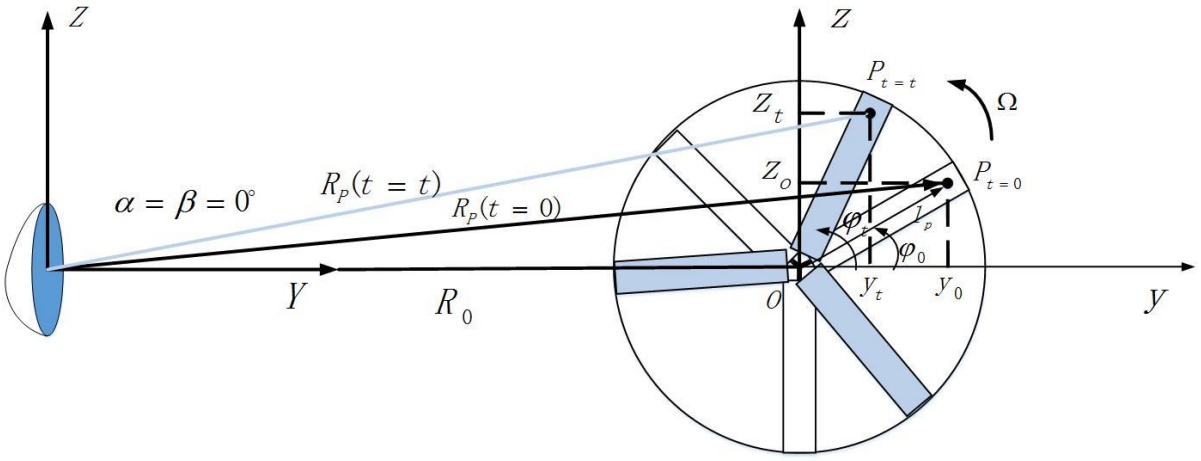

Figure 5.2 Geometric of radar and the rotation rotor blades

Where, $\Phi_P(t) = 4\pi R_P(t)/\lambda$ is the scattering phase function.

If the pitch angle β of the blades and the height x_0 of blades is not zero, the corrected phase function is

$$\Phi_P(t) = \frac{4\pi}{\lambda}[R_0 + z_t \cos\beta + x_0 \sin\beta] \tag{5.3}$$

Where, $z_t = l_P \cos\phi_0 \cos\Omega t + l_P \sin\phi_0 \sin\Omega t$

Therefore, the echo signal from scattering point P of becomes

$$s_R(t) = \exp\left\{-j\frac{4\pi}{\lambda}[R_0 + x_0 \sin\beta]\right\}\exp\left\{-j2\pi f_0 t - \frac{4\pi}{\lambda} l_P \cos\beta \cos(\Omega t + \phi_0)\right\} \tag{5.4}$$

Set $\phi_0 = 0^\circ$, $B = (4\pi/\lambda) l_P \cos\beta$; then the Equation(5.4) can be represented as a first-order Bessel function.

Integrate baseband signal of Equation (5.4) in the entire length of the blade L, obtain the total base band signal [71-72] is

$$s_L(t) = \exp\left\{-j\frac{4\pi}{\lambda}[R_0 + x_0\sin\beta]\right\}\int_0^L \exp\left\{-j\frac{4\pi}{\lambda}l_P\cos\beta\cos(\Omega t + \phi_0)\right\}dl_P$$
$$= L\exp\left\{-j\frac{4\pi}{\lambda}[R_0 + x_0\sin\beta]\right\}\exp\left\{-j\frac{4\pi}{\lambda}\frac{L}{2}\cos\beta\cos(\Omega t + \phi_0)\right\}\mathrm{sinc}\left\{\frac{4\pi}{\lambda}\frac{L}{2}\cos\beta\cos(\Omega t + \phi_0)\right\}$$

(5.5)

Where, $\mathrm{sinc}(\cdot)$ is Sinclair function: $\mathrm{sinc}(x) = 1$, when $x = 0$, $\mathrm{sinc}(x) = \sin(x)/x$, when $x \neq 0$

For the rotor blades of N, N blades having N different initial rotation angle:

$$\theta_k = \theta_0 + k2\pi / N \ \ (k = 0,1,2,..,N-1)$$

Characteristics of the total received signal in time domain becomes

$$s_\Sigma(t) = \sum_{k=0}^{N-1} s_{L_k}(t) = L\exp\left\{-j\frac{4\pi}{\lambda}[R_0 + x_0\sin\beta]\right\}\sum_{k=0}^{N-1}\mathrm{sinc}\left\{\frac{4\pi}{\lambda}\frac{L}{2}\cos\beta\cos(\Omega t + \phi_0 + k2\pi/N)\right\}\exp\{-j\Phi_k(t)\}$$

(5.6)

Where, the phase function is

$$\Phi_k(t) = \frac{4\pi}{\lambda}\frac{L}{2}\cos\beta\cos(\Omega t + \phi_0 + k2\pi/N) \ \ (k = 0,1,2,..,N-1) \qquad (5.7)$$

Assuming that radar working in L-band (1-2GHz) in far field, wavelength is $\lambda = 0.199m$ and the distance resolution is 1m. The wind turbine has two main blades rotating at a constant rate $\Omega = 0.2rad/s$. If the blade length from the blade root to the tip is L = 25.5m, then in the elevation $\beta = 30^\circ$, from the radar to the blade center is 163.30m. According to the length of the blade tip and the rotational speed, the tip speed is $V_{tip} = 2\pi L\Omega = 32.0442m/s$, and therefore,

the maximum Doppler shift is $\{f_D\}_{\max} = (2V_{tip}/\lambda)\cos\beta = 277.70Hz$. Therefore, Nyquist sampling frequency is $2\times 277.7Hz = 555.4Hz$. Using 2200Hz sampling frequency, which is greater than the Nyquist sampling rate, the spectrum of the same signal is shown in **Figure 5.3**. There is no aliasing.

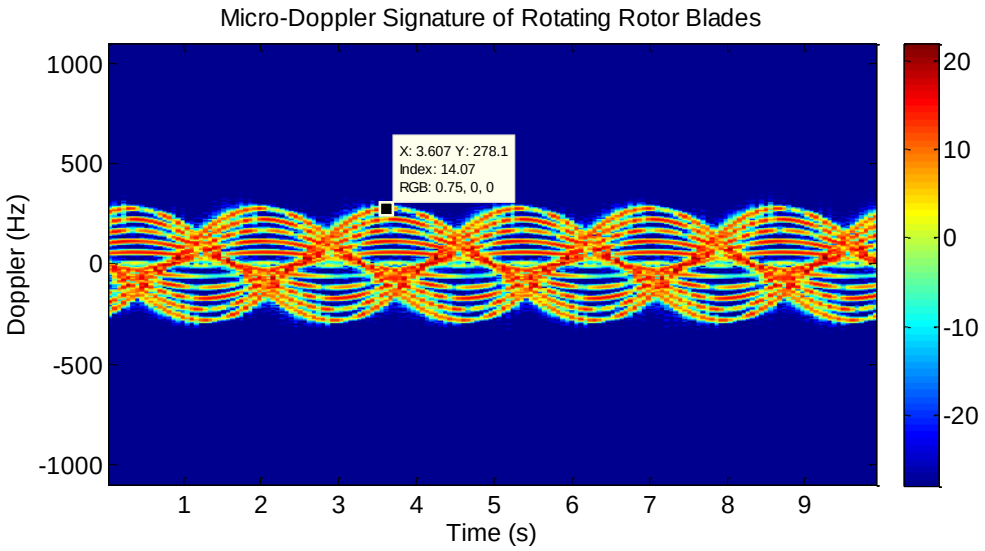

Figure 5.3 Micro-Doppler Signature of Rotating Rotor Blades

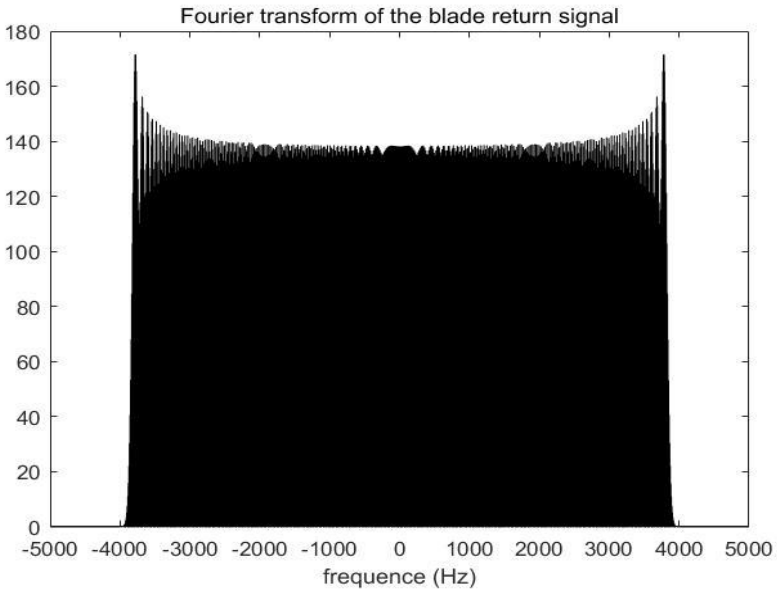

Figure 5.4 Micro-Doppler Signature of Rotating Rotor Blades

The Doppler modulation caused by the rotation is considered a unique feature of the rotating blades. In the joint time-frequency domain, represent this Doppler modulation, we can see the blades micro-Doppler features. It is a three rotating blades micro-Doppler features, as shown in **Figure 5.3**.

Due to the rotating blades modulate the echo signal, in the frequency domain, the Doppler frequency shift caused by rotation occupy a unique position. **Figure 5.4** shows the spectral component of rotating blades without rotor hub, due to wind turbine blades has no translational motion, the Doppler frequency should be around zero doppler.

Because the time derivative of the phase function is the instantaneous frequency of the signal, take time derivative of the phase function $\Phi_k(t)$ in (5.7), the instantaneous Doppler frequency shift caused by the k-th rotating blades is

$$f_{D,k}(t) = \frac{L}{\lambda}\Omega\cos\beta[-\sin(\phi_0 + k2\pi/N)\sin\Omega t + \cos(\phi_0 + k2\pi/N)\cos\Omega t] \quad (5.8)$$

Doppler shift is modulated by the rate of rotation through two sine function.

5.1.1 RCS Model of Rotating Wind Turbine Blade

In order to calculate the electromagnetic scattering from the rotating blades, for simplicity, blades is simplified to a rigid, uniform and linear rectangular plate, with a constant rotation rate around a fixed axis, and does not consider the leading and trailing edges. Geometry of blade sand radar are shown in **Figure 5.5**. For a perfectly conducting rectangular plate, RCS mathematical equation can be found in [73-74]. RCS approximate equation of rectangular plate given in [73]. There are two terms in the equation RCS: peak RCS σ_{Peak} and direction factor σ_{Aspect} :

$$\sigma = \sigma_{Peak}\sigma_{Aspect} = \frac{4\pi a^2 b^2}{\lambda^2}\left(\cos\theta\frac{\sin x_k}{x_k}\frac{\sin y_k}{y_k}\right)^2 \quad (5.9)$$

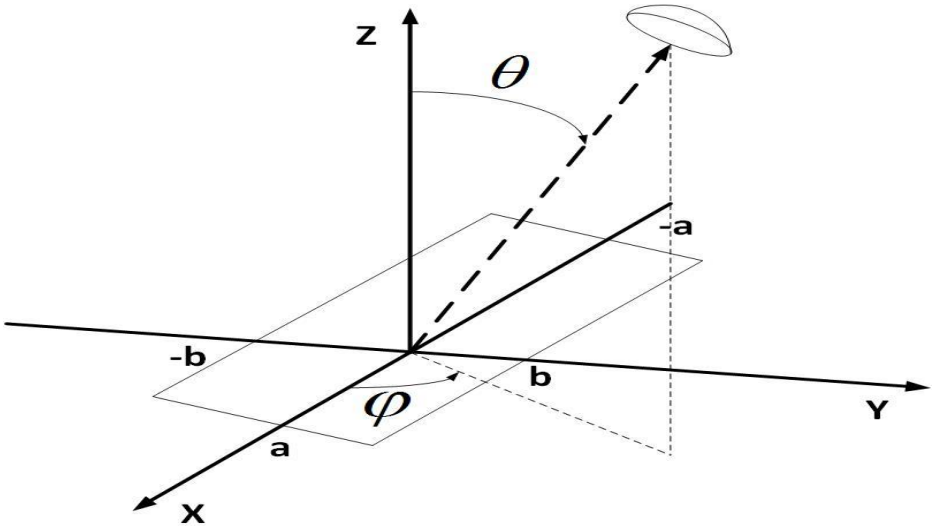

Figure 5.5 The RCS of Rectangular plate

Where, $\sigma_{Peak} = \frac{4\pi a^2 b^2}{\lambda^2}$, $\sigma_{Aspect} = \left(\cos\theta \frac{\sin x_k}{x_k} \frac{\sin y_k}{y_k} \right)^2$, $x_k = ka \sin\theta \sin\phi$,

$y_k = kb \sin\theta \cos\phi$ and $k = 2\pi / \lambda$.

Equation (5.9) is a polarization-independent, and only little perspective $\theta \leq 20^\circ$ is accurate.

5.1.2 Radar Backscattering from a Rotating Wind Turbine Blade

The rotating blades can be obtained by follow: position and direction can be calculated by a rotation matrix of zero roll and pitch angle. The yaw angle is decided by given initial angle and rotation rate. Based on the position and direction of the blade, can be calculated the blade RCS and radar reflected signals. All blades reflected signal can be obtained by coherent super position of each individual blade radar signal.

Coherent radar system emits a series of pulse width Δ and pulse repetition interval ΔT narrow rectangular pulses, and the receiver base band signal is

$$s_B(t)=\sum_{k=1}^{n_p}\sum_{n=1}^{N_B}\sqrt{\sigma_n(t)}\cdot rect\left\{t-k\cdot\Delta T-\frac{2R_n(t)}{c}\right\}\cdot\exp\left\{-j2\pi f_c\frac{2R_n(t)}{c}\right\} \quad (5.10)$$

Where, N_B is the total number of blades, and n_P is the total number of pulses received. f_c is the radar transmit frequency. $R_n(t)$ is the distance between the radar and the nth blades at time t. $\sigma_n(t)$ is the n-th blade RCS at time t, while rect is defined as the rectangular function $rect(t)=1(0\le t\le\Delta)$.

In Equation (5.10), we need to calculate two variables $R_n(t)$ and $\sigma_n(t)$. RCS of conductor rectangular plate can be calculated by the equation(5.9). Equation (5.9) is accurate only for $\theta\le 20^\circ$. Variable distance from the radar to the center of rectangular plane.

Geometry of radar and blade is shown in **Figure 5.1**, radar located at $(X_1=111.8m, Y_1=100m, Z_1=-50m)$, the wave length of 0.199m, the rotor center located at $(X_0=0m, Y_0=0m, Z_0=0m)$, length of the blade $L=25.5m$, and the blade root in $L_1=0.5m$ and tip in $L_2=25.5m$, the width of the tip $W=1m$. The rotation rate is $\Omega=0.5r/s$. Azimuth ϕ and viewing angle θ can be calculated by the geometric relationship between the radar position and the blade position. By specifying the scattering center in the tip of each blade, can be obtained receiver base band signal from the Equation (5.10), and RCS is calculated by Equation (5.9), one-blade and three-blade of two-dimensional pulse-distance profile is shown in **Figure 5.6** and **Figure 5.7**, and its micro-Doppler features are shown in **Figure 5.8**..

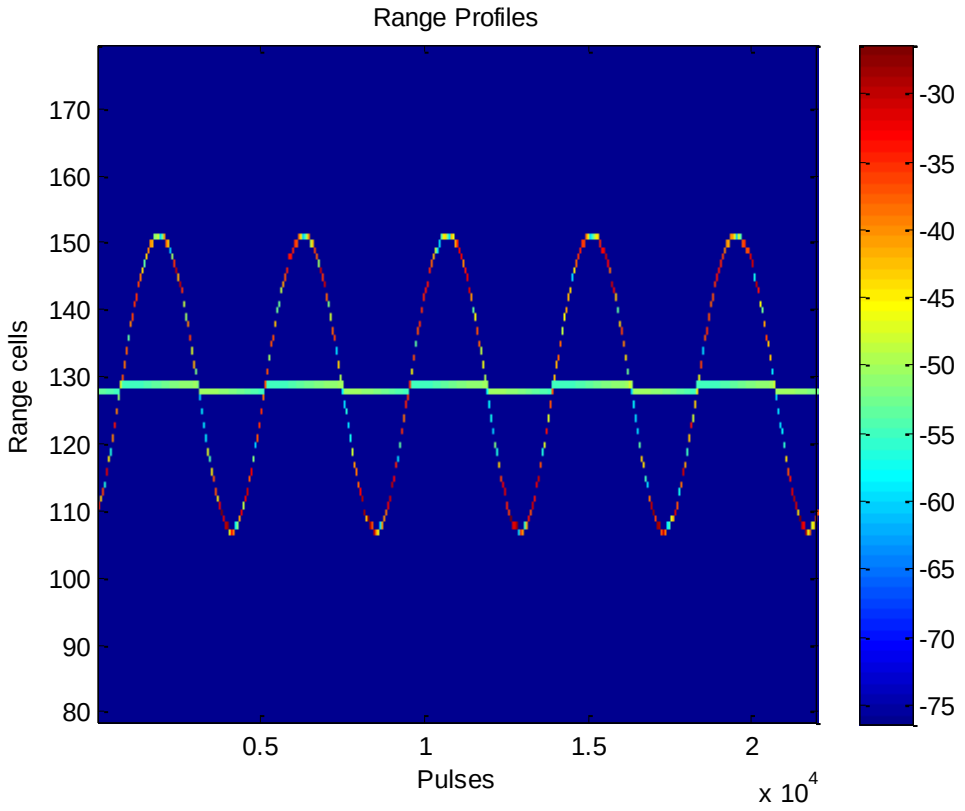

Figure 5.6 One blade tip scattering signal in time domain

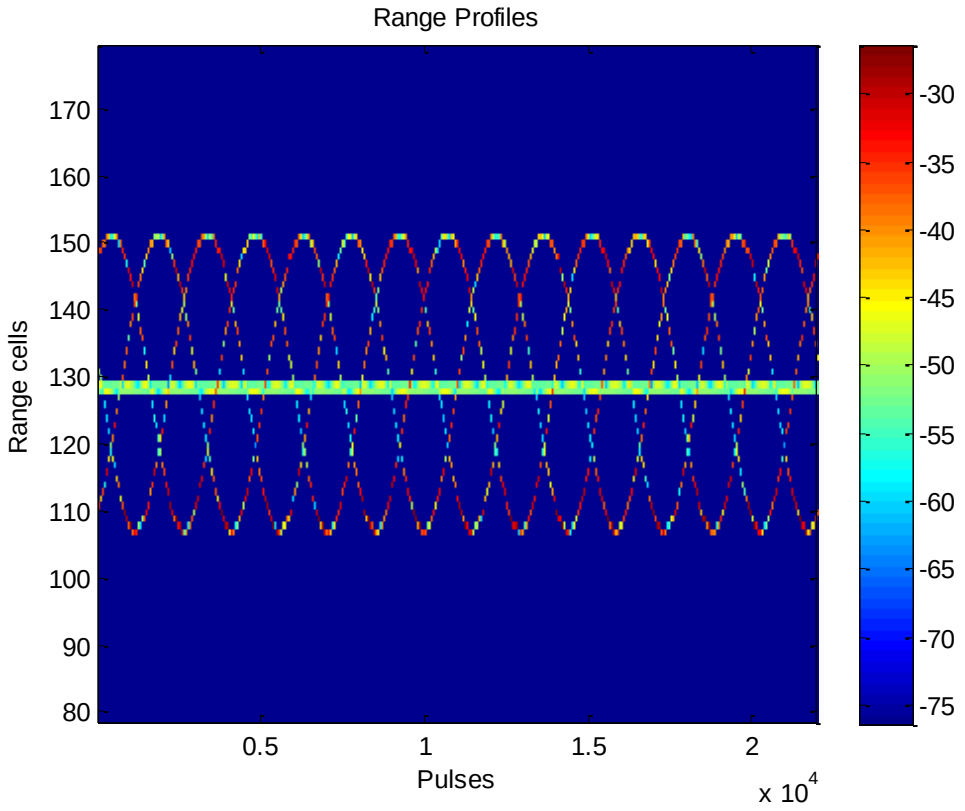

Figure 5.7 Three blade tip scattering signal in time domain

From the space model of **Figure 5.1**, we got two range profiles. As can be seen from **Figure 5.6**, there is a one blade wind turbine rotating, and from **Figure 5.7**, it also shows the wind turbine is located at a distance of 129 unit from radar equaling 129.10 m from the radar.

5.2 Wind Turbine Micro-Doppler Signature

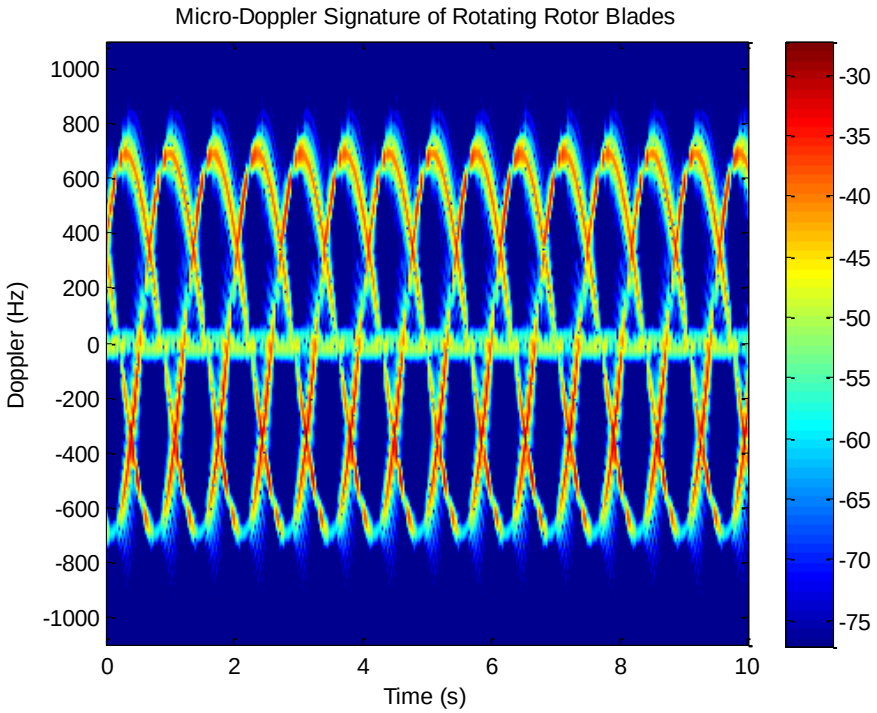

Figure 5.8 Three blades tip scattering signal in joint time-frequency domain

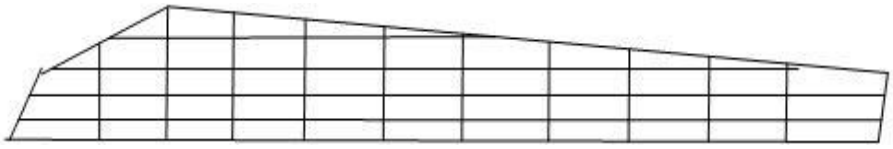

Figure 5.9 Blade model

More accurate model radar back scattering of the blades is the physical optics surface model. Rectangular blade represented by rectangular area arrays, as shown in **Figure 5.9**. Scattering center of each rectangular are assumed at original coordinate center. Radar receiver base band signal is

$$s_B(t) = \sum_{k=1}^{n_P} \sum_{n=1}^{N_P} \sum_{m=1}^{N_F} \sqrt{\sigma_{n,m}(t)} rect\left\{ t - k\Delta T - \frac{2R_{n,m}(t)}{c} \right\} \exp\left\{ -j2\pi f_c \frac{2R_{n,m}(t)}{c} \right\} \quad (5.11)$$

Where, N_B is the number of blades. N_F is the total number of ocular surface of each blade. n_P is the total number of pulse in radar observation time interval.

Based on specific physical optics model, radar distance profile and three-blade micro-Doppler features are shown in **Figure 5.10** and **Figure 5.11**.

.

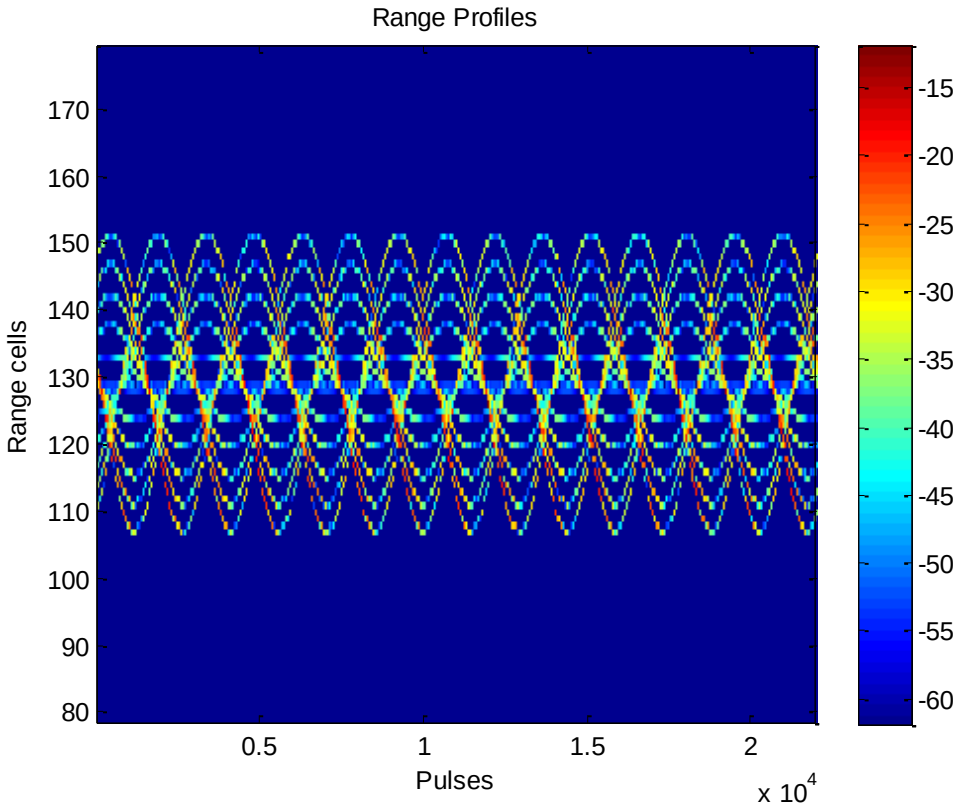

Figure 5.10 Range Profile of radar backscattering of the blades

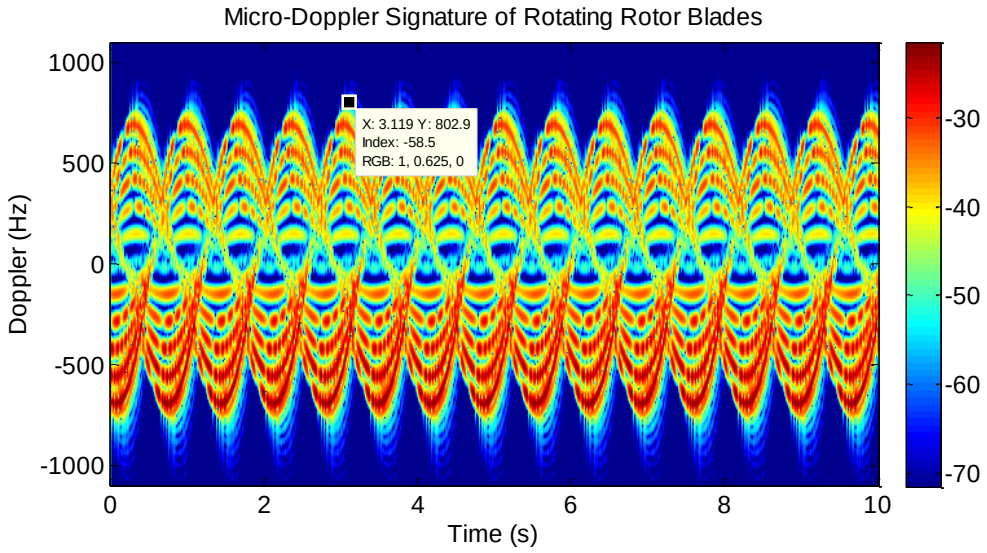

Figure 5.11 Radar distance profile and three-blade micro-Doppler features

From the micro-Doppler features we can estimate the number of the blade, blade length and rotation rate of the blade.

5.3 Analysis of the Micro-Doppler Signature of Wind Turbine Blade Observed in Radar

Case 1 Wind turbine blades healthy operation

In this case, we suppose wind turbine blades work in healthy condition. Assume that radar works in 1.5GHz,located at (x = 111.8m, y = 100m, z = -50m), the Pulse repeat frequency (PRF) of 2200 Hz, and the time duration of 10 s. the wind turbine blade length of 25.5 m rotating around x axis and angular velocity $0.3\times 2\pi$ rad / s. Assuming that the blade rotation center is located at $(x=0m, y=0m, z=0m)$;

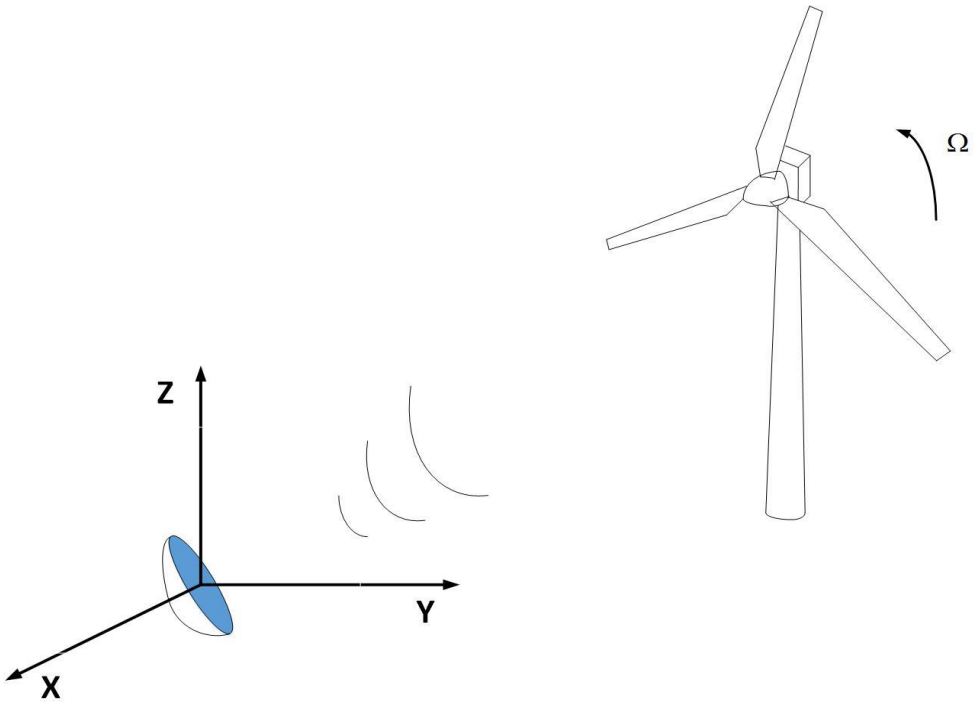

Figure 5.12 Geometry of radar and wind turbine blades

In **Figure 5.12** the rotation period can be obtained from rotational angular velocity. $T_0 = 2\pi / \|\omega\| = 3.33s$, The number of the blade is three, which can be seen from **Figure 5.13**. Because the wind turbine capacity is relative to blade length, we decide the tip of blades equals 25.5 m (600kw-800kw wind turbine), blades length can be derived from the **Figure 5.12** about 26 m (included hub 0.5 m). The rotation rate of the tip of blade can be calculated from the above information about $2\pi \times L \times \Omega = 48.066m/s$. The maximum micro Doppler frequency is $f_{D\max} = 480.99Hz$, as shown in **Figure 5.14**.

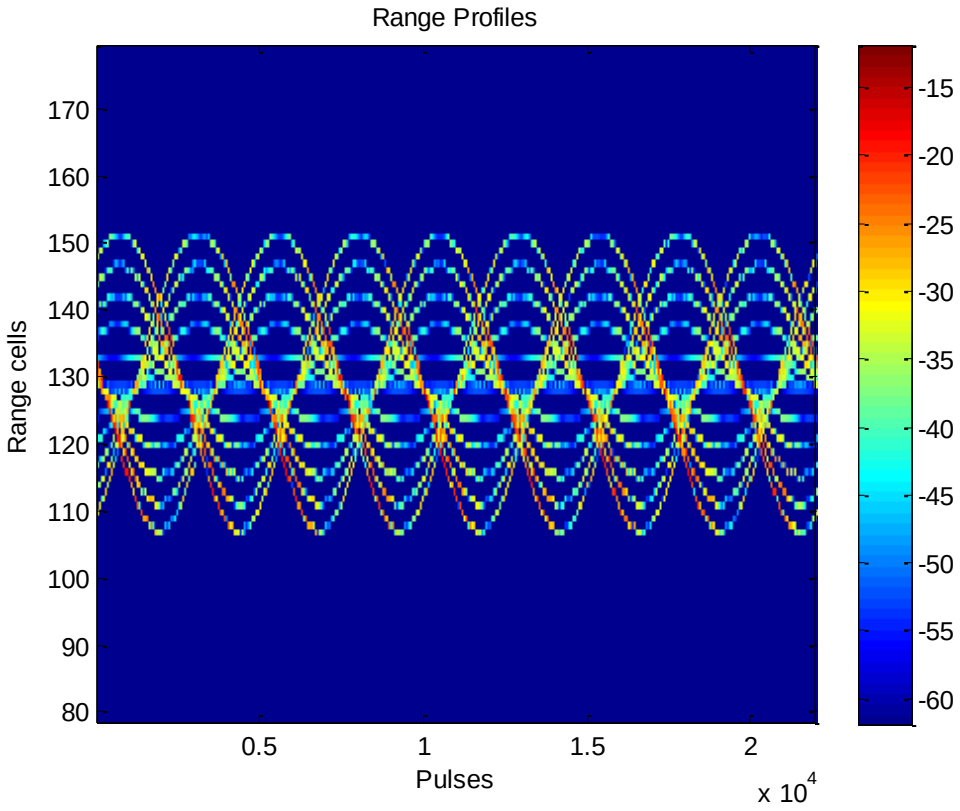

Figure 5.13 Rotating rotor blades micro Doppler characteristics: Range Profile

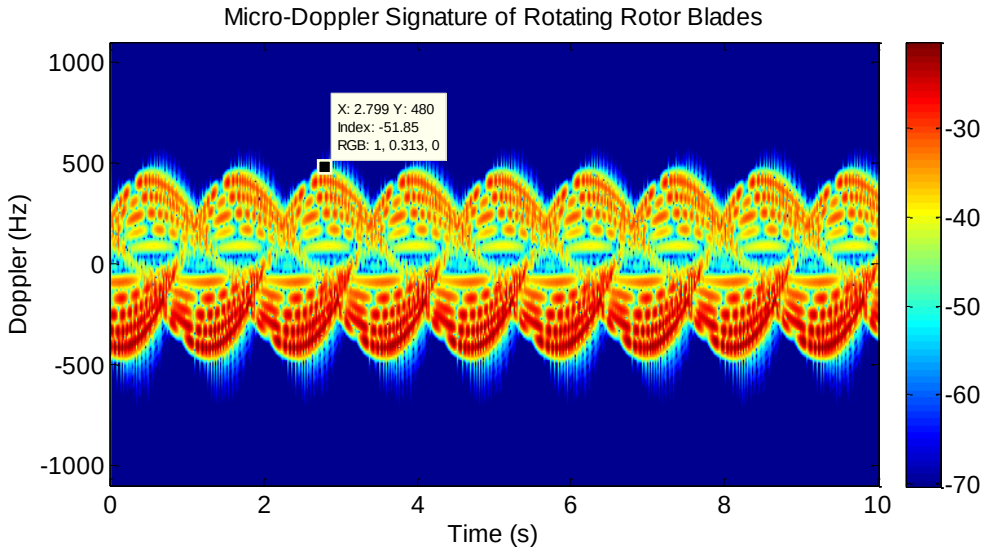

Figure 5.14 Rotating rotor blades micro Doppler characteristics: Micro Doppler Signature

Case 2 Wind turbine blades vibration operation

Wind turbine parameters used as Case 1, set one blades vibrates along x axis with vibration amplitude 1 meters with vibration frequency of $2\times 2\pi$ rad/s, as shown in **Figure 5.15**.

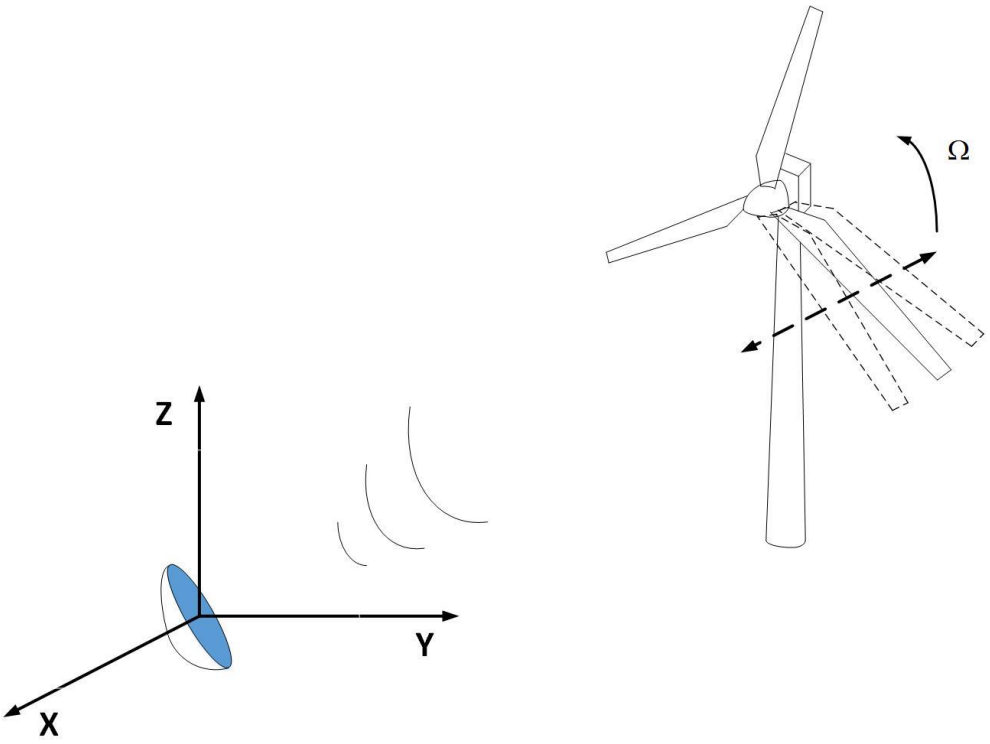

Figure 5.15 Geometry of radar and wind turbine blades

Range profile and Micro-Doppler characteristics of the rotating blades with three blades depicted in **Figure 5.16** and **Figure 5.17** respectively. Obviously three blades produce in **Figure 5.17** showing asymmetry Doppler graphics around the mean Doppler frequency. From blades micro- Doppler frequency in joint time-frequency domain, we can estimate the number of the blades (3), speed of the blade tip (320.44m/s) and blade length (25.5m), as case 1 mentioned.

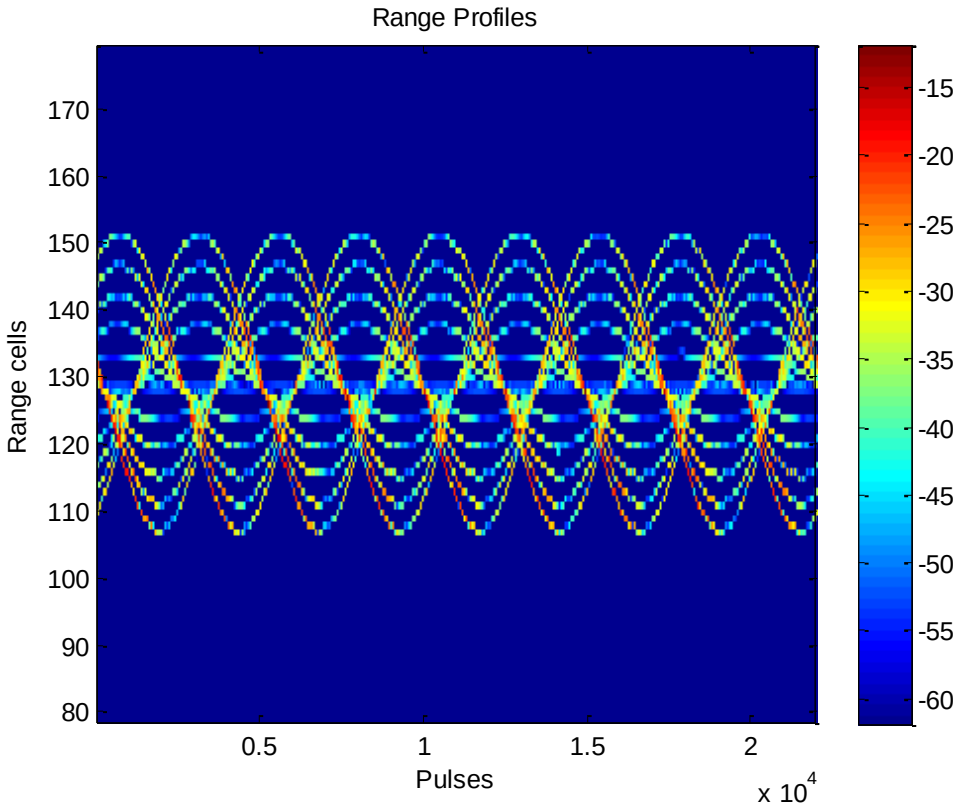

Figure 5.16 Wind turbine blades waveform with vibration in time domain

In **Figure 5.16** and **Figure 5.17**, we can see there is a slightly deformation of the blades waveform in Range Profile.

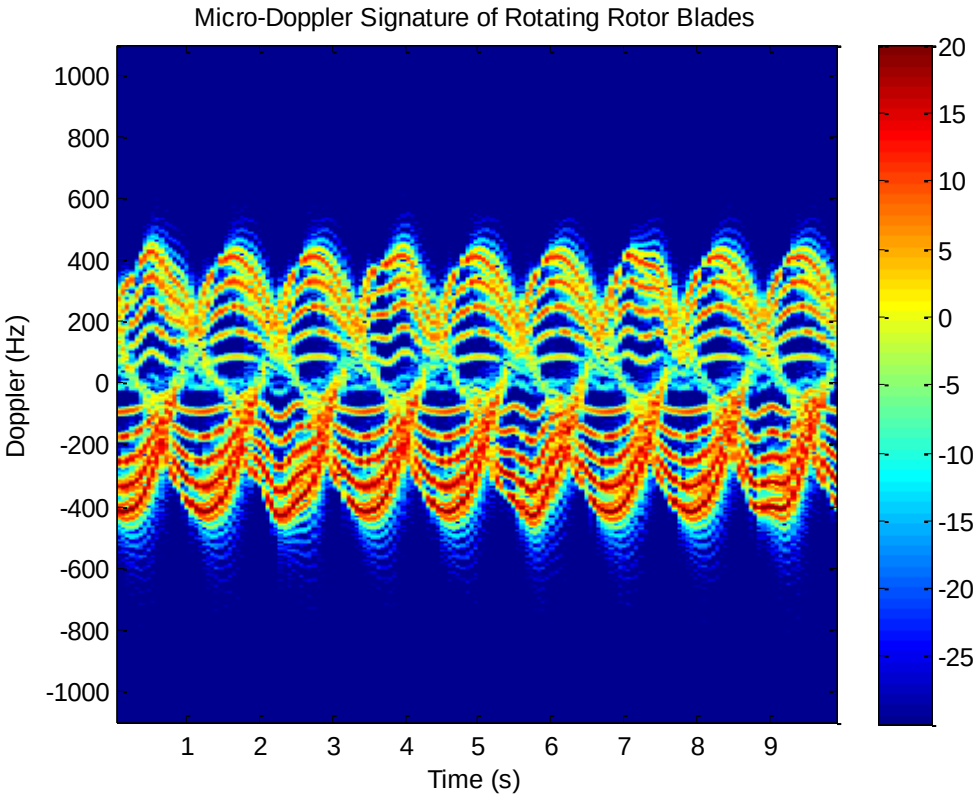

Figure 5.17 Wind turbine blades micro-Doppler features

Case 3 Wind turbine blades of corrosion operation

Wind turbine parameters used as Case 1, set part of three blades are corroded by changing the RCS of some specific pieces, which is shown in **Figure 5.18**.

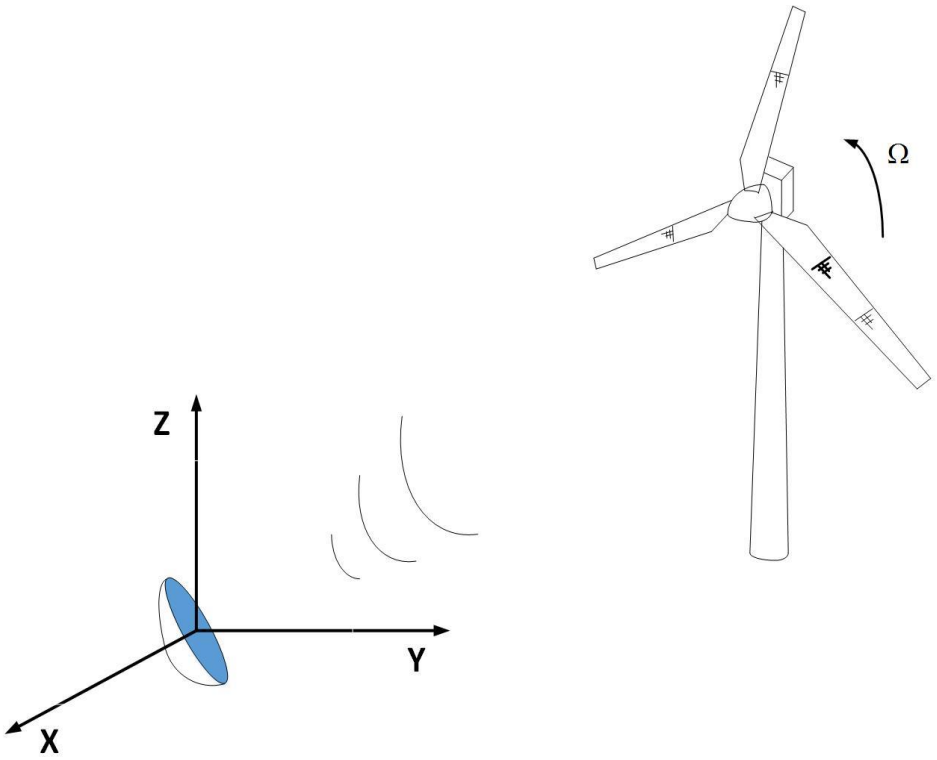

Figure 5.18 Geometry of radar and wind turbine blades

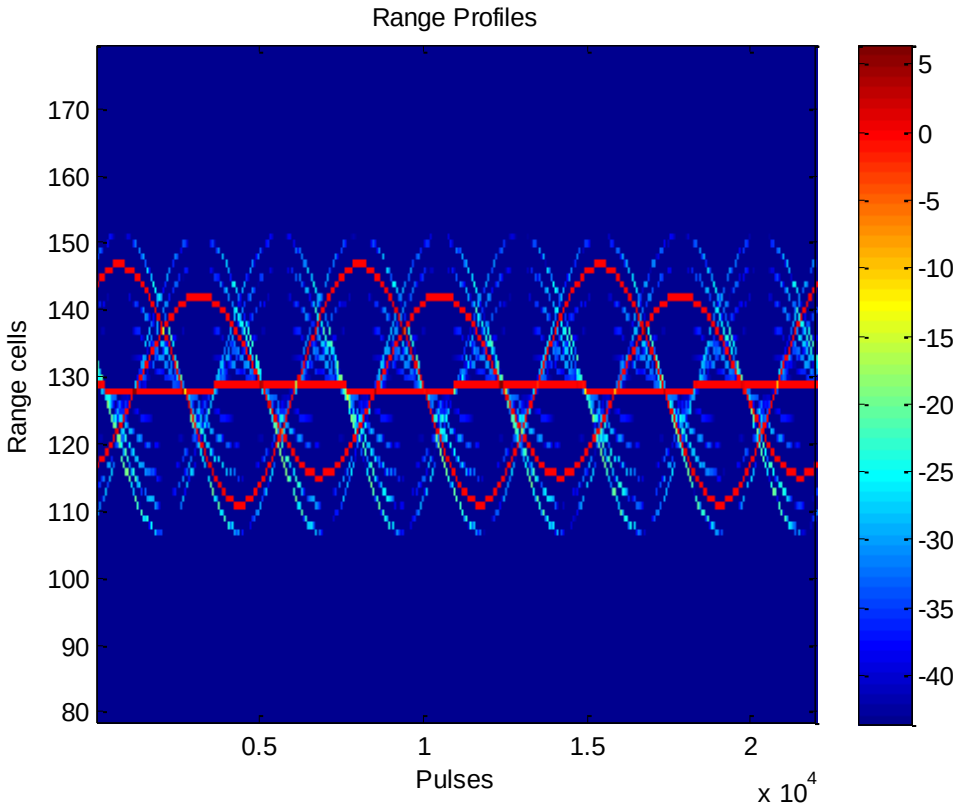

Figure 5.19 Wind turbine corrosion model in time domain

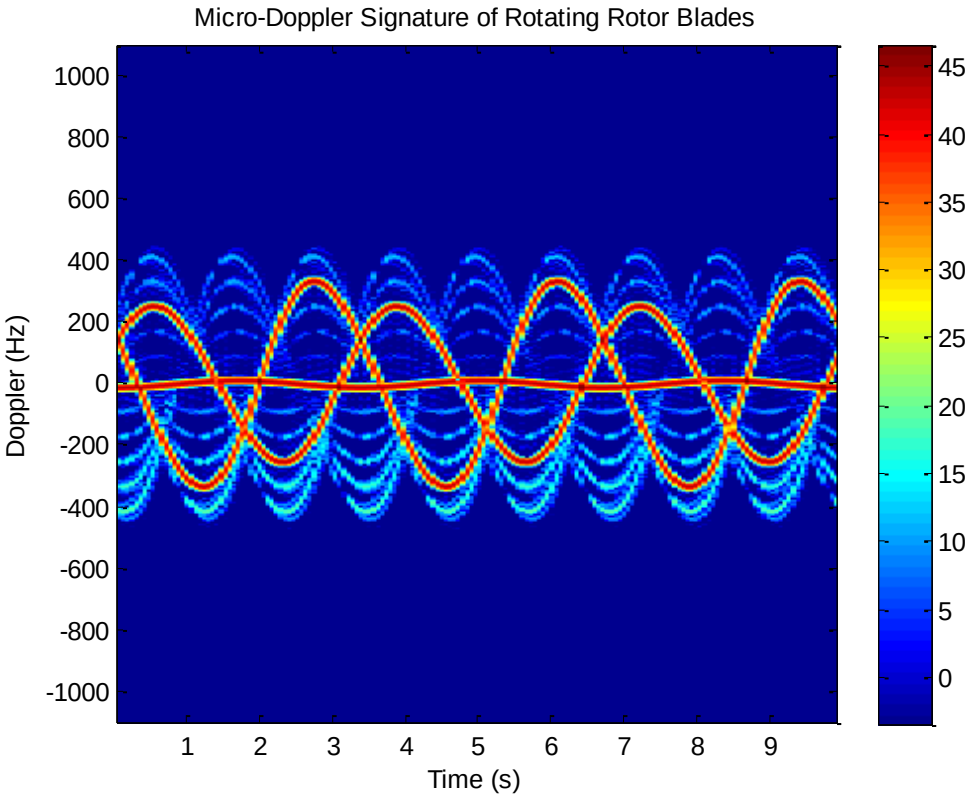

Figure 5.20 Wind turbine blades micro-Doppler feature

The radar back scattering model is shown in **Figure 5.18**. In **Figure 5.19** and **Figure 5.20**, it is clear that the scattering in some parts near the root, middle and tip of blades are different other parts of blades, which means some broken may occur in that area. The red curve means the RCS in that specific part is abnormal.

In this chapter, the blade model is divided into several small pieces, using RCS technical to analysis blade back scattering signal. We designed healthy, vibration and corrosion three modes to test, and received radar echo signals, and apply STFT of the echo analysis. In next chapter, we are going to extract blade operation data with a new method to analysis operation condition.

Chapter 6 Blades Innovations analysis using radar technology

6.1 Wind Turbine Blades Condition Classification Based on Doppler Characteristics Exploiting Krawtchouk Moments

Wind turbine blades classification system is presented in this thesis. A model and a robust framework is developed, which involved different micro Doppler based on Krawtchouk moment. The reliability of proposed framework is tested by simulation data.

Krawtchouk moments do not require approximation integration and transfer to space coordinates, there is no discretization error, which accuracy is only concerned with the high-order value transmission error. Classic Krawtchouk moments in the calculation of the large image of higher order moments, will produce values diverge, causing image cannot be accurately reconstructed. Yap suppressed fluctuation by weight normalizing classical Krawtchouk polynomials, effectively inhibited the polynomial numerical divergence, and use the symmetry of x direction to reduce the amount of the moment calculation and the accumulated error [75]. Krawtchouk moments are independent moment obtained by a set of orthogonal polynomials, that allow us obtain more information in the same number of coefficients (to be used in target classification). Consequently, the Krawtchouk moments are selected as feature to classify different micro Doppler signature.

6.1.1 Classification algorithm based on Krawtchouk moment

Phase change induced by micro motion will occur in the sidebands of spectrum signature. Short Time Fourier Transform (STFT) will constantly monitor the frequency in each time bin which is useful to characterize the classification of signals. Micro Doppler signature requires a robust

feature extraction to concisely describe the micro motion. In this section, the proposed approach exploits the discrete Krawtchouk moments to extract feature vectors representing the wind turbine blades rotating condition to perform state classification. Krawtchouk moments that can represent a detected targets with limited set of features and limited computation complexity, providing robust performance for state classification, with high reliability to noise interference and reduced sensitive to discretization errors. Specifically, the proposed algorithm consists of the extraction Krawtchouk moments from the cadence velocity diagram (CVD); the advantage of CVD is robust to the initial phase of micro motion and it removes the zero periodicity component before calculating by Krawtchouk moments [76].

A. Feature Extraction Algorithm

The proposed micro Doppler feature extraction algorithm is summarized in block diagram shown in **Figure 6.1**. The starting point is the signal s(n), n=0,…,N-1, containing micro Doppler signature and N number of signal samples. It can be modeled as the returns from sum of the different part of target micro motion [77].

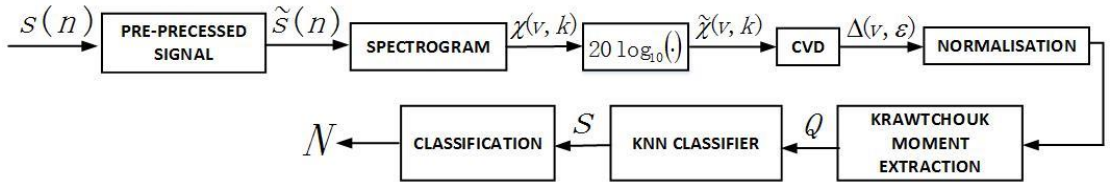

Figure 6.1 Micro Doppler feature extraction algorithm

$$s(n) = \sum_{i=1}^{I} \gamma_i \exp\left\{ -j \frac{4\pi}{\lambda} (v_i n + \alpha_i \cos(2\pi\theta_i n + \varphi_i) + \beta_i) \right\} \tag{6.1}$$

Where I is the total number of scatters, γ is the amplitude related to the scatters electromagnetic reflectivity, v is the bulk motion velocity, α is the micro motion spatial displacement, θ is the micro motion frequency, φ is the initial phase of the micro motion (e.g. the initial position of the wind turbine placement), and β is the initial phase relative to the target range.

The received signal need to be preprocessed before making micro Doppler evaluation. The first block converts $s(n)$ into a zero mean and unit variance signal $\tilde{s}(n)$. The second step is spectrogram calculation of pre-processing signal $\tilde{s}(n)$.

$$\chi(v,k)=\left|\sum_{n=0}^{N-1}\tilde{s}(n)w^{*}(n-k)\exp(-j2\pi vn/N)\right|^{2} \quad \text{, k=0,...,K-1} \tag{6.2}$$

Where v is the normalized frequency, $w(\cdot)$ is the smoothing window. The spectrogram is a time-frequency distribution, and it is chosen for its robustness with respect to interference terms.

In order for the data to be stable and compress data size, the logarithm can be used.

$$\tilde{\chi}(v,k)=20\log_{10}\chi(v,k) \tag{6.3}$$

In the next step, the cadence velocity diagram (CVD) is used to extract micro Doppler features, which is defined as the Fourier transform of each frequency bin[78]. The CVD is more suitable to wind turbine blade monitor than spectrogram since it not depends on the initial phase of moving targets. The CVD of Case 1 in Chapter 5obtained from spectrogram is shown in **Figure 6.2**. in which it is can be seen that the zero cadence component is filter out. The CVD also provides the cadence of each frequency and maximum micro Doppler shift. In specific, all the component with their own cadence located in the cadence frequency axis and their micro Doppler shift magnitude located in the frequency axis.

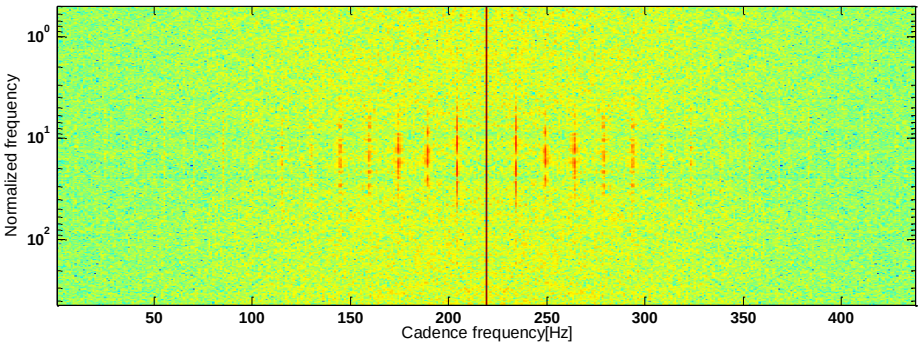

Figure 6.2 CVD from returns relative to rotation blade

$$\Delta(v,\varepsilon)=\left|\sum_{k=0}^{K-1}\tilde{\chi}(v,k)\exp(-j2\pi k\varepsilon/K)\right| \tag{6.4}$$

The third step of the algorithm is the projection of the CVD onto the basis of Krawtchouk polynomials. By applying(6.4) to $\Delta(v,\varepsilon)$ for each order of (n,m)

$$Q_{nm}=\sum_{x=0}^{N-1}\sum_{y=0}^{M-1}\bar{K}_n(x;p_1,N-1)\bar{K}_m(y;p_2,M-1)\Delta(v,\varepsilon) \tag{6.5}$$

The feature vector Q_{nm} has $(n+1)\times(m+1)$ elements and results are

$$Q_{nm}=[Q_{00},...,Q_{nm}] \tag{6.6}$$

Finally, Q_{nm} is normalized using the following rescaling in order to avoid particular feature impacts the classification [79].

$$\tilde{Q}_{nm}=\frac{Q_{nm}-\mu Q_{nm}}{\sigma Q_{nm}} \tag{6.7}$$

Where $\mu\mathrm{Q}_{\mathrm{nm}}$ is the mean, $\sigma\mathrm{Q}_{nm}$ is standard deviation of feature vectors. The feature vectors are micro Doppler signature then used to populate as input of a classifier for identifies each specific class.

B. Classification and k-Nearest Neighbor (kNN) classifier

kNN algorithm is a non-parametric classification algorithm, which has been widely used in various fields of pattern recognition. The principle of kNN: when we give a sample x to be classified, first, we give a set training samples closest to x with K dimension which have been already known the class labels, and then according to the training sample labels to determine the sample x classification, as shown in **Figure 6.3**..

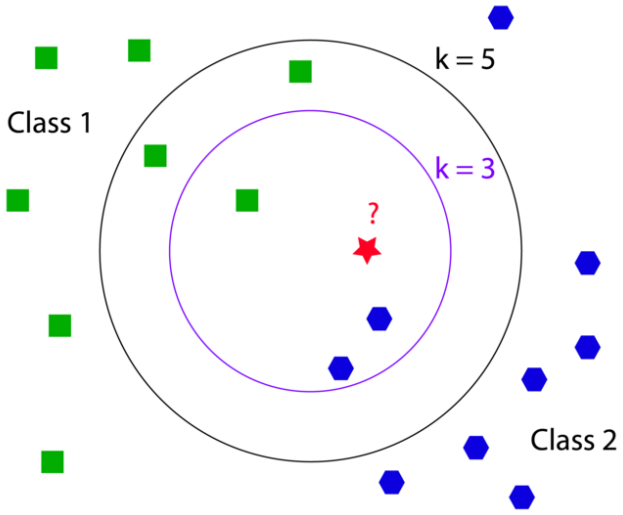

Figure 6.3 kNN classifier can obtain higher accuracy classification for the data of unknown and non-normal distribution, which has many advantages such as clear concept and easy implementation

Let K be the set of nearest neighbour training vectors for the feature vector Q , which is

$$K = \left\{ \tilde{Q}_1, \ldots, \tilde{Q}_k : \min_{\tilde{Q} \in T} \left\| \tilde{Q} - Q \right\| \right\} \tag{6.8}$$

Where T is the training vectors set, besides, make $l = [l_1, \ldots l_k]$ be the labels of the vectors of N, which can assume values in the range of $[1, N]$, where N is the number of possible classes. In order to consider the unknown class, the design rules will include two steps. First, the vector labels $l_i, i = 1, \ldots, k$, is updated as flows:

$$l_i = \begin{cases} 0 & \tilde{Q}_i \notin S_{CM_{l_i}}(\zeta_{l_i}) \\ l_i & otherwise \end{cases} \tag{6.9}$$

Where, $S_{CM_n}(\zeta_n)$ is an hypersphere with centre CM_n and radius ζ_n, and CM_n is the centre of mass of the training vectors belonging to the class n. Secondly, let s be (N+1) dimensional score vector that are defined as occurrence It allows the definition of 'unknown' class occurs.

When s does not have a sufficient score, we define a threshold η (the minimum values of the score to be allowed classify) and all the scores below η will not be allowed to classify labelled as 'unknown'. Eventually, the estimation rule is

$$\tilde{n} = \begin{cases} \arg\max_n s & if\ \exists!(\max s) > \eta \\ 0 & \end{cases} \tag{6.10}$$

6.1.2 Experimental Result on Simulated Data

In this section, the simulated model of the wind turbine blades described in section 5 is provided. Specifically, the return from the wind turbine blades has been simulated. The time domain signature of rotation blade is defined as:

$$s_{\Sigma}(t) = \sum_{k=0}^{N-1} s_{L_k}(t) = L\exp\left\{-j\frac{4\pi}{\lambda}[R_0 + x_0\sin\beta]\right\}\sum_{k=0}^{N-1}\sin c\left\{\frac{4\pi}{\lambda}\frac{L}{2}\cos\beta\cos(\Omega t + \phi_0 + k2\pi/N)\right\}\exp\{-j\Phi_k(t)\}$$

(6.11)

where L is the scattering coefficient of the blade (for simplicity we consider it equal to the dimensionless length of the blade L [5]), λ is the radar operative wavelength, R_0 is the distance from the radar to the origin of the reference coordinates, x_0 is the z-coordinate of the scattering center, β is the radar observed elevation angle, N is the number of blades, sinc(x) = sin(x)/x, and the phase function given by $\Phi_k(t)$,

$$\Phi_k(t) = \frac{4\pi}{\lambda}\frac{L}{2}\cos\beta\cos(\Omega t + \phi_0 + k2\pi/N)\ (k = 0,1,2,..,N-1) \tag{6.12}$$

with Ω the angular rotation rate and ϕ_0 the initial rotation angle.

In particular, 3 classes have been provided; each comprises 280 realizations of rotating blade returns simulated using(6.11). Here, the parameters representing the simulated classes for a total of 840 observations are reported.

Class 1. Healthy operation

The wind turbine basic parameters are shown in Block[81]

Table 6.1 Wind Turbine Main Parameters

Wind wheel diameter (Commercial)	53m
Tower height	50m
Number of Blades	3
Rotation speed	0.4-1 π rad/s
Elevation angle	20-80°

The health wind turbine model is same as **Figure 5.12**, which parameter is shown in **Table 6.1**. Wind Turbine with $N_B = 3$ blades, L=26 m main blade length, angular rotating rate varies $\Omega = (0.2 - 0.5) \times 2\pi rad / s$, initial phase of the blades randomly choose within 2π, the elevation angle β between radar and blade rotation center varies from 20° to 80° and the height of blades rotation center is 50 meters.

Class 2. Operation with one blade vibration in x axis

The Vibration model is shown in **Figure 5.15**. Wind turbine parameters used as Class 1, set one blades vibrates along x axis with vibration amplitude 0.2 or 1 meters combined with vibration frequency of $1\times 2\pi$ or $2\times 2\pi$ rad/s (4 combination results).

Class 3. Operation with some parts of blades corrosion

The Corrosion model is shown in **Figure 5.18**. Wind turbine parameters used as Class 1, set part of three blades are corroded by changing the RCS of some specific pieces.

The other parameters, used to compute in the simulation data, are the range resolution $R_r = 1$ m, pulse repetition frequency $PRF = 2200$, signal duration $T =$ 2s,5s,10s, radar operative frequency $f_0 = 1.5GHz$, one end (root) of the blades $L_1 = 0.5$ m, other end (tip) of blade $L_2 = L_1 + L = 26.5$ m, blade width $W = 1$ m, rotor center location ($x = 0, y = 0, z = 0$), and radar location $x_r = 200, y_r = 0, z_r =$ variable.

Database description

The algorithm is applied to simulation L-band data, database consisting of different operation condition of wind turbine blades, with randomly initial phase angle of blades, the database are supposed to cover the full elevation angles, for analysis, the elevation angle has been divided into sub angles of 10°, 4 different rate of blades $\Omega = (0.2 - 0.5)\times 2\pi rad/s$ for each of the 7 angles (20° to 80°) are available. In **Table 6.1**, the concept of the database is shown. In this way, different elevation angles are taken to testing the database which gives the independent training and validation sets. Obtained the different values of the elevation angle β_E as follow:

$$\beta_E = 20^\circ + \varepsilon 10^\circ \tag{6.13}$$

with $\varepsilon = 0,...,6$

The number of observation for each class are 280, 1120, 1120 (Class1, Class2, Class3) respectively. The database for simulated data is composed of 280 realizations of the received signal for each class. The use of limit observation for training is practical realization. The training observation are selected randomly with same number to characterize the class. After the spectrogram is computed, additive zero-mean Gaussian noise has been added to it. Specifically, the spectrogram is calculated by a number of points for the discrete Fourier transform (DFT) N_{DFT}, a Hamming window of length M with 75% overlap. The performance is shown for varying the signal to noise (SNR) ratio (-5dB, 0dB, 5dB, 10dB, 15dB) and variable time (10s, 5s, 2s). In order to obtain a square representation of the spectrogram, N_{DFT} is given by

$$N_{DFT} = \left\lceil \frac{N - W_{overlap}}{W(1 - overlap\%)} \right\rceil \tag{6.14}$$

Where N is the number of points of signal. $\lceil \cdot \rceil$ represents the smaller integer greater than or equal to the argument, and the percentage overlap is in the interval [0,1].

Figure 6.4 shows an example of a spectrogram obtained for each class and with a signal to noise power ratio (SNR) of -5dB. As shown in **Figure 6.4**, the three classes show a different time-frequency spectrogram and CVD, representing a good test case for propose algorithm. In **Figure 6.5**, an example of spectrogram and CVD for each class is given with an SNR of 5dB.The proposed algorithm will give additional classification.

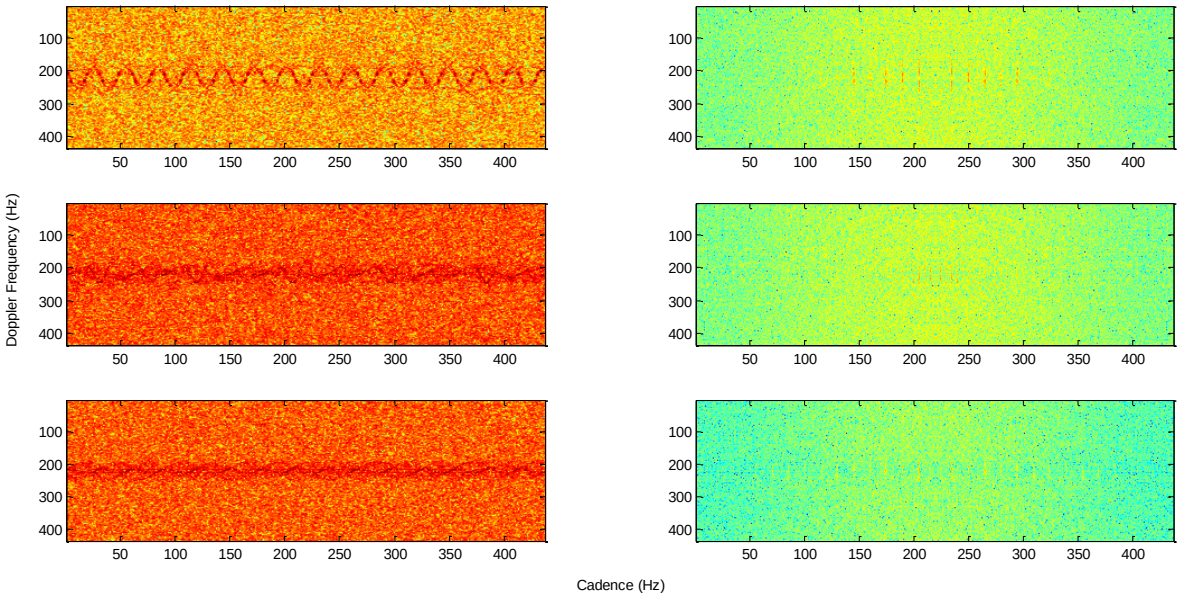

Figure 6.4 Example of spectrogram (with SNR=-5dB) for 3 classes of return from wind turbine rotation blades with 9th order moment. Figures on left refer to spectrogram of class1, class 2 and class 3, respectively. Figure on right refer to CVD of class1, class 2 and class 3.

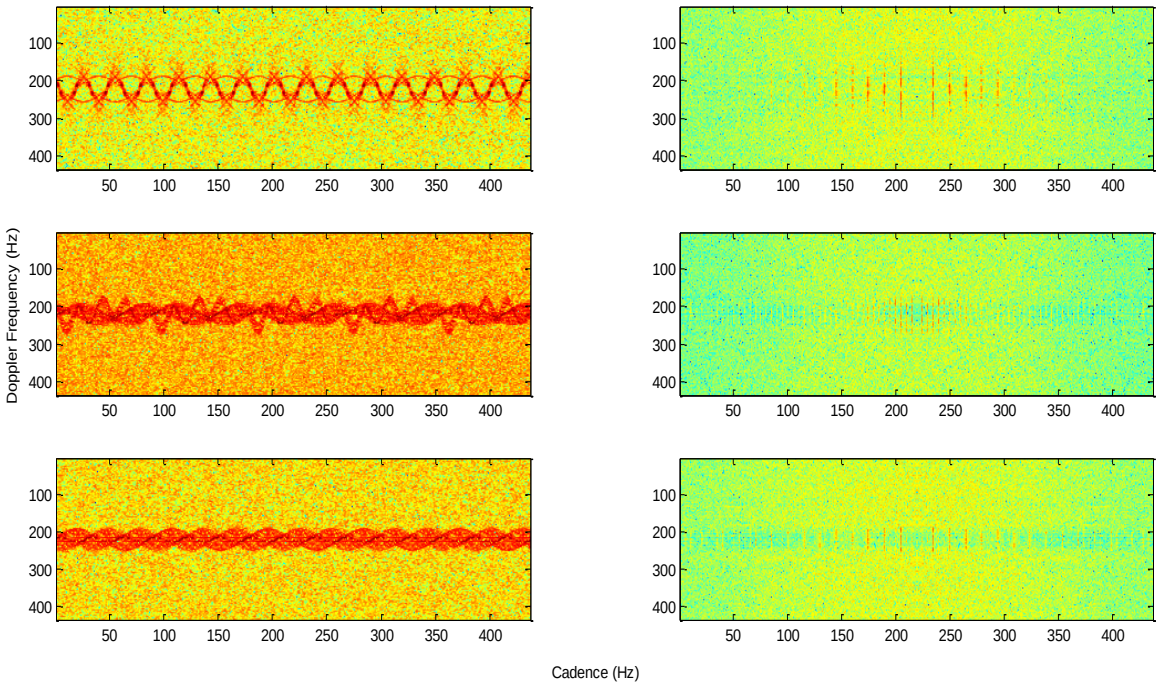

Figure 6.5 Example of spectrogram (with SNR=5dB) for 3 classes of return from wind turbine rotation blades with 9th order moment. Figures on left refer to spectrogram of class1, class 2 and class 3, respectively. Figure on right refer to CVD of class1, class 2 and class 3.

The analysis is conducted considering 70% of data for training and 30% for testing. All the available signal are divided randomly into training and testing sets. In order to statistically characterize the performance, A Monte Carlo approach is applied. 500 different experimental cases is performed, evaluating the average correct classification, in percentage, P_c (defined as the number of correctly classification over the total number of observation), P_r (defined as the number of correctly recognition over the total number of observation) and the Probability of Unknown P_U (defined as the number of unknown sub observation over the total number of observation) are used to figures of merit. The analysis is performed for different orders n of the Krawtchouk moment between 1 and 20. The range value of n is selected to consider that the sensitivity to

noise increase with n. The k value of kNN classifier is greater than 1 (considering the unknown class) and analyses different values.

6.2 Performance Analysis on the Simulation Data

In this section, the proposed classification algorithm is assessed in three cases.

6.2.1 Case 1. Classification between Healthy Operation (Class 1) and Unhealthy Operation which included One Blade Vibration (Class 2) and Operation with Some Parts of Blades Corrosion (Class 3)

In Case 1, the blades are divide into two classes which are Healthy condition (Class 1) and Unhealthy condition, and the Unhealthy class is divided into sub-classes, which are vibration condition (Class 2) and corrosion condition (Class 3). In this case, the meaning of classification is the ability to distinguish between Healthy class and Unhealthy class, while recognition means the capability to identify the Vibration class and Corrosion class. At last, unknown means the number of analyzed observations which the classifier does not make a decision over the total number of observation. The classification chart of Case 1 is shown in **Figure 6.6.**

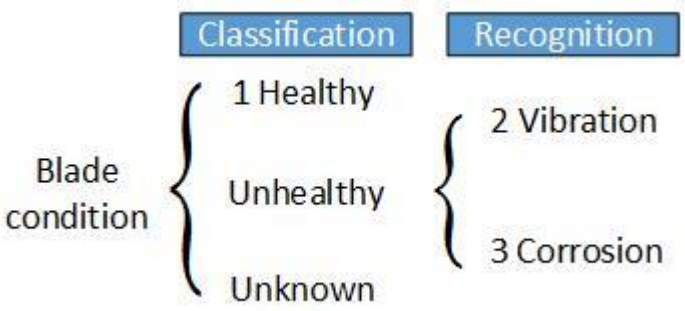

Figure 6.6 Classification chart of Case 1

Correct classification (%) versus moments order for simulated wind turbine blades data for different values of SNR.

Probability of Classification

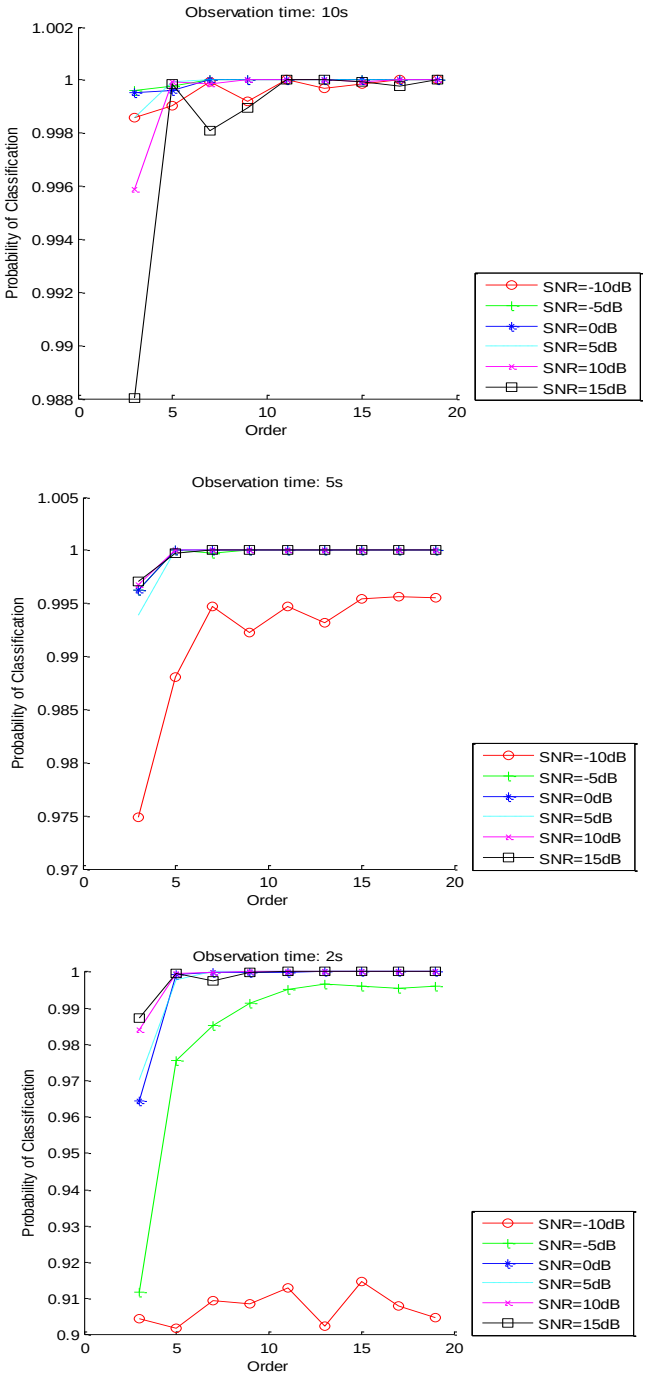

Figure 6.7 Correct classification versus moments order and duration time for simulated wind turbine blades data for different values of SNR

Table 6.2 Average Correct Classification (%) for Different Observation Time Windows and Krawtchouk Moment Orders

Observation Length [s]	Krawtchouk Moments Order(SNR=15)								
	3	5	7	9	11	13	15	17	19
10	0.98802	0.99984	0.9981	0.99897	1	1	0.99992	0.99976	1
5	0.99706	0.99976	1	1	1	1	1	1	1
2	0.98722	0.9996	0.99754	0.99976	1	1	1	1	1

Figure 6.7 shows the performance obtained by using the Krawtchouk moment based approach. In this case, the polynomial order determines the number of Krawtchouk moments and also the dimension of feature vector. From **Figure 6.7**, it is clear that the performance generally improved as the signal moment order and duration time increases. For the low SNR level, the noise effect is serious; for a signal duration of 2 seconds, the probability of classification increase quickly, becoming greater than 0.96 for SNR greater than -5dB. Moreover, for observation time of 10 and 5 seconds, SNR greater than 5dB, as the moments order increases, both of them achieve probabilities of about 0.998 for order greater than 10.

Probability of Unknown

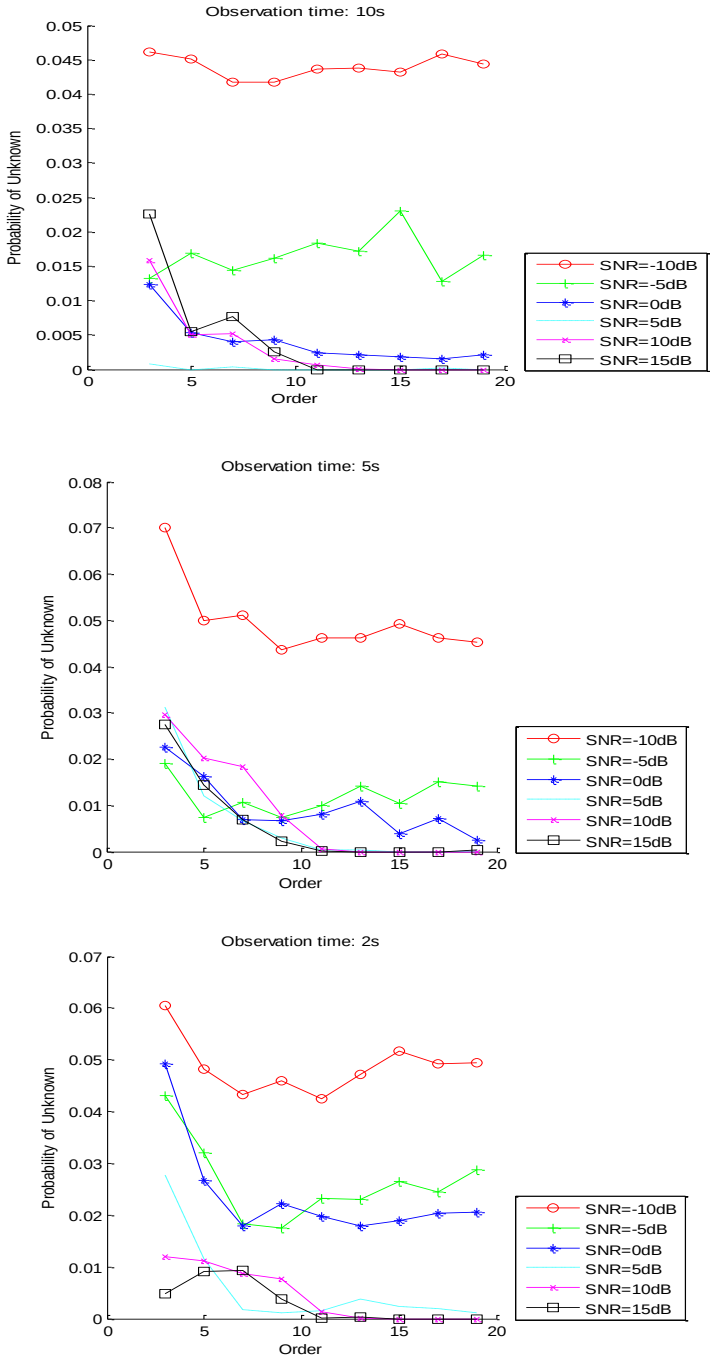

Figure 6.8 Probability of Unknown versus moments order and duration time for simulated wind turbine blades data for different values of SNR

Table 6.3 Confusion Matrix Averaged Showing The Percentage Of Correct Recognition Using Krawtchouk Moments, SNR -5dB, ORDER=9.

		Prediction Classification			
		Healthy	Vibration	Corrosion	Unknown
Real Classification	Healthy	100.0000	0	0	0
	Vibration	0	92.8810	2.2619	4.8571
	Corrosion	0	1.3810	98.6190	0

Figure 6.8 shows the performance in terms of P_U, the probability of unknowns reduces as the moment order increases. The performance generally improves as both signal duration and moments order increase. From order 3 to order 5, P_U decreases quickly, for order greater than 5, P_U is smaller than 0.01 for the SNR over than -5dB. In contrast, for duration equal to 10 seconds and for SNR of -10dB, P_U is about 0.045, while for lower noise levels P_U becomes smaller than 0.025 as the order increases.

6.2.2 Case 2 Classification between Healthy Operation (Class 1), Operation with One Blade Vibration (Class 2) and Operation with Some Parts of Blades Corrosion (Class 3)

In case 2, the performance is performed classifying (Class 1, Class 2 and Class 3), in which, we only consider the Probability of correct Classification (P_C) and Probability of Unknown (P_U). Specifically, the meaning of P_C is the ability of identify the blade working condition within the three classes, while P_U is computed the ratio of the number of the observations which the classifier does not make a decision and the total number of observations.

P_Classification

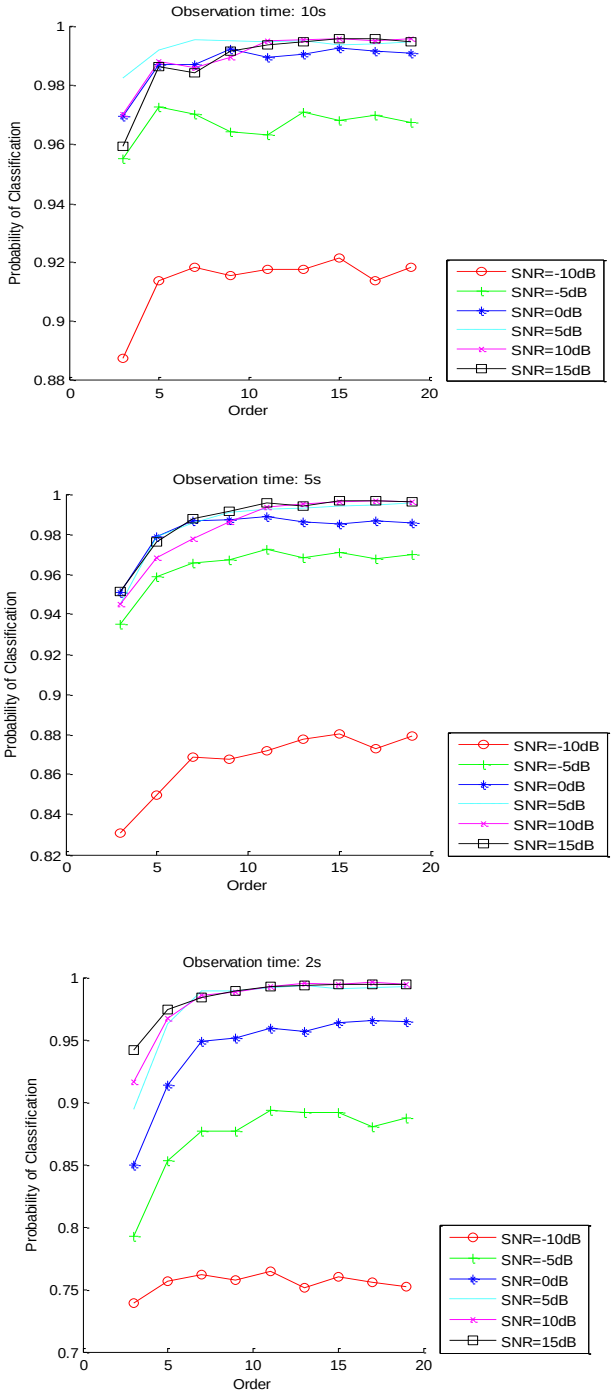

Figure 6.9 Correct classification versus moments order and duration time for simulated wind turbine blades data for different values of SNR

In **Figure 6.9**, A similar trend is found for the target recognition case with performance going from 88% to 99.8%. The high order of moments are increasingly influenced by the noise. It can be observed that decreasing the observation time cause the performance of the classifier to decrease because the reduced number of training observations.

P_C and P_R generally improves as the moments order and the SNR increase. However, they both decrease as the signal duration decrease.

P_Unknown

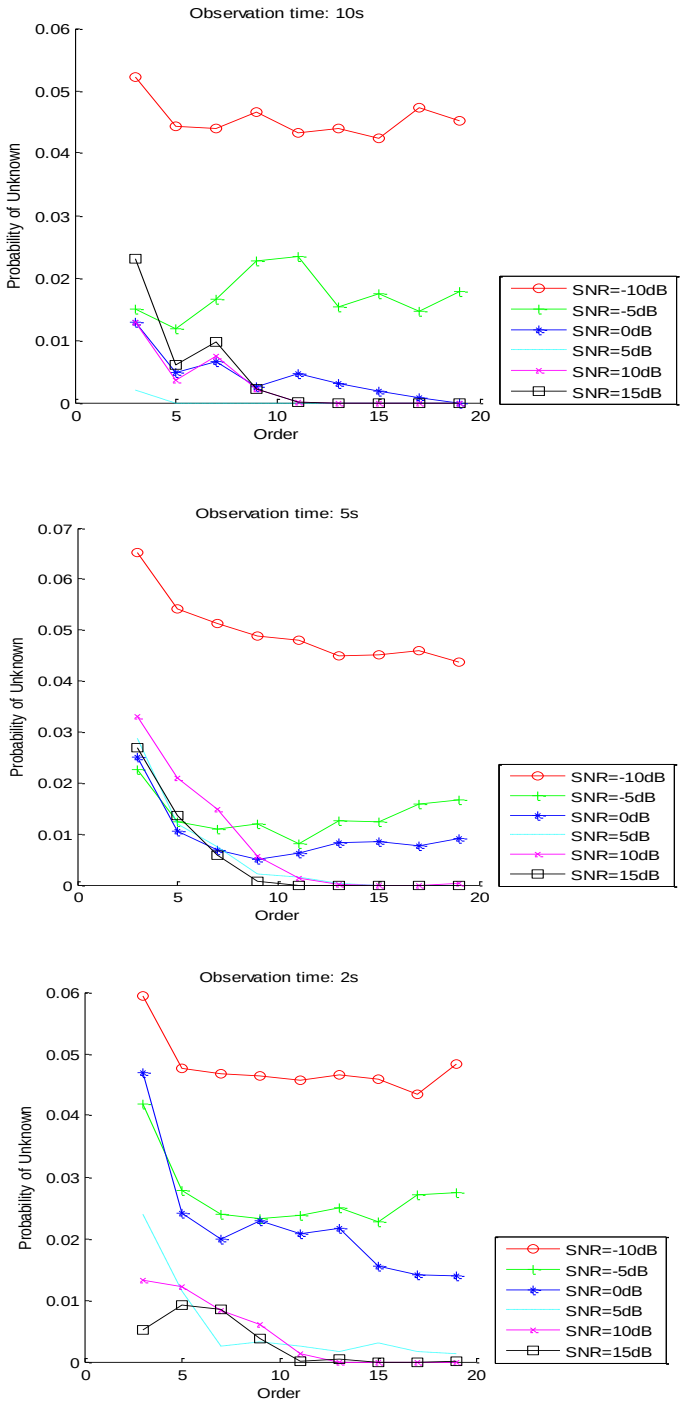

Figure 6.10 Probability of Unknown versus moments order and duration time for simulated wind turbine blades data for different values of SNR

Figure 6.10 represents the performance in terms of Pu. It is clear observe that, for SNR greater the -5dB, the performance generally increase as both the signal duration and moment order increase. For duration equal to 10 seconds and for SNR of -10dB, Pu is about 0.05, while for lower noise levels Pu becomes smaller than 0.01 as the order increase. For observation time of 5 and 2 seconds, Pu is smaller than 0.05, for order greater than 10 and for all noise level.

6.2.3 Case 3. Classification between Healthy Operation (Class 1) and Operation with One Blade Vibration (Class 2) And Classification between Healthy Operation (Class1) and Operation with Some Parts of Blades Corrosion (Class 3)

In case 3, the performance is performed classifying (Class 1, Class 2) and (Class 1, Class 3), because wind power companies need to identify different types of blade working condition, this classification method is practical. We can derive the Probability of correct Recognition (P_R) which means the number of correct recognition of the observations Class 1 and Class 2 or Class 1 and Class 3 over the total number of observations. And P_U is computed the ratio of the number of the observations which the classifier does not make a decision and the total number of observations.

Performance of recognition between class 1 and class 2

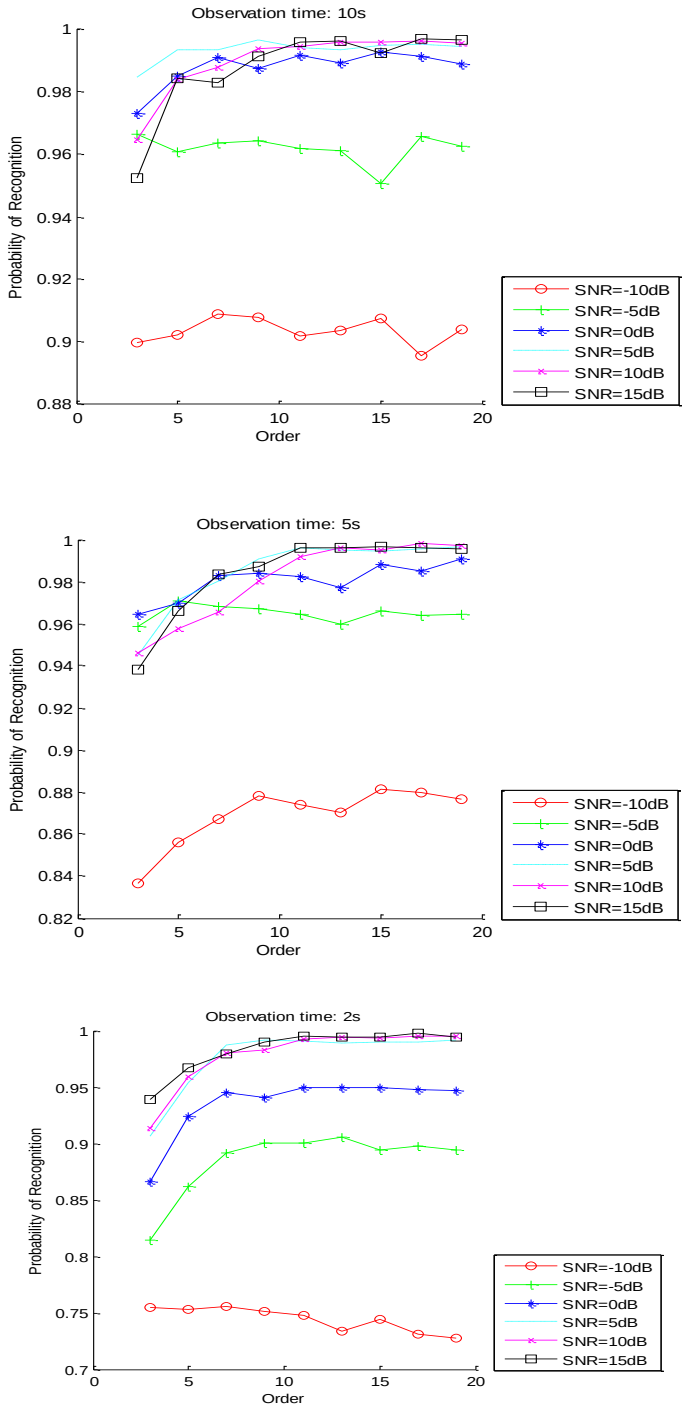

Figure 6.11 Correct classification versus moments order and duration time for simulated wind turbine blades data for different values of SNR

Figure 6.11 shows the Probability of correct Recognition (P_R) between Class 1 and Class 2, for signal duration of 2 seconds, they increase quickly, becoming greater than 0.92 for SNR greater than -5dB. For signal duration of 5 and 10 seconds, P_R are greater than 0.83 for all the considered value of SNR and Order.

Performance of recognition between class 1 and class 3

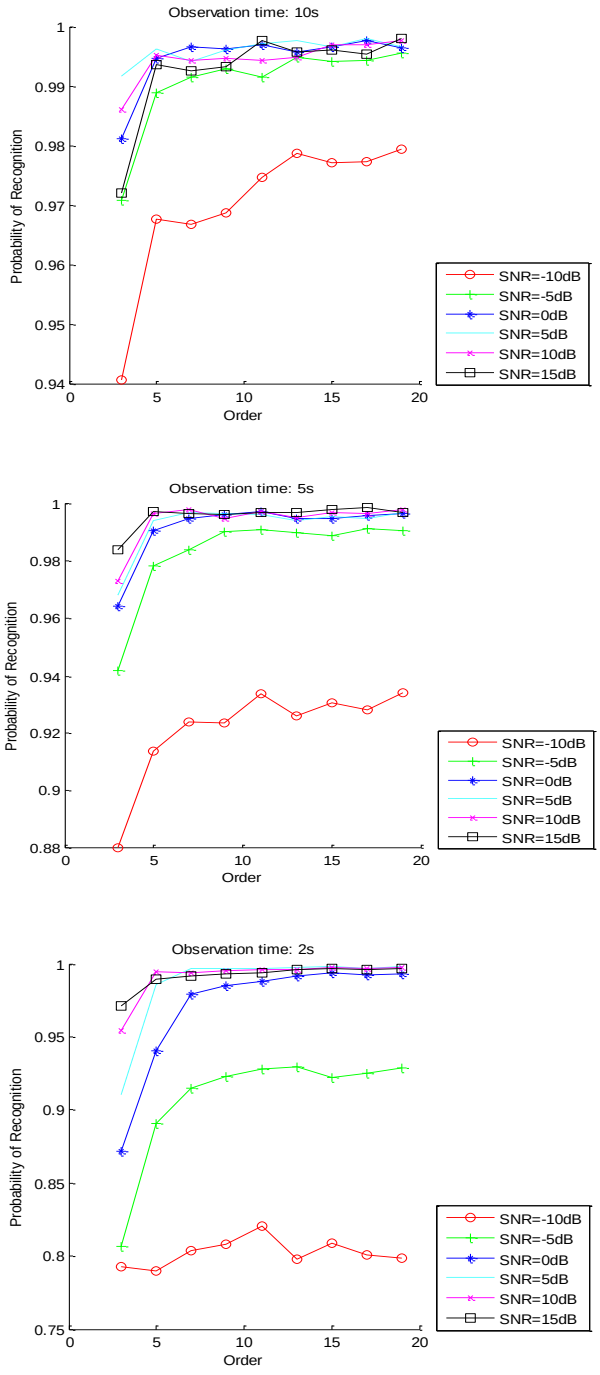

Figure 6.12 Correct classification versus moments order and duration time for simulated wind turbine blades data for different values of SNR

Observing **Figure 6.12**, it is clear that P_R increasing as the SNR and observation time increasing. In particular, for signal duration of 10 seconds, P_R is greater than 0.98 for SNR greater than -10dB; for duration equal to 5 seconds, instead, P_R is greater than 0.99 for SNR greater than-10dB and order greater than 10. From the results it is clear that higher is the SNR, then higher is the performance.

In this section, a novel algorithm for wind turbine working condition with the capability of target identification between health and unhealthy wind turbine blades has been presented. This signal model has been used to simulate the received signal from the wind turbine blades on different elevation angle. After that, Krawtchouk moment of radar micro-Doppler based on the CVD has been test by kNN classifier. The results has shown that, for the three cases, the algorithm results get a sufficient degree of correct classification, and also, an unknown class involved in the test, in which, the feature vector under test does not belong to one of the classes. The algorithm also can recognize the unknown class.

Chapter 7 Conclusion

7.1 Conclusion

In this research, we focus on the micro Doppler effect on wind turbine blades, the capability of micro Doppler based recognition of wind turbine blade condition monitor between healthy condition and unhealthy condition has been evaluated, which is an efficient, accurate and practical approach. In Chapter 1, we introduce some typical situations of blade failure models and the status of monitoring blades. Select some failure models adapted to radar detection as the study content. In Chapter 2, we introduce the principle of radar working and radar echo analysis. We also introduce the methods of Radar Cross Section prediction. In Chapter 3, we introduce the basic theory of wind turbine and analyze the stress of blades to understand the blade vibration information. In Chapter 4, we introduce the micro Motion and derive the micro Doppler from the rotation wind turbine blade. Establish mathematical space model of radar and wind turbine blades, analyzing the wind turbine blades Doppler effect and analyzing the data of wind turbine blade backscatter signal. In Chapter 5, we use radar technology to analyze three typical wind turbine blade models. Since the large amount of information simulation data, in Chapter 6, we use Krawtchouk moment to extract data feature, in the meantime, the blade model is repeatedly amended and finally give the ideal result of fault recognition. Experimental results show that this method can effectively identify wind turbine blade vibration and corrosion.

7.2 Future Work

This thesis mainly based on simulation data testing, in the next step, we prepare to use the real data to verify the actual radar echo, for practical problems, we can detect from one wind turbine to several wind turbine running. Try to use bistatic radar to analyze the health of each blade providing more convenient and reliable protection for the safe operation of the wind power. Try to

use another Joint time and frequency analysis tool in order to adapt analysis frequency characteristics of the non-stationary signals, we need analysis tool with multi-resolution analysis. We can also improve the design in the aspect of computing speed, expanding the existing failure modes to another failure mode. We can also use other algorithms to extract data features, such as neural networks.

Limitations of STFT: STFT attempt to take into account the time and frequency resolution by a window function, but the window function keep constant throughout the conversion process and it is essentially a single analytical method and fixed resolution. In order to adapt analysis frequency characteristics of the non-stationary signals, we need analysis tool with multi-resolution analysis.

RCS computing: This thesis assumes that the blade is uniform metal scattering body, in fact, the modern wind turbine in order to avoid interference with civil, military radar, often made some design reduced RCS, the RCS model in this thesis may have different with real one. For the real one, adjust the radars gain, power, or close to the target can solve these problems. Actually, the model is a test model, It is important to make the algorithm valid. Model classification: This thesis only discusses three typical fault modes, in practical applications, there may be several faults occur simultaneously, so it is not a simple pattern classification. There may also be other types of failure adapted to radar, which requires further study and summarize. During training, this thesis does not consider the distinction between the modes, and no consider of recognize performance not within trained samples set, which should be strengthened in the follow-up work.

Classification algorithm: we use the Krawtchouk Moment to do the feature extraction, comprising a plurality of step, including spectrogram, cvd, and classification. This process is involved with many manual interventions. Now mainstream methods is based on deep learning neural network algorithm to take advantage of machine self-learning which is a simple process. It achieves a breakthrough in many areas, if it is used in this study; it is also possible to obtain better classification and recognition performance.

In the specific implementation of the algorithm, the algorithm takes long time to run, and many operations are repeated, if based GPU acceleration algorithms, it can be greatly improved processing speed.

In the aspect of radar: the current radar echo acquisition mode only considers the case of one wind turbine, in real application, a plurality of wind turbines echo may also appear in the radar echo. For this, the radar needs the ability of range resolution, we need a system of pulse radar, in the reflected signal, search the distance unit of wind turbines, then do the above analysis.

In the aspect of extraction of parameters: wind turbine reflected signal is a typical multi-component signal, which spectral is overlapped, due to the rotation of the blades, the frequency has higher order and linear change, which requires time-frequency analysis algorithm has good clarity, and adapt to changes in spectral lines. STFT used in this thesis adapts stable characteristic of the signal time and frequency. For multi-component signal, STFT spectrogram does not have cross-terms, but the time and frequency concentration is poor. The time and frequency of Wigner-Ville distribution (WVD) is energy concentrated but it presences cross-term. By improving WVD, can effectively suppress WVD cross - terms interference, while maintaining a high time-frequency concentrated. With this algorithm it can get a clearer time-frequency diagram. Therefore, in the future we can consider WVD and another various improved algorithms to calculate the time-frequency figures.

In the aspect of pattern recognition algorithms: in this algorithm of training process, there is no consideration of the distinction between the various modes, if added Discriminative Training in the training process, such as using the Minimum Classification Error(MCE), theoretically, it can improve the recognition rate of mode. In addition, for the problem of sample rejection other than the three types of fault, this thesis does not discuss.

Using radar technology to test wind turbine blades of wind power detection and diagnosis has broad prospects. In this thesis, through micro Doppler information analysis can constantly monitor

wind turbine blade condition, also have promotion and application value, will greatly reduce the risk of unsafe of wind turbine blades.

Reference

1. Li D., Y.Z., Bao N., et al. , Vibration modal analysis of the rotating rotor of horizontal axis wind trbine. Acta Energiae Solaris Sinica, 2004(1): p. 72-77.
2. Richard Smith, Anatomy of a Horizontal-Axis Wind Turbine, May 30, 2007. http://www.symscape.com/blog/anatomy_horizontal_wind_turbine.
3. Chengdu Good Good International Trading Co., Ltd, Vertical Axis Wind Turbine Generator, January, 2006. http://www.cccme.org.cn/products/detail-3059268.aspx.4. Time and Date AS 1995–2017, World Temperatures — Weather Around The World, 2016, https://www.timeanddate.com/weather/?sort=0.
5. Kim Cambron, Blade breaks on wind turbine near Armstrong, 29.11.2012. http://www.rantoulpress.com/news/other/2012-11-29/blade-breaks-wind-turbine-near-armstrong.html.
6. Yang B., S.D.T., inspecting and monitoring technologies for wind turbine blades: A survey. Renewable and Sustainable Energy Reviews, 2013. 22: p. 515-526.
7. S., Y., Lightning protection of wind turbine blades. Electric Power Systems Research, 2013. 94: p. 3-9.
8. Miller R.H., Dugundji J., Chapral., et al. Dynamics of horizontal axis wind turbines[J]. Wind Energy Conversion, 1978, Vol.III, MITASAL TR-184-9.
9. GLOBAL WIND ENERGY COUNCIL, GLOBAL WIND STATISTICS 2014, 10.2.2015. http://www.gwec.net/wp-content/uploads/2015/02/GWEC_GlobalWindStats2014_FINAL_10.2.2015.pdf

10. Castelli M.R., M.A.D., Quaresimin M., et al., Numerical evaluation of aerodynamic and inertial contributions to Darrieus wind turbine blade deformation. Renewable Energy, 2013. 51: p. 101-112.

11. Homola M.C., V.M.S., Wallenius T., et al, Effect of atmospheric temperature and droplet size variation on ice accretion of wind turbine blades. Journal of Wind Engineering and Industrial Aerodynamics, 2010. 98(12): p. 724-729.

12. Lee J.W., L.J.S., Han J.H., et al, Aeroelastic analysis of wind turbine blades based on modified strip theory. Journal of Wind Engineering and Industrial Aerodynamics, 2012. 110: p. 62-69.

13. Maheri A., N.S., Vinney J., Decoupled aerodynamic and structural design of wind turbine adaptive blades. Renewable Energy, 2007. 32(10): p. 1753-1767.

14. Sloth C., E.T., Stoustrup J., Robust and fault-tolerant linear parameter-varying control of wind turbines, Mechatronics. 2011. 21(4): p. 645-659.

15. Schlechtingen M., S.I.F., Achiche S., Wind turbine condition monitoring based on SCADA data using normal behavior models. . Part 1: System description, Applied Soft Computing, 2013. 13(1): p. 259-270.

16. Aguglia D., V.P., Wamkeue R., et al, Determination of fault operation dynamical constraints for the design of wind turbine DFIG drives. Mathematics and Computers in Simulation, 2010. 81(2): p. 252-262.

17. Márquez F.P.G., T.A.M., Pérez J.M.P., et al, Condition monitoring of wind turbines: Techniques and methods. Renewable Energy, 2012. 46: p. 169-178.

18. Hameed Z., H.Y.S., Cho Y.M., et al, Condition monitoring and fault detection of wind turbines and related algorithms. A review, Renewable and Sustainable Energy Reviews, 2009. 13(1): p. 1-39.

19. Kraj A.G., B.E.L., Phases of icing on wind turbine blades characterized by ice accumulation. Renewable Energy, 2010. 35(5): p. 966-972.

20. Kraj A.G., B.E.L., Measurement method and results of ice adhesion force on the curved surface of a wind turbine blade. Renewable Energy, 2010. 35(4): p. 741-746.

21. QuGe, Chen., ZhaoXinGuang, ZhouBo, Wavelet scale spectrum identification of crack characteristics of wind turbine blades. Journey of Shenyang industry university. 2012. 34(1): p. 22-25.

22. ZhouBo, Chen., ZhaoXinGuang, GuQuan, Extract blind signal of crack wind turbine blade. Chinese Journal of Scientific Instrument, 2012. 33(7): p. 1483-1489.

23. QuGe, Chen., ZhouHao, ZhouBo, Crack identification of wind turbine blades based on emmison and neutral network. Machinery Design and Manufacture, 2012(3): p. 152-154.

24. C.K., L., Corrosion and wear-corrosion resistance properties of electroless Ni–P coatings on GFRP composite in wind turbine blades. Surface and Coatings Technology, 2008. 202(19): p. 4868-4874.

25. Ciang C.C., L.J.R., Bang H.J., Structural health monitoring for a wind turbine system: a review of damage detection methods. Measurement Science and Technology, 2008. 19(12): 122001.

26. Dalili N., E.A., Carriveau R., A review of surface engineering issues critical to wind turbine performance. Renewable and Sustainable Energy Reviews, 2009. 13(2): 428-438.

27. Knut O.R., J.W.H., Carl J.C., Reliability-based fatigue design of wind-turbine rotor blades, Engineering Structures. 1999. 21(12): 1101-1114.

28. Marín J.C., B.A., París F., et al, Study of fatigue damage in wind turbine blades. Engineering Failure Analysis, 2009. 16(2): 656-668.

29. Marín J.C., B.A., París F., et al, Study of damage and repair of blades of a 300kW wind turbine. Energy, 2008. 33(7): 1068-1083.

30. Shokrieh M.M., R.R., Simulation of fatigue failure in a full composite wind turbine blade. Composite Structures, 2006. 74(3): 332-342.

31. Chou J.S., C.C.K., Huang I.K., et al, Failure analysis of wind turbine blade under critical wind loads. Engineering Failure Analysis, 2013. 27: 99-118.

32. Wang F.L., M.C.K., Adaptive modelling of transient vibration signals. Mechanical Systems and Signal Processing 2006. 20(4): 825-842.

33. Wu J.D., H.C.C., Fault gear identification using vibration signal with discrete wavelet transform technique and fuzzy–logic. Expert Systems with Applications, 2009. 36(2): 3785-3794.

34. Xun J., Y.S.Z., A revised Hilbert–Huang transformation based on the neural networks and its application in vibration signal analysis of a deployable structure. Mechanical Systems and Signal Processing, 2008. 22(7): 1705-1723.

35. Zhao M.S., Z.J.H., Yi C.P., Time–frequency characteristics of blasting vibration signals measured in milliseconds. Mining Science and Technology (China), 2011. 21(3): 349-352.

36. Liu X.H., R.R.B., Blind source separation of internal combustion engine piston slap from other measured vibration signals. Mechanical Systems and Signal Processing, 2005. 19(6): 1196-1208.

37. Kyle Sherer, Climbing robot inspects wind turbines for damage, January 30th, 2009. http://newatlas.com/riwea-robot-inspects-wind-turbines-for-damage/10844/

38. K.Thomsen, P.S., Fatigue loads for wind turbines operating in wakes[J]. Journal of wind engineering and industrial aerodynamics, 1999. (80): 121-136.

39. BaoKai, Wang., WuDongLiu, New nondestructive testing techniques-- Infrared thermal wave imaging detection[J](Chinese), 2006. 8(28): 393-408.

40. Changduk Kong, T.K., Dongju Han, et al, Investigation of fatigue life for a medium scale composite wind turbine blade[J]. International Journal of Fatigue, 2006. (28): 1382–1388.

41. ShenXiaoHong, YangFeng, JingJing. The study of digital ultrasonic flaw detector based on PC/104[J](Chinese). 2006(5):46-51.

42. GanChuanFu, Zhang., ZhangBing, Introduction to microwave exploration[J]. nondestructive testing(Chinese), 2001.6.251-253.

43. E.A.Bossanyi, GH Bladed theory manual. Garrad Hassan and Partners Limited, April, 2005.

44. ChenBoXiao, ZhuWei, SunGuangCai, YangLin. Modern Radar System Analysis and Design. Sep, 2012. P89-90.

45. Knott, E.F., J.F.Schaffer, and M. T. Tuley, Radar Cross Section,. 2nd.,Norwood, MA: Artech House, 1993.

46. Ruck, G.T., et al., Radar Cross Section Handbook. New York: Plenum Press, 1970.

47. Jenn, D., "Radar Cross-Section," in Encyclopedia of RF and Microwave Engineering, K.Change, (ed.). New York: John Wiley & Sons

48. Ting, X., Moment-based method for image analysis. Southeast University, 2006.

49. K, H.M., "Visual pattern recognition by moment invariants". IRE Transaction on Information Theory, 1962. 8(1): p. 179-187.

50. R, T.M., "Image analysis via the general theory of moment". Journal of the Optical Society of America, 1980. 70(8): p. 920-930.

51. H, Y.P.T.a.R.P.a.O.S., "Image analysis by Krawtchouk moments". IEEE Transactions on Image Processing, 2003(12(11)): p. 1367-1377.

52. Bhatia A B and Wolf E, " On the circular polynomials of Zernike and related orthogonal sets", Proceedings of Camb Phil Soc, 1954, 50: 40-48.

53. Ping Z L, Wu R G and Sheng Y L, "Image description with Chebychev-Fourier moments", Journal of Optical Society of America A, 2002, 19(9): 1748-1754.

54. Marcelo Gustavo Molina and Juan Gimenez Alvarez, Technical and Regulatory Exigencies for Grid Connection of Wind Generation. 14 June, 2011. https://www.intechopen.com/books/wind-farm-technical-regulations-potential-estimation-and-siting-assessment/technical-and-regulatory-exigencies-for-grid-connection-of-wind-generation

55. ZhuCunXu, Research on Detection Device of Wind Turbine Blades. North China Electric Power University, 2012.

56. ZhangYuLiang, ChengZhaoXue, YangCongXin. Wind turbine design for wind speed processing[J]. Shenyang University of Technology. 2006, 28(6): 687-689.

57. SCOTT J GRUNEWALD, NEW 3D PRINTING MATERIAL MIMICS LIGHT WEIGHT BALSA WOOD FOR USE IN WIND TURBINE CONSTRUCTION. JULY 04TH 2014. https://www.google.com.hk/search?safe=strict&biw=1916&bih=886&tbm=isch&sa=1&q=wind+turbine+blade+structure&oq=wind+turbine+blade+structure&gs_l=psy-ab.3..0i19k1.32870.36068.0.36294.11.10.1.0.0.0.354.913.4j2j0j1.7.0....0...1.1.64.psy-ab..3.8.913.3mcMdbzTOLM#imgrc=BiLpTqEiK0tkBM:

58. helicopter aerodynamics. Dec. 12. 2010. http://www.tech-domain.com/thread-29388-1-1.html

59. Tony Burton, David Sharpe, Nick Jenkins, Ervin Bossanyi. Wind Energy Handbook,2001.p60-63. John Wiley & Sons, Ltd.

60. Fraunhofer Institute, Wind Power: Smart anti-icing system for rotor blades, December 5, 2014.http://www.pennenergy.com/articles/pennenergy/2014/12/wind-power-smart-anti-icing-system-for-rotor-blades.html

61. Joseph Bebon, GE Investigates Two More Turbine Blade Breaks, May 13, 2014. http://nawindpower.com/ge-investigates-two-more-turbine-blade-breaks

62. Chen, V.C., et al.,"Micro-Doppler Effect in Radar: Phenomenon, Model, and Simulation Study," IEEE Transactions on Aerospace and Electornics Systems, 2006. Vol. 42, No.1: p. 2-21.

63. Goldstein, H., Classical Mechanics, 2nd ed. Reading, MA: Addison-Wesley, 1980.

64. Murray, R.M., Z.Li and S.S.Sastry, A Mathematical Introduction to Robotic Manipulation. Boca Raton, FL:CRC Press, 1994.

65. Wittenburg, J., Dynamics of Systems of Rigid Bodies. Stuttgart: Teubner, 1977.

66. Kuipers, J.B., Quaternions and Rotation Sequences. Princeton,NJ: Princeton University Press, 1999.

67. Klumpp, A.R., "Singularity-Free Extraction of a Quaternion from a Direction-Cosine Matrix". Journal of Spacecraft and Rockets, 1976. Vol. 13: p. 754-755.

68. Cooper, J., "Scattering by Moving Bodies: The Quasi-Stationary Approximation". Mathematics Methods in the Applied Sciences, 1980. Vol.2 No.2: p. 131-148.

69. Kleinman, R.E., and R. B. Mack, "Scattering by Linearly Vibration Objects,". IEEE Transactions on Antennas and Propagation, 1979. Vol.27, No.3: p. 344-352.

70. Van Bladel, J., "Electromagnatic Fields in the Presence of Rotating Bodies,". Proc. of the IEEE, 1976. Vol.64, No.3: p. 301-318.

71. Martin, J., and B. Mulgrew, "Analysis of the Theoretical Radar Return Signal from Aircraft Propeller Blades,". IEEE 1990 International Radar Conference, 1990: p. 569-572.

72. Misiurewicz, J., K.Kulpa, and Z.Czekala, "Analysis of Recorded Helicopter Echo,". IEE Radar 97, Proceedings, 1997: p. 449-453.

73. Mahafza, B., Radar Systems Analysis and Design Using Matlab London, U.K.: Chapman & Hall/CRC, 2000.

74. Anderson, W.C., The Radar Cross Section of Perfectly Conducting Rectangular Flat Plates and Rectangular Cyliners: A Comparison of Physical Optics, GTD and UTD Solution. Technical Report ERL-0344-TR DSTO, Australia, 1985.

75. ZhuNa, ZhangHui, ShuHuaZhong, Medical image retrival based on radial Krawtchouk moment. biomedical engineering research. 2008. 27（1）: p. 40-44.

76. C. Clemente, L.P., A. D. Maio, J. J. Soraghan and A. Farina, "A novel algorithm for radar classification based on doppler characteristics exploiting orthogonal Pseudo-Zernike polynomials,". in IEEE Transactions on Aerospace and Electronic Systems, January 2015. vol. 51, no. 1: p. 417-430.

77. Molchanov, P., Astola,J.Egiazarian,K.,and Totsky,K, Classification of ground moving radar targets by using joint time-frequency analysis. IEEE Radar Conference, Atlanta, GA, May 2012.

78. C. Clemente, L.P., I. Proudler, A. De Maio, J. J. Soraghan and A. Farina, "Pseudo-Zernike-based multi-pass automatic target recognition from multi-channel synthetic aperture radar,". in IET Radar, Sonar & Navigation, 4 2015. vol. 9, no. 4: p. 457-466.

79. Fukunaga, K., Introduction to Statistical Pattern Recognition Computer Science and Scientific Computing. Elsevier Science, 1990.

80. https://en.wikipedia.org/wiki/K-nearest_neighbors_algorithm#cite_note-3

81. Zachary Shahan, History of Wind Turbines, November 21, 2014. www.renewableenergyworld.com/ugc/articles/2014/11/history-of-wind-turbines.html